THE UNIVERSITY *of* EDINBURGH

Studies of the Structure of the T_z = -1 Nuclei ^{20}Na and ^{30}S for Explosive Astrophysics

Miss Jennifer Wallace

Doctor of Philosophy
The University of Edinburgh
March 2013

Abstract

In explosive astrophysical environments such as novae, X-ray bursters and supernovae, conditions of extreme temperature and density are achieved. Under such conditions, both the rate of energy release and path of nucleosynthesis are governed by reactions on unstable nuclei. In this light, direct reaction studies using radioactive ion beams play a vital role in determining nuclear reaction rates. However, in the vast majority of cases, direct measurements are not possible and as such, indirect measurements are equally important for the understanding of the main reaction processes driving astrophysical events.

In this thesis work, indirect studies of the astrophysically important ^{19}Ne$(p,\gamma)^{20}$Na and ^{29}P$(p,\gamma)^{30}$S reactions have been performed. For the first reaction, a β-delayed proton decay study of ^{20}Mg was performed to gain information about the spin-parity assignment of the first key resonance above the proton emission threshold in the compound nucleus ^{20}Na. This resonance is expected to dominate the ^{19}Ne$(p,\gamma)^{20}$Na reaction rate in explosive astrophysical environments and its identity has been under discussion for a long time, with $J^\pi = 1^+$ and 3^+ assignments suggested. In the present study an upper limit on the β-decay branch to this state of 0.02% with a confidence level of 90% is reported. This is significantly more stringent than previous studies and makes a 1^+ assignment highly unlikely, favouring instead a 3^+ assignment. A 3^+ assignment is predicted to have a significantly higher resonance strength and produce a proportionately higher ^{19}Ne$(p,\gamma)^{20}$Na reaction rate in X-ray burst conditions.

The second study performed was a detailed gamma-ray spectroscopy study of the nucleus ^{30}S. Excitation energies have been determined with improved precision over previous studies and the first, firm spin-parity assignments of key ^{29}P + p resonant states, expected to dominate the ^{29}P$(p,\gamma)^{30}$S reaction in stellar scenarios, have been made. An evaluation of the ^{29}P$(p,\gamma)^{30}$S reaction over the temperature range T = 0.06-2.5 GK shows that the 3^+ and 2^+ resonant states located at Er = 292.0(9) and 413.1(10) keV, respectively, dominate the

^{29}P$(p,\gamma)^{30}$S reaction rate in ONe novae, while the 413 keV resonance is expected to govern the rate in X-ray burster environments. These new, precise resonance energy measurements and firm spin-parity assignments have significantly reduced uncertainties in the ^{29}P$(p,\gamma)^{30}$S reaction in ONe novae and X-ray bursters. In particular, the reaction rate is now specified precisely enough for calculations of isotopic abundances in ONe novae ejecta.

Declaration

The two experiments that are described in this thesis were completed by myself, other members of the nuclear physics group at the University of Edinburgh and our collaborators at the Cyclotron Institute at Texas A&M University and Argonne National Laboratory. The data analysis and interpretation of results are my own work unless otherwise stated, and this work has not been submitted for any other degree or professional qualification except as specified.

Parts of this work have been published in Physical Review C and Physics Letters B.
Physics Letters B, J.P. Wallace *et al.*, 712(1):59 (*2012*).
Physical Review C, G. Lotay and J.P. Wallace *et al.*, 86(4):042801(R) (*2012*)
Physical Review C, J.P. Wallace and P.J. Woods, 86(6):068801 (*2012*) .

(*Miss Jennifer Wallace, March 2013*)

Acknowledgements

Firstly I would like to thank my first and second supervisors Prof. Phil Woods and Dr. Gavin Lotay. Their continued support and wisdom throughout the entirety of my PhD has been invaluable and I will be forever grateful to them.

Secondly I must thank my collaborators at Texas A&M University and Argonne National Lab. Without their expertise I would never have been able to complete the two experiments that have made up my thesis.

I must also thank all the students and staff in the nuclear group at The University of Edinburgh. Not only for their help throughout my PhD, but also for their friendship. In particular I must thank Helena David, Lea Reichhart, David Mountford and Daniel Doherty who's friendship I hope will last a lifetime.

I must also thank my family for their continued support through my PhD and my life. Without the support of my family I would never have got to where I am today. My family have supported every decision I have made throughout my life and I thank them wholeheartedly for their continued support.

Finally I must thank my wonderful future husband Jonathan Fryer. Without him standing by me throughout my PhD, patiently listening to me practice talks, picking me up when things went wrong and generally just putting up with me talking nuclear astrophysics to him I would never have completed this thesis.

Contents

List of Figures

List of Tables

Chapter 1

Nuclear Astrophysics Introduction

"It is important that we know where we come from, because if you do not know where you come from, then you don't know where you are, and if you don't know where you are, you don't know where you're going."

Terry Pratchett - I Shall Wear Midnight (2010)

The question of our origin has puzzled mankind through the ages, we look to the heavens in search of an answer, and amongst the stars we find one. Within the stellar environment the building blocks of the universe are created, seeding new stars and life itself. The nuclear reactions that allow stars to synthesise the elements that give rise to our existence are the very reactions that nuclear astrophysicists endeavour to understand.

Stars like our Sun are on the main sequence, burning hydrogen quiescently. The main two ways hydrogen burns in a main sequence star is either through the *pp* chains [1] or through the "cold" CNO cycles [2, 3], with the mass and chemical composition of the star dictating which burning process will dominate. When stellar environments become hotter and denser, the reactions change and it is possible for reactions to occur on heavier, more unstable nuclei. This is where processes such as the "hot" CNO cycles and the triple-α process start to take over the energy generation [4]. If the temperature and density of the environment is great enough it is possible to "break out" from these reactions, leading into the rp process, a series of rapid proton captures along the proton dripline [5].

The reactions involved in hot, dense stellar environments provide great experimental challenges when it comes to measuring them directly. This is due to the

exotic nature of the nuclei involved, with most reactions involving radioactive nuclei. As such radioactive beam facilities have been developed to study these reactions directly [6]. For most reactions the radioactive beam intensity required to measure the reaction directly has yet to be achieved at a high enough rate and therefore studying the direct reaction is not possible. However, it is often the case that reaction rates at astrophysical temperatures are dominated by a single resonance, and it is therefore possible to determine resonance parameters and reaction rates through indirect methods [7].
The reactions that will be discussed within this thesis play an important role within explosive binary systems, where temperatures and densities increase greatly. The next few sections will detail novae and X-ray bursters and the importance of the ^{19}Ne$(p,\gamma)^{20}$Na and ^{29}P$(p,\gamma)^{30}$S reactions within these explosive binary systems.

1.1 Novae

Novae are one of the most abundant explosive nuclear events in the galaxy, with 30$\pm$10 nova bursts every year [7]. The energy output of a nova outburst can reach $>10^4$ $L_\odot$, with between 10^{-5} and 10^{-4} $M_\odot$ ejected in each event [7]. The mean velocity of the material ejected is between $\sim 10^2$ - 10^3 km/s [7]. By analysing the abundance distribution in nova ejecta [9], and through the observations of γ-rays from β-unstable nuclides, a direct test of the predicted nucleosynthesis and nova model is possible [10].
A nova outburst occurs due to the accretion of hydrogen-rich material onto a white dwarf in a close binary system. An artists impression of the binary star system RS Ophiuchi is shown in Fig. 1.1. The binary star system is normally made up of a late main-sequence or red giant star with a more massive white dwarf. The white dwarf is typically composed of carbon-oxygen (CO) if the white dwarf is formed at the end of the helium burning stage, with a mass of $\sim$1 $M_\odot$, or oxygen-neon (ONe) if it comes from a more evolved progenitor and forms after the carbon burning stage, with a mass $\sim$1.2 - 1.4 $M_\odot$ [11, 12]. Material from the companion star that has filled its Roche lobe is accreted onto the white dwarf [14–16]. Fig. 1.2 shows a schematic diagram of a companion star filling it's Roche lobe. The infalling material carries angular momentum and builds up as an accretion disk on the white dwarf before falling onto the star.
The consequence of mass transfer depends on the composition of the mass

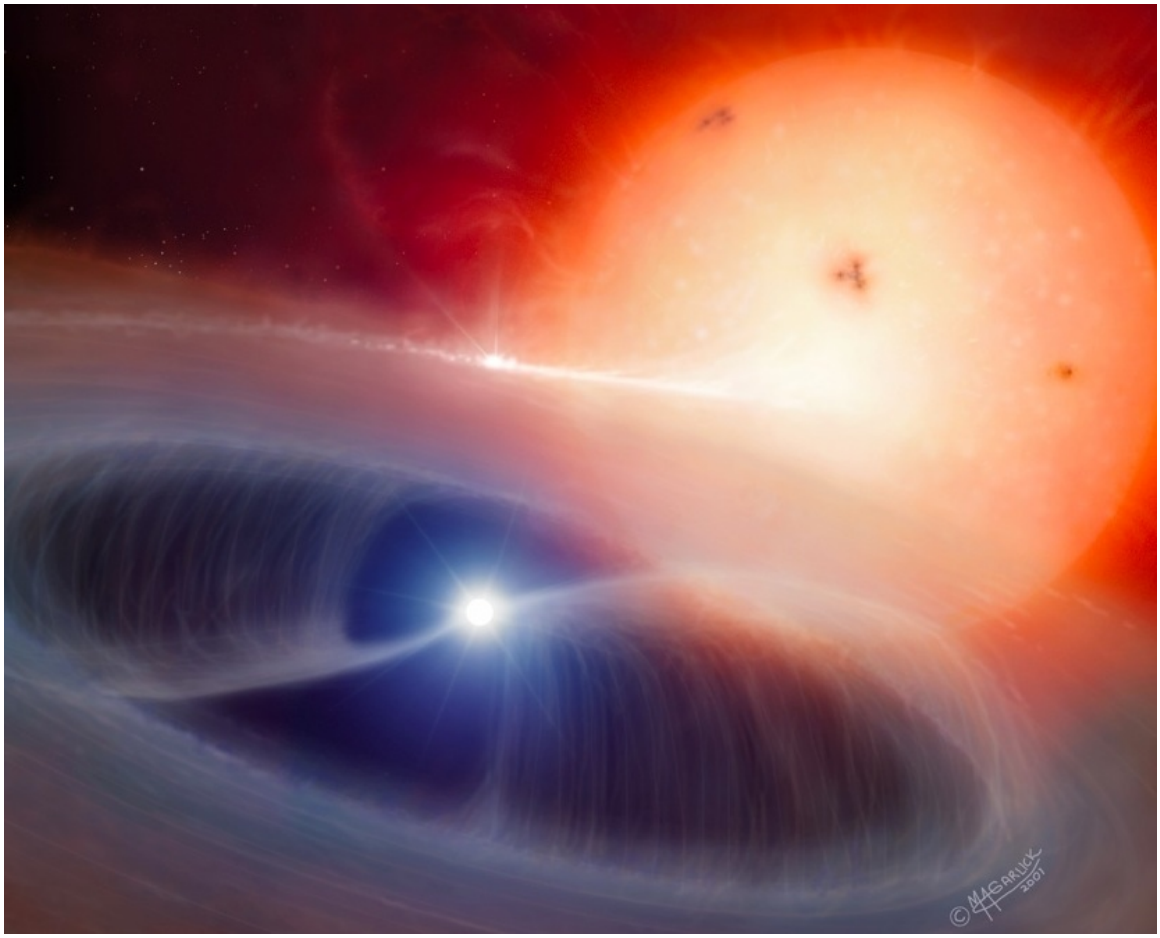

Figure 1.1 *An artists impression of the binary star system RS Ophiuchi [8].*

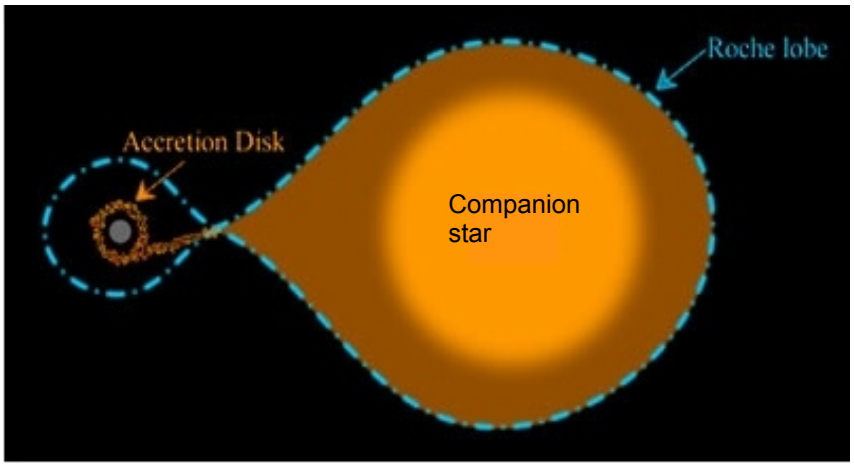

Figure 1.2 *Diagram representing a star in a binary system filling its Roche lobe. The Roche lobe is the region surrounding a star where orbiting material is gravitationally bound to the star [13].*

accreted, the temperature or degree of degeneracy and the rate of the mass transfer [17]. The rate of accretion is normally between $\sim 10^{-10}$-10^{-9} $M_{\odot}$/yr [7]. The matter that is accreted onto the white dwarf builds up as an envelope on the surface, gradually becoming more and more compressed and eventually degenerate. Due to the degenerate nature of the envelope it is not possible for the envelope to expand in order to cool and as such the temperature and density of the envelope continues to rise until thermonuclear runaway can ensue, leading to mass ejection. The dominant trigger reactions are the *pp* chains [15, 18, 19], with the hot CNO cycles taking over and providing the main source of energy for the thermonuclear runaway [20].

Within the CNO cycles there are two timescales, from the β-decay on ^{13}N, ^{14,15}O and ^{17}F, which are temperature and density independent in nova conditions, and from proton capture, dependent strongly upon the temperature [7]. Early within the runaway the CNO cycle is in equilibrium, with the timescale of the β-decay faster than the timescale of proton capture. However, when the temperature of the envelope reaches $\sim 10^8$ K the proton capture timescale decreases and is now faster than the β-decay timescale and the CNO cycle therefore becomes β-limited [4]. The energy produced is now too great to be transported by radiation and as such convection sets in [7]. The β-unstable nuclei are then transported to the cooler outer regions where they β-decay, initiating the nova outburst. The release of energy from the β-decays increases the temperature of the matter, allowing the degeneracy of the envelope to be lifted and as such expansion sets in, followed by the ejection of matter. Unburnt material is also brought into the burning shell by convection, effecting the nucleosynthesis [7].

If the gas is partially degenerate then the material will burn violently but no mass will be ejected [12]. For fully degenerate gas the pressure of the accretion disk is determined by the density of the gas rather than the temperature. The nuclear reactions that occur are unstable and although a lot of energy is released raising the temperature sharply, the gas does not cool due to little or no corresponding rise in outward pressure. For complete mass ejection the material needs to be degenerate enough such that the mass ejection is delayed whilst the thermonuclear runaway strengthens [12].

The light curve of a nova rises within a few days by a factor of 10^4 with a luminosity at its maximum of 10^{37} - 10^{38} ergs/s [7]. After the optimal maximum the emitted flux of a nova shifts to shorter wavelengths, with the flux in the ultraviolet increasing with decreasing flux in the optical. It is possible within some novae for the emission in the infrared to increase as the emission in the

ultraviolet decreases, believed to be due to dust grains, which form in the nova explosion, re-radiating the energy they have absorbed in the ultraviolet in the infrared [7].
For ONe white dwarfs it is possible for additional energy release to occur through the Ne-Na and Mg-Al cycles [21–23]. Peak temperatures range between 0.1 and 0.2 GK for CO white dwarfs and 0.4 and 0.5 GK for ONe white dwarfs [12]. The timescale for thermonuclear explosions range between 10^3 and 10^4 s [24]. During this time in order to conserve angular momentum the two stars spiral apart.
Directly after the thermonuclear explosion mass is transferred between the two stars at an accelerated rate due to radiation heating, causing the envelope of the companion star to expand [25]. After a while the binary system enters a period of low mass transfer until gravitational radiation and/or friction brings the two stars closer together and the cycle is repeated [12].

1.1.1 Novae and Pre-Solar Grains

The abundances of certain isotopes in novae ejecta can be different from those found in the solar system. These nucleosynthetic signatures provide a benchmark for nova models, although these models have yet to completely explain observations [16]. A method to obtain precise nova elemental abundances is through the study of pre-solar grains in a laboratory [26]. Pre-solar grains from nova origin are characterised by a series of ratios of different isotopes, namely low $^{12}C/^{13}C$, $^{14}N/^{15}N$ and $^{20}Ne/^{22}Ne$ ratios, high $^{26}Al/^{27}Al$ ratio and excesses of ^{30}Si [27]. Fig. 1.3 is taken from Ref. [22] and shows the different types of pre-solar grains, which are expected to form in the ejecta of three nova outbursts, where the mass and composition of the white dwarf differs. The silicon abundances are one of the most important markers as they are good indicators of the peak temperatures achieved in novae and they hint to the dominant nuclear pathways followed by thermonuclear runaway, giving a clear imprint on the overall composition of ejecta [22].
In order to interpret silicon isotopic abundances the rate of thermonuclear reactions that affect the production of silicon in novae need to be understood. One such reaction that affects the production of silicon in novae is the $^{29}P(p,\gamma)^{30}S$ reaction. Depending on the rate of the $^{29}P(p,\gamma)^{30}S$ reaction compared to the competing ^{29}P β^+-decay, the reaction flow can be directed towards ^{30}Si through the reaction sequence $^{29}P(p,\gamma)^{30}S(\beta^+\nu)^{30}P(\beta^+\nu)^{30}Si$ and away from ^{29}Si, the

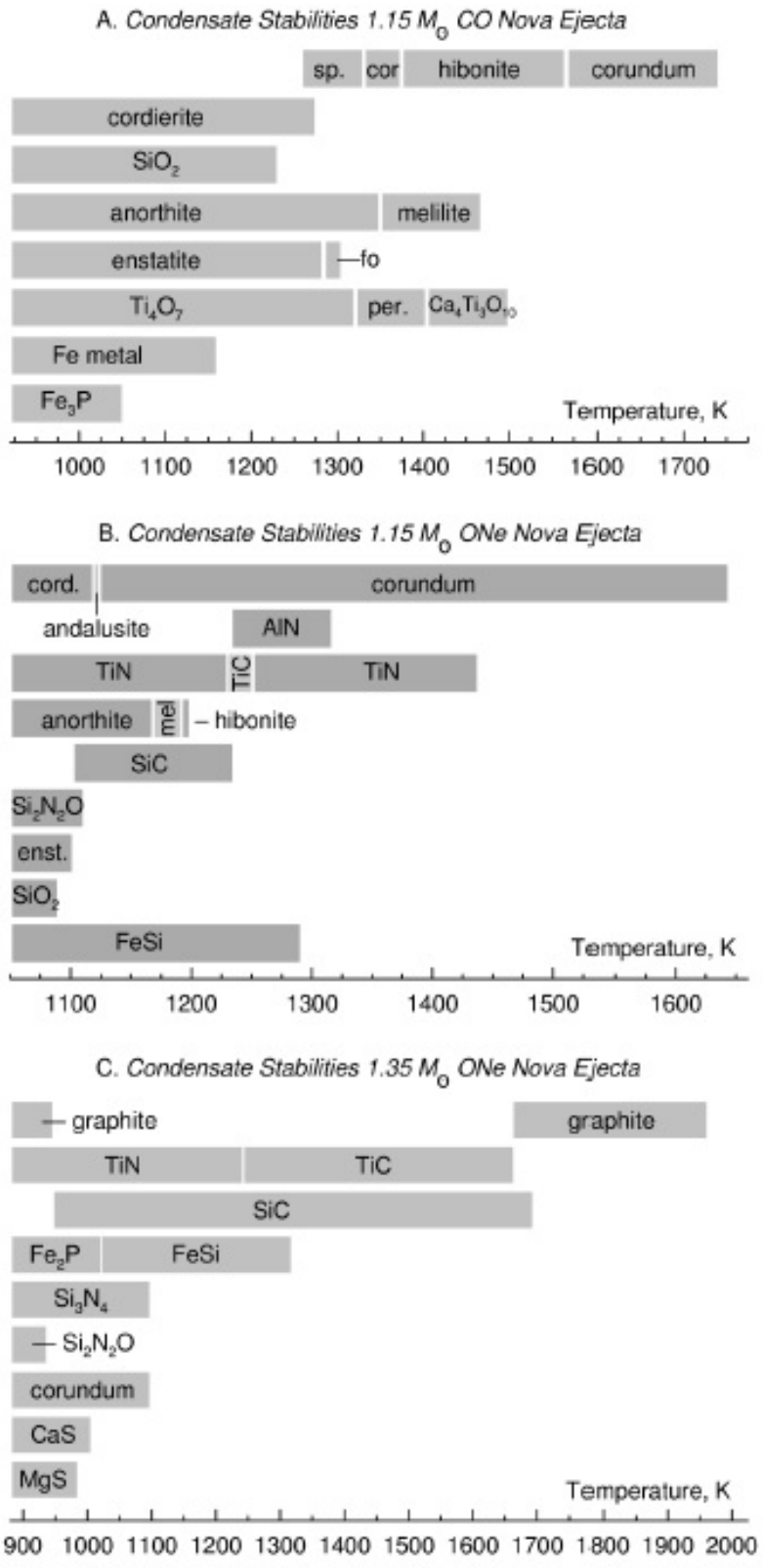

Figure 1.3 *The different types of solar grains expected to form in the ejecta of a nova outburst with a 1.15 $M_\odot$ CO white dwarf, a 1.15 $M_\odot$ ONe white dwarf and a 1.35 $M_\odot$ ONe white dwarf, from Ref. [22].*

product of the β^+-decay of ^{29}P. Ref. [28] looked at the differing abundances of ^{29,30}Si when the $^{29}\mathrm{P}(p,\gamma)^{30}\mathrm{S}$ reaction rate was varied within the current limits, finding a factor of 3 variation in the ^{29,30}Si abundances. In order to improve the limits of the $^{29}\mathrm{P}(p,\gamma)^{30}\mathrm{S}$ reaction rate, more nuclear information on the isotope ^{30}S needs to be obtained.

1.2 X-ray Bursters

X-ray bursters are one of the most explosive events in the galaxy, characterised by a sudden increase in X-rays over ∼10 - 100 s, emitting an energy of $\sim 10^{40}$ ergs [4, 7]. X-ray bursters were first reported in 1976 by Grindlay *et al.* [29]. These sudden bursts are repeated normally on a consistent timescale with a recurrence rate of anything from hours to days. Fig. 1.4 displays the periodic bursts of energy for the GS 1826-238 X-ray burster. In our galaxy we know of ∼60 X-ray bursters [7]. Energy generation associated with a neutron star is up to 7 MeV/nucleon, however, due to the great gravitational potential of the neutron star 200 MeV/nucleon is required for matter to be released and as such no matter is emitted during an X-ray burst [7].

X-ray bursts occur in a close binary system with a weakly magnetic ($B \ll 10^{11}$ G) neutron star and a companion star, where mass is transferred from the companion star onto the surface of the neutron star. Mass transfer from the companion star onto the surface of the neutron star is believed to occur through Roche lobe overflow [31]. The typical accretion rate is less than 10^{-9} $M_\odot$/yr [32]. A thin layer of surface matter is continuously accreted onto the surface of the neutron star and is compressed by the freshly accreted material until the temperature and density are such that nuclear reactions are ignited in the electron degenerate gas conditions. The matter accreted onto the neutron star is normally a mix of hydrogen and helium as well as some heavier elements [7].

It is believed that the hot CNO cycles are important for mass accretion between bursts [24]. The hot CNO cycles convert some of the accreted hydrogen into helium, thereby changing the chemical composition of the surface layer for thermonuclear explosions. For accretion rates considered high, near or above the Eddington limit [33], where the Eddington accretion rate is the rate at which the neutron star radiates at the Eddington luminosity, ($\dot{m}_{Edd} \sim 8.7 \times 10^4$ gs^{-1}cm^{-2}), hydrogen and helium burning is thermally stable at the surface of the accreting

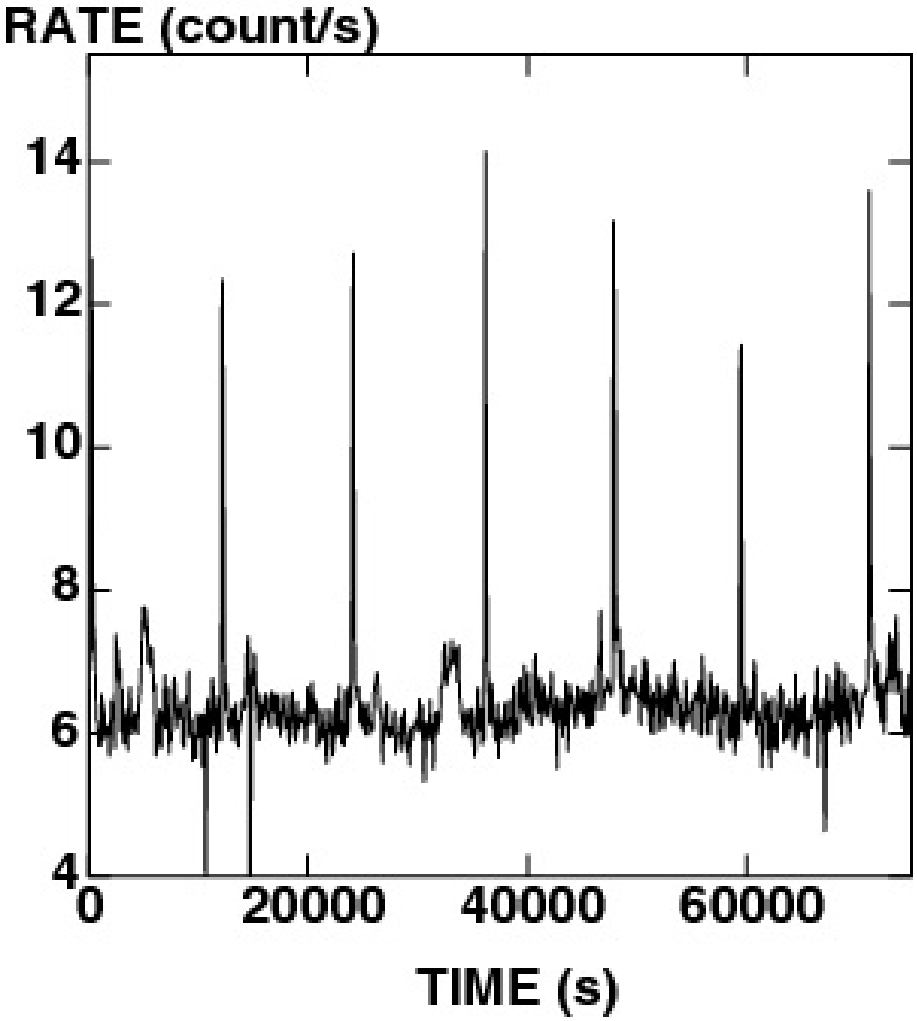

Figure 1.4 *Light curves from the X-ray burster GS 1826-238, showing consistant periodic bursts of energy [30].*

neutron star [34–39]. These high accretion rates can occur on weakly magnetic neutron stars globally with accretion rates in excess of 10^{-8} $M_{\odot}$/yr, and locally on the polar caps of strongly magnetic neutron stars due to infalling material on magnetic field lines (known as X-ray pulsars) [4]. This steady state burning can impact greatly on the composition of the ocean and the crust on the surface of a neutron star [38, 40], as well as impacting the stars seismology [41], thermal structure and magnetic evolution. The steady state hydrogen burning is limited by the amount of CNO seed nuclei present in the accreted material.
When temperatures are greater than ∼0.2 GK the helium accreted is ignited through the triple-α process [42], which has a very strong temperature dependence [7]. Triple-α burning occurs in a very thin shell where the temperature increase cannot be compensated for by readjusting the stellar structure or through surface cooling. In a very fast runaway it is possible for the temperature to increase above 0.5 GK, connecting the CNO cycles to the advanced hydrogen burning cycles [7]. Hydrogen burning is energetically more efficient than helium burning and as such when hydrogen burning is ignited it carries the energy generation of the burst [7]. Once the NeNa cycle is ignited a sequence of (p,γ),(α,p) reactions and β^+ decays, known as the αp process, allows the reaction flow to reach ^{40}Ca [7]. Temperatures in the αp process can reach in excess of 10^9 K, allowing the remaining hydrogen to be burnt onto heavier nuclei. The reaction sequence then consists of rapid proton capture reactions and β^+ decays, known as the rp process [5]. The flux of X-rays observed comes from the thermal emission of the neutron star, which is heated dramatically during the burst [7].

1.2.1 Breakout from the Hot CNO Cycle

Breakout from the hot CNO cycles within the accretion envelope on neutron stars and white dwarfs in a binary star system can only occur when there is a great enough increase in temperature and density, in turn causing an even greater increase in energy. The increase in the energy production rate can only occur when the proton unbound drip line isotopes ^{15}F, ^{16}F and ^{19}Na are bridged, either through α-capture or two-proton capture [4]. There are three reactions through which α-capture can occur, ^{14}O$(\alpha,p)^{17}$F, ^{15}O$(\alpha,\gamma)^{19}$Ne and ^{18}Ne$(\alpha,p)^{21}$Na [5]. Due to the high Coulomb barrier involved in α-capture the cross sections of these reactions are small requiring very high temperatures. For temperatures less than ∼0.3 GK the hot CNO cycles are closed [4]. When temperatures exceed

$\sim$0.4 GK a considerable breakout occurs via the ^{15}O(α,γ)^{19}Ne reaction [43]. At temperatures above $\sim$0.6 GK the hot CNO cycles are open and breakout occurs mainly via the ^{15}O(α,γ)^{19}Ne and ^{18}Ne$(\alpha, p)^{21}$Na reactions [43]. Two-proton capture reactions can also occur on ^{15}O and ^{18}Ne, however, these are three particle interactions and as such require very high density [44, 45] [4].
The ^{19}Ne$(p, \gamma)^{20}$Na reaction leads on from the ^{15}O(α,γ)^{19}Ne reaction and it links the nuclear reactions in the CNO mass range, A $\leq$ 19, to the reactions in the Ne-Na cycles, the αp process and the rp-process, A $\geq$ 20, shown in Fig. 1.5. Temperature and density needs to be great enough in order for the ^{19}Ne$(p, \gamma)^{20}$Na reaction to compete with the β-decay rate of ^{19}Ne.
The ^{19}Ne$(p, \gamma)^{20}$Na reaction was first suggested to be important in Wallace and Woosley's 1981 publication "Explosive Hydrogen Burning" [5]. This was a very extensive theory paper looking at energy generation in hydrogen-rich astrophysical sites at temperatures greater than 10^8 K. The rp-process is identified for the first time in this paper and the production of heavy elements in explosive astrophysical sites is discussed. The ^{19}Ne$(p, \gamma)^{20}$Na reaction is highlighted as an important reaction for the breakout from the hot CNO cycles into the newly identified rp-process. An analysis of the ^{19}Ne$(p, \gamma)^{20}$Na reaction rate is performed, mostly using information from the mirror nucleus ^{20}F. A low energy resonance at E_{ex} = 2.89 MeV was predicted to dominate the reaction rate at temperatures around 0.3 GK [5]. A slightly later paper by Langanke *et al.* [46] concentrated more on the ^{19}Ne$(p, \gamma)^{20}$Na reaction rate and found an increase in the reaction rate for temperatures $T_9 \leq 0.9$ K. Since then there has been much interest in the astrophysically important nucleus ^{20}Na, which will be discussed in much more detail in Chapter 3.

1.2.2 Type 1 X-ray Bursters and Waiting Points

Within X-ray bursters the energy generation, nucleosynthesis, duration and light curve of the burst are very sensitive to the flow through waiting points along the rp and αp process paths [47–49]. Waiting points occur when there is a significant build up on an isotope due to the next reaction or decay in the sequence having a relatively slower timescale and as such the flow of reactions is delayed. From network calculations ^{30}S is shown to be a waiting point with a β-decay half life of $t_{1/2}$ = 1.178 s [47, 50]. The long half life of ^{30}S, comparable to the typical time of the burst rise of a few seconds, combined with (p, γ)-(γ, p) equilibrium between ^{30}S

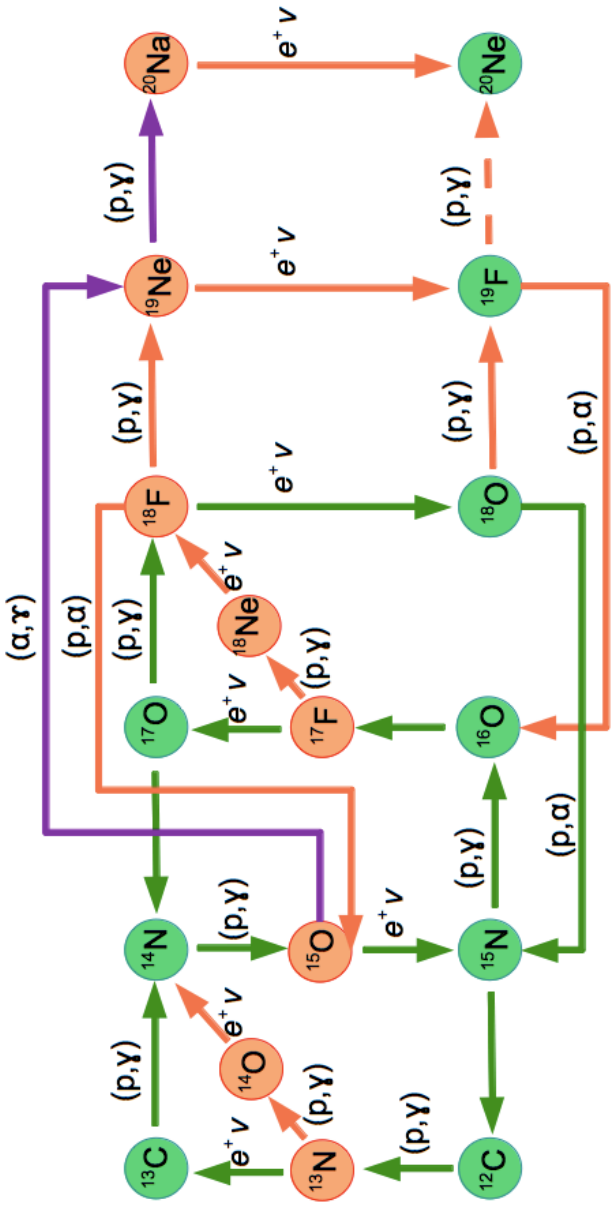

Figure 1.5 *The hot CNO cycles with the breakout reaction sequence* $^{15}O(\alpha,\gamma)^{19}Ne(p,\gamma)^{20}Na$ *indicated by the purple arrows [4].*

and ^{31}Cl, results in a bottle neck for the reaction flow. Two reaction sequences can produce ^{30}S in this environment, $^{27}\mathrm{Si}(p,\gamma)^{28}\mathrm{P}(p,\gamma)^{29}\mathrm{S}(\beta^{+}\nu)^{29}\mathrm{P}(p,\gamma)^{30}\mathrm{S}$ or $^{26}\mathrm{Si}(\alpha,p)^{29}\mathrm{P}(p,\gamma)^{30}\mathrm{S}$. Which reaction sequence occurs depends on the phase and location of the explosive burning [47]. No matter which sequence leads to ^{30}S, the reaction $^{29}\mathrm{P}(p,\gamma)^{30}\mathrm{S}$ is present in both and is therefore important for the overall flow as the burst approaches its peak.

The two reactions $^{19}\mathrm{Ne}(p,\gamma)^{20}\mathrm{Na}$ and $^{29}\mathrm{P}(p,\gamma)^{30}\mathrm{S}$ have been highlighted in this chapter as they are important for explosive binary star systems and will be the focus of this thesis. Chapter 2 will explain some of the nuclear physics required to understand the impact of these reactions upon astrophysical reaction rates and the indirect methods used to study them.

Chapter 2

Thermonuclear Reaction Rates

To determine the rates of the reactions highlighted in Chapter 1, an in depth knowledge of thermonuclear reaction rates is required. This chapter will discuss the general properties of thermonuclear reaction rates in relation to non-resonant and resonant stellar reactions. Additionally, indirect experimental methods for determining stellar reaction rates, such as β-delayed proton emission, will also be discussed.

2.1 Basic Nuclear Reactions

A basic nuclear reaction can be represented by,

$$a + X \rightarrow Y + b \tag{2.1}$$

or,

$$X(a, b)Y \tag{2.2}$$

where a particle "a" collides with a particle "X" to form particle "Y" and particle "b". "X" and "Y" are usually heavier elements, with "a" and "b" usually nucleons or light nuclei, although "a" and "b" can also be γ-rays. When the entrance channel reactants "a" and "X" are in their ground states with masses M_a and M_X, and the exit channel products are in their ground states with masses M_b and M_Y, the Q-value is,

$$Q = (M_a + M_X - M_b - M_Y)c^2. \tag{2.3}$$

If the energy released is positive then the reaction is said to be exothermic and no energy is required for the reaction to occur. If the energy released is negative then the reaction is said to be endothermic and energy must be supplied to the system for the reaction to occur.

2.2 Stellar Reaction Rates

Before discussing stellar reaction rates it is important to first understand nuclear reaction cross sections. Nuclear reaction cross sections, σ, are a measure of probability that a given nuclear reaction will take place. Generally, nuclear reaction cross sections depend on the relative velocity, v, of the target and projectile system, $\sigma = \sigma(v)$. For the most basic nuclear reaction, X(a,b)Y, where there are N_X of "X" particles per cm^3 and N_a per cm^3 of "a" particles, with "a" and "X" at rest and moving with relative velocity v, the reaction rate is given by,

$$r_{aX}(v) = N_a N_X v \sigma(v) \tag{2.4}$$

in units of reactions per cm^3 per second. Within a stellar plasma, the interacting nuclei have varying velocities described by the probability function,

$$\int_0^\infty P(v)dv = 1. \tag{2.5}$$

This can be used to generalise the reaction rate for a distribution of relative velocities within a stellar plasma,

$$r_{aX} = N_a N_X \int_0^\infty v P(v) \sigma(v) dv. \tag{2.6}$$

For exothermic reactions the integral extends from $v = 0$ to $v = \infty$. The reaction rate is therefore,

$$r_{aX} = N_a N_X < \sigma v >_{aX} \tag{2.7}$$

where $< \sigma v >_{aX}$ is the reaction rate per particle pair and $N_a N_X$ is the total number density of pairs of nonidentical "a" and "X" [51]. However, in practise this gets simplified to,

$$r_{aX} = N_A < \sigma v >_{aX} \tag{2.8}$$

where N_A is the Avogadro constant and r_{aX} is expressed in $cm^3mol^{-1}s^{-1}$.
Within normal stellar matter the nuclei travel non-relativistically and are non-degenerate [51]. Therefore, the relative velocities for interacting nuclei in stellar plasmas can be described by the Maxwell-Boltzmann distribution,

$$P(v) = 4\pi v^2 \left(\frac{\mu}{2\pi kT}\right)^{3/2} exp\left(-\frac{\mu v^2}{2kT}\right) \tag{2.9}$$

where T is the temperature in K, k is the Boltzmann constant and μ is the reduced mass. The numerator in the exponential term of Eqn. 2.9 represents the kinetic energy of the nucleus and as such, it is possible to express $P(v)$ in terms of energy,

$$P(E) \propto Eexp\left(\frac{-E}{kT}\right). \tag{2.10}$$

By incorporating the Maxwellian distribution and the energy distribution, the reaction rate per particle pair is found to be,

$$< \sigma v >= \int P(v)\sigma(v)vdv = \int P(E)\sigma(E)vdE \tag{2.11}$$

$$< \sigma v >= \left(\frac{8}{\pi\mu}\right)^{1/2} \frac{1}{(kT)^{3/2}} \int_0^\infty \sigma(E)Eexp\left(-\frac{E}{kT}\right) dE. \tag{2.12}$$

This equation shows clearly that the reaction rate critically depends on the energy dependant cross section σ(E), which in turn is dependant on the reaction mechanism [52].
If the energy dependence of the cross section is "simple" then the reaction rate can be calculated analytically. However, in some situations the cross section is not known explicitly and cannot be integrated analytically. Here the reaction rate needs to extrapolated to the region of interest.

2.2.1 Non-Resonant Reaction Rates

In order for a nuclear reaction to occur, the nuclei involved must reach the nuclear interaction radius, r_0. The interacting nuclei are positively charged and as such, repel each other with a force proportional to the nuclear charge. The Coulomb potential barrier due to the positive charge of the nuclei is shown in Fig. 2.1 and has the form,

$$V_c(r) = \frac{Z_1 Z_2 e^2}{r}. \tag{2.13}$$

The effective potential barrier is a combination of the Coulomb potential and the relative orbital angular momentum, known as the centrifugal potential,

$$V_{c.f}(r) = \frac{l(l+1)\hbar^2}{2\mu r^2} \tag{2.14}$$

where l is the orbital angular momentum. There is a probability that a particle

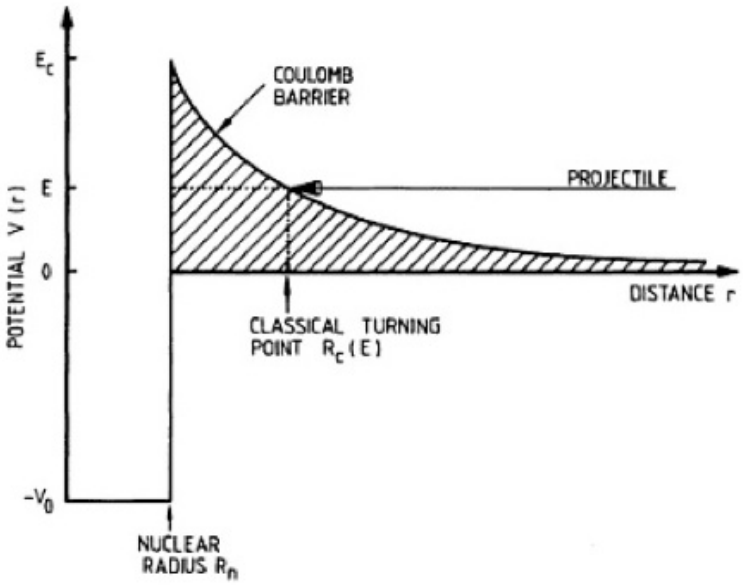

Figure 2.1 *Schematic diagram showing the Coulomb barrier for a nucleus [51].*

with energy E < E_C can penetrate the Coulomb barrier [53], where E_C is the energy required to overcome the Coulomb barrier, shown in Fig. 2.1. The typical energy of particles in stellar interiors is much less than the energy of the Coulomb barrier and the probability of the particle penetrating the wall can be described by the Gamow factor,

$$P = exp(-2\pi\eta) \tag{2.15}$$

where η is called the Sommerfeld parameter and is equal to,

$$\eta = \frac{Z_1 Z_2 e^2}{\hbar\mu} \tag{2.16}$$

and in numerical units,

$$2\pi\eta = 31.29 Z_1 Z_2 \left(\frac{\mu}{E}\right)^{1/2} \tag{2.17}$$

where E is the centre of mass energy in keV and μ the reduced mass in amu. The probability for tunnelling to occur is proportional to the energy-dependent

nuclear reaction cross section σ(E) for charged-particle induced nuclear reactions,

$$\sigma(E) \propto exp(-2\pi\eta). \tag{2.18}$$

The cross section for charge-particle-induced nuclear reactions drops rapidly for energies below E_C. This makes extrapolating the reaction rate down to low energies found in stellar interiors unreliable. This has lead to the formulation of a new value that drops more constantly at low energies depending on the type of reaction, the S-factor. Fig. 2.2 shows how the cross section and S-factor varies with the laboratory proton energy for the $^{12}C(p,\gamma)^{13}N$ reaction. The S-factor contains all the strictly nuclear structure information and is related to the cross section by,

$$\sigma(E) = \frac{1}{E} exp(-2\pi\eta) S(E). \tag{2.19}$$

If we put the S-factor into Eqn. 2.12 the reaction rate equation becomes,

$$< \sigma v >= \left(\frac{8}{\pi\mu}\right)^{1/2} \frac{1}{(kT)^{3/2}} \int_0^\infty S(E) exp\left(-\frac{E}{kT} - \frac{b}{E^{1/2}}\right) dE \tag{2.20}$$

where b arises from the barrier penetrability and is given by,

$$b = (2\mu)^{1/2} \pi e^2 \frac{Z_1 Z_2}{\hbar} = 0.989 Z_1 Z \mu^{1/2} (MeV)^{1/2} \tag{2.21}$$

where b^2 is also known as the Gamow energy, E_G. The reaction rate per particle pair then becomes,

$$< \sigma v >= \left(\frac{8}{\pi\mu}\right)^{1/2} \frac{1}{(kT)^{3/2}} \int_0^\infty S(E) exp\left[-\frac{E}{kT} - \left(\frac{E_G}{E}\right)^{1/2}\right] dE. \tag{2.22}$$

The energy dependence of the integrand is governed by the two terms in the exponential. The $exp[-(E_G/E)^{1/2}]$ term comes from the penetration through the Coulomb barrier, which at low energies becomes very small. The $exp(-E/kT)$ term corresponds to a measure of the number of particles available in the high-energy tail of the Maxwell-Boltzmann distribution and vanishes at high energy [51]. The product of the peak of the integral near an energy E_0, which is much larger than kT, is known as the Gamow peak, shown in Fig. 2.3. For any given T, the width of the Gamow peak, ΔE, represents the narrow energy where nuclear reactions are likely to take place. Over ΔE the S factor is roughly constant,

$$S(E) = S(E_0) = constant \tag{2.23}$$

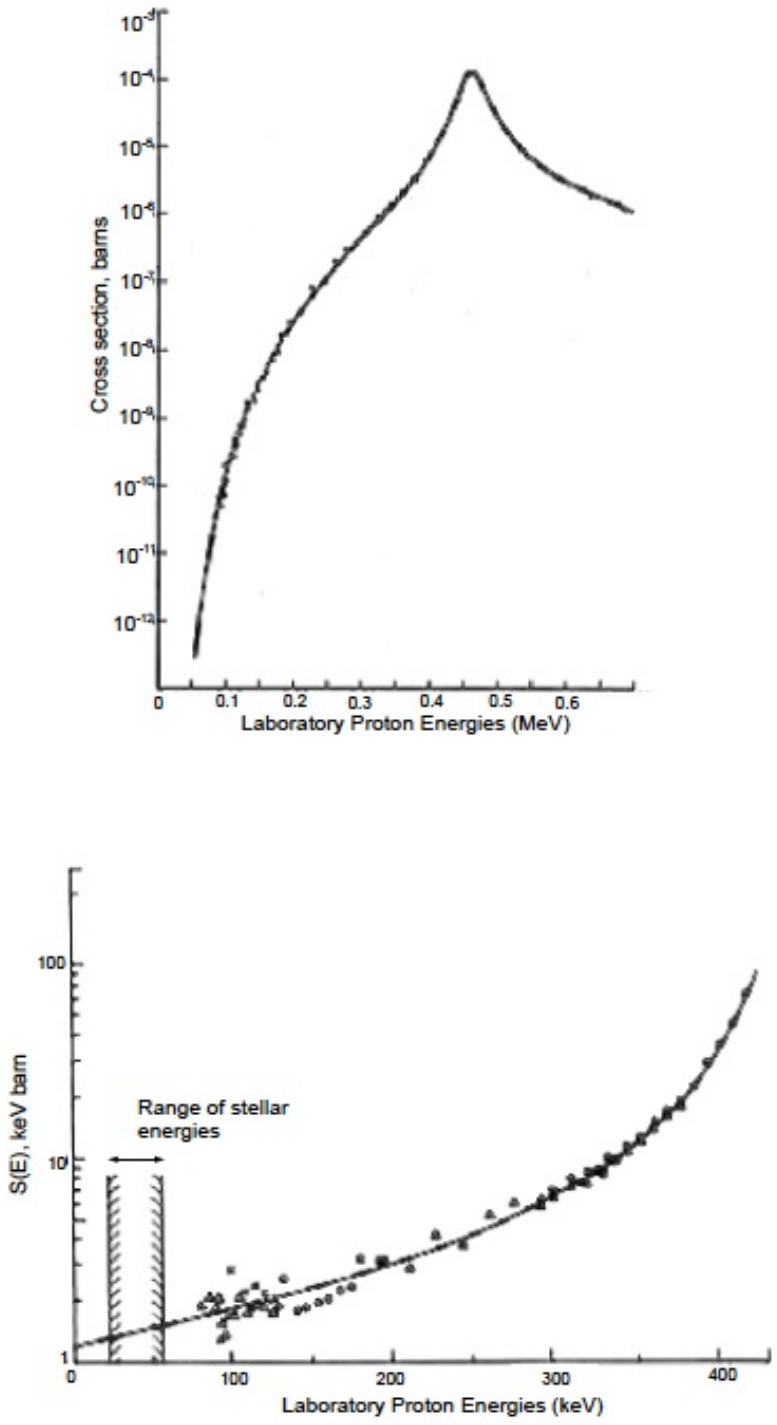

Figure 2.2 *Cross section (above) and S-factor (below) varying with the laboratory proton energy for the* $^{12}C(p,\gamma)^{13}N$ *reaction [54]. The region of interest for stellar environments lies just beyond the region where experiments are possible and as such the S-factor needs to be extrapolated to lower energies.*

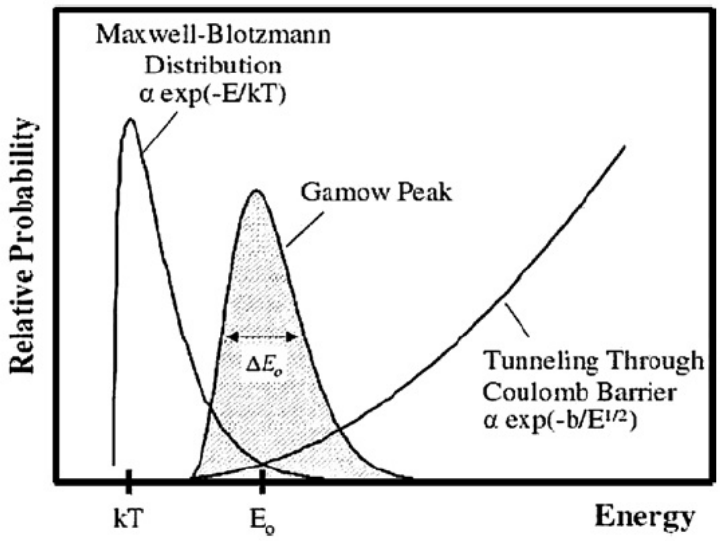

Figure 2.3 *Diagram indicating the Gamow Peak, the region where nuclear reactions are likely to take place [55].*

and as such the reaction rate is reduced to,

$$< \sigma v >= \left(\frac{8}{\pi\mu}\right)^{1/2} \frac{1}{(kT)^{3/2}} S(E_0) \int_0^\infty exp\left[-\frac{E}{kT} - \left(\frac{E_G}{E}\right)^{1/2}\right] dE. \quad (2.24)$$

The energy E_0 is found by taking the first derivative of the integrand of Eqn. 2.24,

$$E_0 = \left(\frac{bkT}{2}\right)^{2/3}. \quad (2.25)$$

Taking the second derivative of the approximate integrand in Eqn. 2.24 gives the effective width of the Gamow energy window as,

$$\Delta E_0 = \frac{4}{3^{1/2}} (E_0 kT)^{1/2}. \quad (2.26)$$

The S-factor is an extremely useful quantity for non-resonant reactions. There are cases however where resonances dominate the reaction rate and as such, the S-factor varies greatly.

2.2.2 Resonant Reaction Rates

Resonant reactions can only occur when the centre of mass kinetic energy of "a" and "X" coincide with the energy of one of the quasi-stationary excited states of the compound nucleus. The majority of resonant reactions are dominated by isolated narrow resonances, where the S-factor varies strongly and particle partial widths are approximately constant over the total resonance energy width, Γ. If we consider the most basic resonance reaction,

$$a + X \rightarrow W^* \rightarrow Y + b \quad (2.27)$$

where "a" and "X" are the primary particles, which combine to make "W" in an excited state, which then decays to "Y" and "b". There is another value that must be considered, the angular momentum J_n of the excited state E_n, which from conservation of angular momentum is known to equal,

$$\mathbf{J}_n = \mathbf{J}_a + \mathbf{J}_X + \mathbf{L} \quad (2.28)$$

where $\mathbf{L}$ is the orbital angular momentum of "a" relative to "X" and the standard vector rules apply.

Quasi-stationary states can exist when the potential barrier is high enough, giving the states relatively long lifetimes against break-up. However, quasi-stationary states are said to be "unbound" as they are formed by and can decay to "a" and "X" with positive kinetic energy. As the excitation energy increases, particle decay becomes favourable and the lifetimes of the resonant states shorten.
The energy-dependent cross section of isolated resonances can be described by the Breit-Wigner formula for a single-level resonance,

$$\sigma(E)_{BW} = \frac{\lambda^2}{4\pi}\frac{(2J+1)}{(2J_X+1)(2J_a+1)}(1+\delta_{Xa})\frac{\Gamma_a\Gamma_b}{(E_r-E)^2+\Gamma^2/4} \tag{2.29}$$

where,

$$\lambda = \frac{2\pi\hbar}{\sqrt{2\mu E}} \tag{2.30}$$

and J_X and J_a are the spins of the target and projectile respectively, J and E_r is the spin and energy of the resonance, E is the centre of mass energy, Γ_a and Γ_b are the particle partial widths of "a" and "b" and Γ is the total resonance width. δ_{Xa} is included to account for the case of identical entrance channel nuclei, which increases the cross section by a factor of 2. Eqn. 2.29 is only valid for isolated resonances, defined by the large separation of levels compared to the total width. Resonances are defined as "narrow" when the width of the resonance is much smaller than the resonance energy.
The type of reactions investigated in this thesis are proton capture reactions. These types of reactions are critical for explosive astrophysical environments and often involve radioactive proton-rich nuclei. The total resonance width for a radiative proton capture reaction is just the sum of the two particle partial widths, Γ_p and Γ_γ, simply,

$$\Gamma = \Gamma_p + \Gamma_\gamma. \tag{2.31}$$

For narrow resonances the stellar reaction rate per particle pair can be written as,

$$< \sigma v >= \left(\frac{8}{\pi\mu}\right)^{1/2}\frac{1}{(kT)^{3/2}}\int_0^\infty \sigma_{BW}(E)Eexp\left(-\frac{E}{kT}\right)dE \tag{2.32}$$

$$< \sigma v >= \frac{\sqrt{2\pi}\hbar^2}{(\mu kT)^{3/2}}\omega\int_0^\infty \frac{\Gamma_p\Gamma_\gamma}{(E_r-E)^2+\Gamma^2/4}exp\left(-\frac{E}{kT}\right)dE \tag{2.33}$$

where the statistical factor ω is,

$$\omega = \frac{(2J_R+1)}{(2J_p+1)(2J_T+1)} \tag{2.34}$$

where J_R, J_p and J_T are the spins of the resonance, projectile and target respectively. For sufficiently narrow resonances, the Maxwell-Boltzmann factor, the particle partial widths Γ_p and Γ_γ and the total resonance width are approximately constant and therefore for $\mathrm{E} = \mathrm{E}_r$ these values can be taken outside of the integral. The reaction rate becomes,

$$< \sigma v >= \frac{\sqrt{2\pi}\hbar^2}{(\mu kT)^{3/2}} exp\left(-\frac{E_r}{kT}\right) \omega \frac{\Gamma_p \Gamma_\gamma}{\Gamma} 2 \int_0^\infty \frac{\Gamma/2}{(E_r - E)^2 + \Gamma^2/4} dE \tag{2.35}$$

$$< \sigma v >= \frac{\sqrt{2\pi}\hbar^2}{(\mu kT)^{3/2}} exp\left(-\frac{E_r}{kT}\right) \omega \frac{\Gamma_p \Gamma_\gamma}{\Gamma} 2\pi \tag{2.36}$$

$$< \sigma v >= \left(\frac{2\pi}{\mu kT}\right)^{3/2} \hbar^2 exp\left(-\frac{E_r}{kT}\right) \omega\gamma \tag{2.37}$$

where,

$$\omega\gamma = \omega \frac{\Gamma_p \Gamma_\gamma}{\Gamma} \tag{2.38}$$

and is known as the resonance strength. The spin and parity of a resonance effect the value of the resonance strength greatly, which in turn effects the reaction rate. If the spin-parity of a resonance is not known confidently then large errors are introduced into the calculation of the reaction rate.

In nuclear reactions in astrophysical scenarios there are normally several narrow and isolated resonances. Generally these can just be summed, and the reaction rate becomes,

$$< \sigma v >= \left(\frac{2\pi}{\mu kT}\right)^{3/2} \hbar^2 \sum_i exp\left(-\frac{E_i}{kT}\right) (\omega\gamma)_i. \tag{2.39}$$

Ideally, all resonance energies and strengths would be measured directly in order to determine stellar reaction rates. As has been previously mentioned, most proton capture reactions involve radioactive nuclei and as such radioactive beams are required to study proton capture reactions directly, however, most of the time this is not possible. For the majority of reactions it is therefore crucial to use indirect methods to determine resonance parameters. Indirect methods are used to determine resonance energies, spins and particle partial widths. From Eqns. 2.34 and 2.38, it is known that the resonance strength is dependant upon spin and particle widths. The spin of the resonance can normally be directly determined in indirect studies and the particle partial widths can be calculated. In proton capture reactions the smaller particle partial width dominates the reaction rate. For resonances lying close to the proton emission threshold the decay is dominated

by γ-ray decay and the resonance strength is therefore dominated by the proton partial width. The proton emission threshold, S_p, is the excitation energy above which proton-decay becomes energetically favourable. Proton partial widths are directly related to the spin of the state and can be calculated using the expression,

$$\Gamma_p = 2\frac{\hbar}{\mu a^2} P_l C^2 S \theta_{sp}^2 \tag{2.40}$$

where a (the interaction radius) is given by,

$$a = r_0(A_t^{1/3} + A_p^{1/3}) \tag{2.41}$$

where A_t is the target mass number, A_p is the projectile mass number, P_l is the barrier penetrability for orbital angular momentum l, μ is the reduced mass, θ_{sp}^2 is the dimensionless single-particle reduced width and C^2S is the spectroscopic factor. The spectroscopic factor is the overlap between the final state wavefunction of Y and the initial state wavefunction of X + p [56]. Spectroscopic factors can be measured in transfer reactions. If spectroscopic factors for resonances in the mirror nucleus have been measured, these can be used within the calculation of the proton partial widths. Spectroscopic factors can also be calculated using the shell model and the reader is referred to Ref. [57] for an example of this. Mirror nuclei will be discussed in Section 2.3.2. For higher lying resonances the decay is dominated by proton decay and the gamma partial width dominates the resonance strength. In this case the lifetime of the analogue states in the mirror nucleus, which is normally stable and it is therefore possible to measure lifetimes of states, are used to calculate the gamma partial width. To estimate the γ-ray partial widths the expression,

$$\Gamma_\gamma = \frac{\hbar l n 2}{t_{1/2}} \tag{2.42}$$

is used, using the half lives from the mirror nuclide.

To summarise, it is possible to measure resonance energies, and resonance parameters needed to calculate the resonance strength through indirect methods. Indirect methods will be the central theme of this thesis.

Table 2.1 *Selection rules for β-decay and the expected logft values. $\Delta\pi$ refers to the change in parity between the initial and final states. Superallowed transitions are where the initial and final states have $J^\pi = 0^+$ and have a logft value of ∼3.5 [58].*

		Fermi		Gamow-Teller		
Transition type	L	ΔI	Δπ	ΔI	Δπ	logft
Allowed	0	0	No	(0),1	No	5.5±1.5
1st forbidden	1	(0),1	Yes	0,1,2	Yes	7.5±1.5
2nd forbidden	2	(1),2	No	2,3	No	∼12
3rd forbidden	3	(2),3	Yes	3,4	Yes	∼16
4th forbidden	4	(3),4	No	4,5	No	∼21

2.3 Indirect Experimental Approaches

2.3.1 β-delayed Proton Emission

The first experiment to be discussed in this thesis is a β-delayed proton decay study of ^{20}Mg. Such studies can measure the energy and spin-parity of resonances and are especially useful for states dominated by proton decay. To understand the kinematics of β-delayed proton emission it is prudent to first understand β-decay.

β-decay occurs when an unstable nucleus emits a β-particle in order to return to stability, optimising the N/Z ratio for a given A, converting a proton within the nucleus into a neutron or vice versa. The Q-value for a β^--decay is,

$$Q_{\beta^-} = (m_N({}^A_Z X) - m_N({}^A_{Z+1} X'))c^2 \tag{2.43}$$

and the Q-value for a β^+-decay,

$$Q_{\beta^+} = (m_N({}^A_Z X) - m_N({}^A_{Z-1} X') - 2m_e)c^2. \tag{2.44}$$

There are two types of β-decay, Gamow-Teller and Fermi. For Gamow-Teller decay the spins of the initial and final states must satisfy $J_f = J_i + l + 1$ and for Fermi decay the spins of the initial and final states must satisfy $J_f = J_i + l$. The change in parity and spin between the initial and final states dictates the strength of the β-decay branch. Table 2.1 shows the different types of transitions for both Fermi and Gamow-Teller β-decay and the expected logft value [58]. The

ft value is a comparative half-life measurement, which can vary over many orders of magnitude so it is customary to take the $\log_{10}$ in order to compare different β-decays over a small scale. Fig. 2.4 shows the logft values for a range of allowed β-decays, highlighting the very low logft value for the doubly magic nucleus ^{100}Sn. For β-delayed proton decay, decay protons are mostly detected from allowed and superallowed transitions due to the low probability of other β-decay transitions occurring. It is possible for β-delayed proton decay to occur when the β-decay is not allowed or superallowed, however the precision of the equipment used to study β-delayed proton decays means that these transitions are very unlikely to be seen. β-delayed proton decay precursors appear on the proton-rich side of the

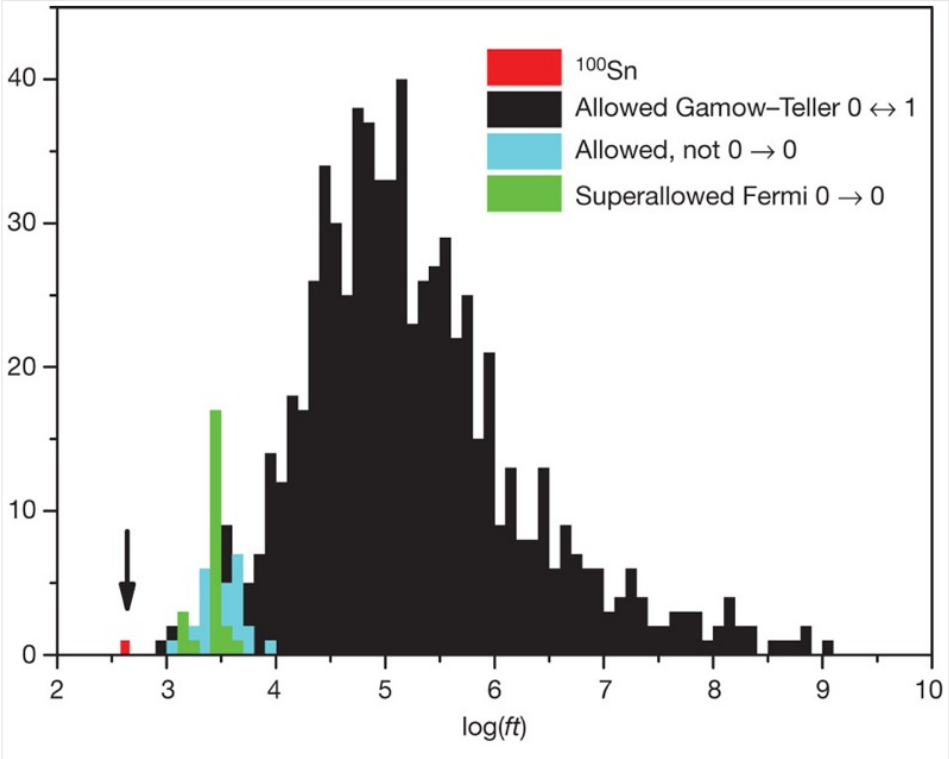

Figure 2.4 *All current allowed β-decay logft values. The doubly magic nucleus ^{100}Sn has an especially low logft value [59].*

line of stability.

The energy of the proton emitted will vary due to the energy of the initial and final states. Fig. 2.5 shows the decay scheme for a general β-delayed proton decay. The β-delayed proton decay of ^{20}Mg is shown in Chapter 3. The intensity of the proton groups depends on two different factors: 1. The intensity of the state in the emitter that is populated by β-decay and 2, the probability that the emitter will decay by proton decay rather than by γ-decay. The first decreases with increasing proton energy, corresponding to decreasing β-energy and the second

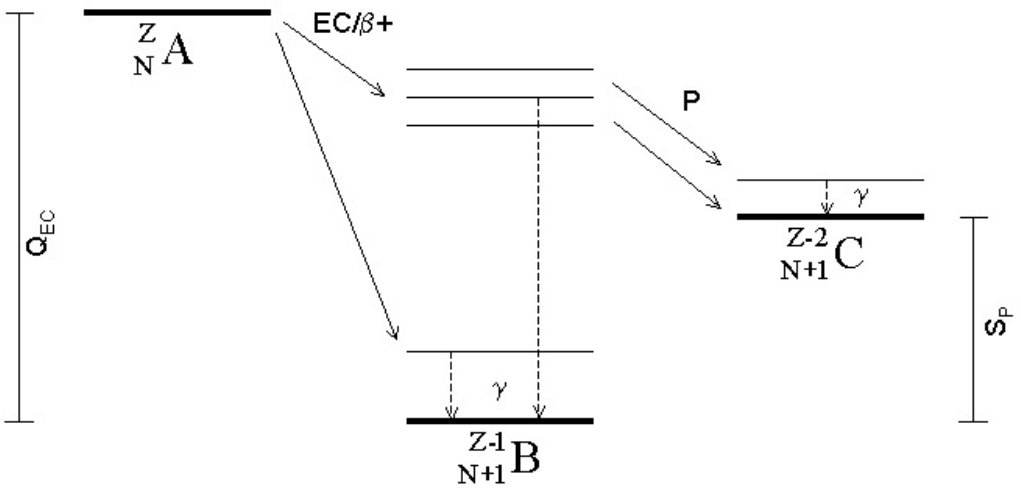

Figure 2.5 *β-delayed proton decay scheme [60]. The nucleus A β^+-decays to the nucleus B, which can then proton decay to the nucleus C.*

increases with increasing proton energy.
If the Q-value and proton emission threshold are large in energy then the proton-emitting states are at a high excitation energy and there is therefore a high level density and the individual states are difficult to distinguish. If the Q-value and proton emission threshold are small in energy then the protons emitted are at lower excitation energy and there is therefore a relatively low level density and the individual protons can be distinguished. The half-life of the β-decay is much longer than the half-life of the proton emission and as such the half-life for the β-delayed proton decay is dominated by the β-decay. If the level density of an isotope is small enough then a β-delayed proton decay study can be a very useful tool to determine energies of resonances. It can also be possible to determine spin-parity assignments if the spin of the initial level is known, using the Fermi and Gamow-Teller selection rules. To determine other resonance parameters such as gamma partial widths, states in the mirror nucleus are studied.

2.3.2 Mirror Nuclei

The isospin formalism describes the neutron and proton as identical particles, with T = 1/2 and T_Z(p) = +1/2 and T_Z(n) = -1/2 [61, 62]. Taking this further one can assume that the structures of nuclei with the same mass A and isospin T are nearly identical. Therefore the nuclear properties of one nucleus can give insight into the nuclear properties of its isobaric analogues. Isobaric nuclei with

the same isospin T are 2T+1 multiplets, with projections of T_Z = (N-Z)/2, where N is the number of neutrons and Z is the number of protons [63].
A special case are mirror nuclei, where the neutron and proton numbers are exchanged. The isospin symmetry is broken by the Coulomb interaction and results in lower total binding energy of nuclear states in one of the mirror nuclei [63]. A connection between the change in binding energy due to the change in states in different isobaric multiplets and the quantum number T was first postulated by Wigner in 1957 [64]. This led to the formulation of the Isobaric Multiplet Mass Equation (IMME) [64],

$$\Delta BE(T, T_Z) = a + bT_Z + cT_z^2 \tag{2.45}$$

where a, b and c are the isoscalar, isovector and isotensor Coulomb energy respectively. IMME also works on excited states.
The absolute binding energy of the ground state can be normalised and therefore the Coulomb energy difference between the excited states can be found as a function of the excitation energy and spin. For mirror nuclei, the energy difference between excited states (MED) is found by,

$$MED_{JT} = E^*_{J,T_Z=-T} - E(Z<N)^*_{J,T_Z=T} = -\Delta b_J \tag{2.46}$$

where J is the total angular momentum of the excited states and Δb_J is the change in the coefficient b as a function of spin in relation to the ground state [65].
The lifetimes and spectroscopic factors of states in one isotope can be used to determine the particle partial widths of analogue states in the mirror, as discussed in Section 2.2.2.

2.3.3 Gamma-ray Spectroscopy

The second experiment that will be described in this thesis is a γ-decay spectroscopy study. In γ-decay, in order to conserve energy, electromagnetic transitions between nuclear states require an emission or absorption of energy,

$$E_i - E_f = \Delta E = E_\gamma + \frac{E_\gamma^2}{2Mc^2} \tag{2.47}$$

where $\frac{E_\gamma^2}{2Mc^2}$ is the energy taken away from the recoiling nucleus. For γ-rays with an energy greater than 1 MeV the recoil of the nucleus becomes comparable to the statistical errors involved in measuring γ-rays and therefore must be taken into account. There must be a conservation of energy within a γ-decay. Gamma-ray energies can be measured to a precision of $\sim$0.01 keV, and as such the locations of states can be determined precisely [66].
There must also be a conservation of angular momentum within a γ-decay. The photon carries away the total angular momentum,

$$L = l + s \tag{2.48}$$

where l is the orbital angular momentum and s is the intrinsic spin, which for real photons s = 1, with a component along the direction of propagation, $s_z = \pm 1$, in units of $\hbar$.
If we take a simple γ-ray transition from an initial state with spin J_i and parity π_i to a final state with spin J_f and parity π_f, then from the law of conservation of angular momentum,

$$J_i = L + J_f \tag{2.49}$$

where J_i, J_f and L form a closed vector triangle. L can only have non-zero integer values, and therefore,

$$|J_i - J_f| \leq L < |J_i + J_f|. \tag{2.50}$$

Single photon emission is forbidden for $J_i = 0$ and $J_f = 0$ transitions [66]. There are two types of γ-ray transitions, electric (EL) which involves oscillating charges and magnetic (ML), involving varying currents. The parity of the initial and final states dictates which type of radiation is emitted,

$$\pi(ML) = (-1)^{L+1} \tag{2.51}$$

$$\pi(EL) = (-1)^{L}. \tag{2.52}$$

When there is no change in parity the transition consists of even electric radiation and odd magnetic radiation, and when there is a change in parity the transition consists of odd electric radiation and even magnetic radiation. The spins of the initial and final states allow for a number of multipoles to be emitted, however from the single-particle Weisskopf estimates the lowest permitted multipoles dominate and only L = 1 and L = 2 need to be considered.
To deduce the multi-polarities of the transitions the angular distribution of the γ rays must be measured. This requires the distribution of the emitted γ

rays with respect to a fixed axis, which in a fusion-evaporation reaction is the beam direction. Fusion-evaporation reactions will be discussed in more detail in Chapter 4. The angular dependence of the γ ray yield is expressed by the directional angular distribution function,

$$W(\theta) = \sum_{k=even}^{2L_{max}} a_k p_k(cos\theta) \tag{2.53}$$

where $a_0 = 1$, $P_k(\cos\theta)$ is the Legendre polynomial and L_{max} denotes the largest multipolarity which contributes to decay [56]. Most states decay by either L = 1 or L = 2 radiation, therefore only $k \leq 4$ need to be considered. Two coefficients are of particular importance, a_2 and a_4, which may be approximated for transitions in which a change of spin between the initial and the final states is ± 2, ± 1 or 0. The approximations show a relationship between a_2 and a_4 [67], shown in Fig. 2.6.

If the angular distribution of the transition can be measured experimentally then it is possible to fit Legendre polynomials. In this thesis the computer programme "LEGFT" was used [68]. The parameters found equal the a_k coefficients of $W(\theta)$ for any given γ-ray transitions and the absolute values of a_2 and a_4 are used to determine changes in spin [56]. The mirror can than be used to determine the parity of states measured, needed to calculate the penetrability factor, which in turn is needed to calculate the proton partial width. The final value needed to calculate the proton partial width is the spectroscopic factor, which as previously mentioned can either be taken from the mirror or can be calculated using the shell model.

In summary, indirect methods can be used to determine resonance energies, spins, spectroscopic factors and particle partials widths, which in turn can be used to calculate stellar reaction rates. The next three chapters will detail the β-delayed proton decay study of ^{20}Mg in order to gain information about the astrophysically important nucleus ^{20}Na, and Chapter 6 will detail the γ-decay spectroscopy study of the astrophysically important nucleus ^{30}S.

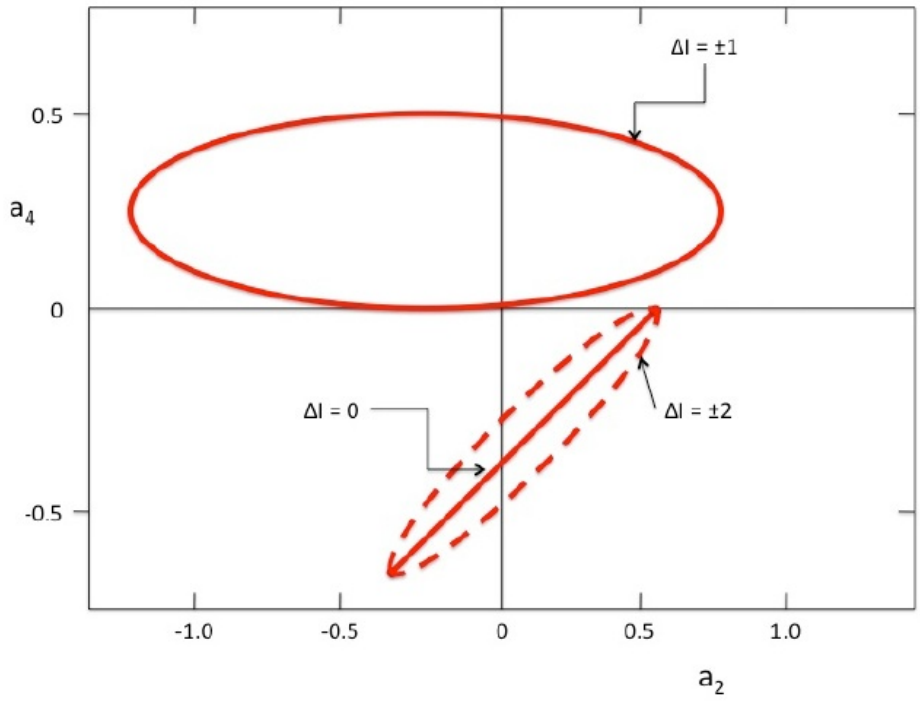

Figure 2.6 *The a_4 versus a_2 coefficients of the angular distribution function $W(\theta)$ [56].*

Chapter 3

Previous Studies of the Level Structure of ^{20}Na

The level structure of ^{20}Na below the proton emission threshold has been studied extensively and is well known. A recent spectroscopic study of in-beam γ-decays by Seweryniak *et al.* [69] populated and identified all states in ^{20}Na below the proton emission threshold, including firm spin-parity assignments, and assigned these states to analogue states in the mirror ^{20}F [69]. The proton emission threshold has also recently been measured to be 2190.1(11) keV, the most accurate measurement to date [70]. However, for the ^{19}Ne$(p,\gamma)^{20}$Na reaction rate at astrophysical temperatures it is the states above the proton emission threshold that are important, as detailed in the theoretical studies by Wallace and Woosley and Langanke *et al.*, mentioned in Chapter 1 [5, 46]. This chapter will detail the vast history of studies on ^{20}Na and the current knowledge and uncertainties for states above the proton emission threshold.

3.1 Charge Exchange Reactions

Langanke *et al.*'s [46] 1986 paper detailing a new estimate for the ^{19}Ne$(p,\gamma)^{20}$Na reaction rate called for more experimental studies to be performed on ^{20}Na to improve the reaction rate estimate as the current knowledge on states in ^{20}Na was very poor. The first of these experimental studies were charge exchange

reactions. Charge exchange reaction studies are very useful as they populate every state in the nucleus and consequently the level structure of the nucleus can be established. It is also possible to obtain some angular distribution information, which can be used to determine spin-parity assignments of the measured states. Lamm *et al.* performed a charge exchange reaction using the FN-Tandem-VdG accelerator at the University of Notre Dame to study the reaction ^{20}Ne(^{3}He,t)^{20}Na. This experiment was first published in the 1987 paper "Level Structure of ^{20}Na near the Proton Threshold" [71] before the data were reanalysed and published in 1990 paper "Level structure of ^{20}Na and the impact upon the stellar reaction rate for ^{19}Ne$(p,\gamma)^{20}$Na" [72]. A ^{3}He beam with energies ranging from 24 - 27 MeV bombarded a gas cell of 95.5% enriched ^{20}Ne gas [72]. Using a magnetic spectrograph the tritons from the charge exchange reaction were measured at angles between 10° - 40°. Sixteen states in ^{20}Na were found, including a low resonant state with excitation energy 2649(15) keV, corresponding to a resonance energy of ∼450 keV [72]. This low resonance energy contradicted one of the points made in Ref. [46], which explicitly said that no resonances below 0.5 MeV were expected. An energy resolution of 80 keV was achieved for the tritons, which related to an error on the excitation energies of ∼15 keV. Fig. 3.1 shows typical spectra from this experiment. For the key resonance at an excitation energy of 2649(15) keV and a small selection of the other states in ^{20}Na, angular distributions were compared to DWBA fits, which were guided by possible analogue states in the mirror ^{20}F and spin-parity assignments were made. The 2649(15) keV state was given a spin-parity assignment of 1^+ and was paired with the 3171 keV 1^+ intruder state in ^{20}F [72].

Independently Kubono *et al.* [73, 74] studied two charge exchange reactions, the ^{20}Ne$(p,n)^{20}$Na reaction at the Cyclotron-Radioisotope Center of Tohoku University and the ^{20}Ne(^{3}He,t)^{20}Na reaction at the Institute for Nuclear Study at the University of Tokyo. Both these studies found a low energy resonance at an excitation energy of 2637(15) keV for the (^{3}He,t) study and at 2651(20) keV for the (p,n) study, with spin-parity assignments of $(0,1)^+$ and 1^+ respectively [73, 74]. The spin-parity assignments were determined using DWBA analysis of the angular distributions of the differential cross sections. The other states found in these two studies agree with the energies found in Ref. [72] within errors. The spin-parity assignment(s) agree for most of the states within the restraints given in each paper except for the state at ∼3.3 MeV, which is given spin assignments of $(4,5,6)^-$ in Ref. [73] and $(1,2)^+$ in Ref. [72].

Another charge exchange reaction was performed in 1990 by Clarke *et al.* [75].

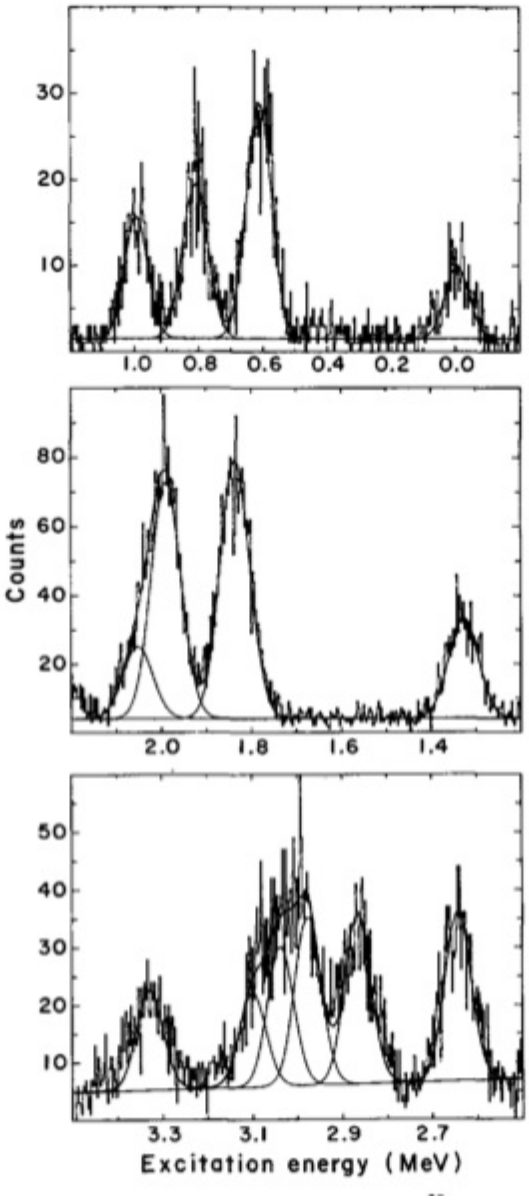

Figure 3.1 *Typical triton spectra from the Lamm et al. charge exchange reaction experiment [72]. These three spectra clearly show the low energy resolution achieved, ∼80 keV.*

Clarke *et al.* performed the analogous charge exchange reactions ^{20}Ne(^{3}He,t)^{20}Na and ^{20}Ne(t,^{3}He)^{20}F, awarding them the unique ability to directly compare ^{20}Na to its mirror ^{20}F. These two experiments were performed at different facilities, with the ^{20}Ne(^{3}He,t)^{20}Na reaction performed at the Radial Ridge Cyclotron, Birmingham and the ^{20}Ne(t,^{3}He)^{20}F reaction performed at the Nuclear Structure Facility, Daresbury. The energy resolution of the two experiments was E_{res} ∼100 keV leading to errors of ∼20 keV for most states. Fig. 3.2 shows the two spectra from these experiments, which look remarkably similar. The key resonance was measured to be at 2640(20) keV in agreement with all the previous charge exchange studies [72–74]. To determine the spin-parities of the states measured in the ^{20}Na study DWBA calculations were performed and compared to the angular distributions of states in ^{20}Na. For the 2640(20) keV state they assign a spin-parity of either 1^+ or 1^-.

However, three years later Clarke *et al.* [76] published a second paper re-examining their previous data. Instead of comparing angular distributions to DWBA calculations, they compared the angular distributions from the ^{20}Ne(^{3}He,t)^{20}Na reaction to angular distributions from the ^{20}Ne(t,^{3}He)^{20}F reaction. Fig. 3.3 shows three comparisons between angular distributions of states in ^{20}Na and states in ^{20}F. The comparison of the ground states is shown to demonstrate the agreement between angular distributions for known mirror states. The other two plots show the ∼2640 keV state compared to both the 3173 and the 2966 keV states in ^{20}F. It is clear from these plots that there is no similarity between the 3173 keV state in ^{20}F and the 2640 keV state in ^{20}Na, even with the large statistical errors for the 3173 keV state. There is a good agreement between the 2966 keV state in ^{20}F and the 2640 keV state in ^{20}Na. The 2966 keV state in ^{20}F has previously been assigned $J^\pi = 3^+$. Clarke *et al.* therefore contradict their earlier paper on the same data and assign the key resonance $J^\pi = 3^+$ [76].

A high precision charge exchange reaction study was performed by Smith *et al.* [77]. Here the ^{20}Ne(^{3}He,t)^{20}Na reaction was studied using a 30 MeV ^{3}He beam produced by the Princeton Universities AVF cyclotron facility and ^{20}Ne implanted transmission targets [77]. A QDDD (quadrupole-dipole-dipole-dipole) magnetic spectrograph was used to analyse the reaction products at a large dispersion (D = 8.72 MeV mm/keV) and a high acceptance (14.7 msr). QDDD magnetic spectrographs provide very accurate measurements of the difference in energy between states. Four states were found in this study, with the key resonance measured to have excitation energy of 2.646(9) MeV [77]. The spectrum gained

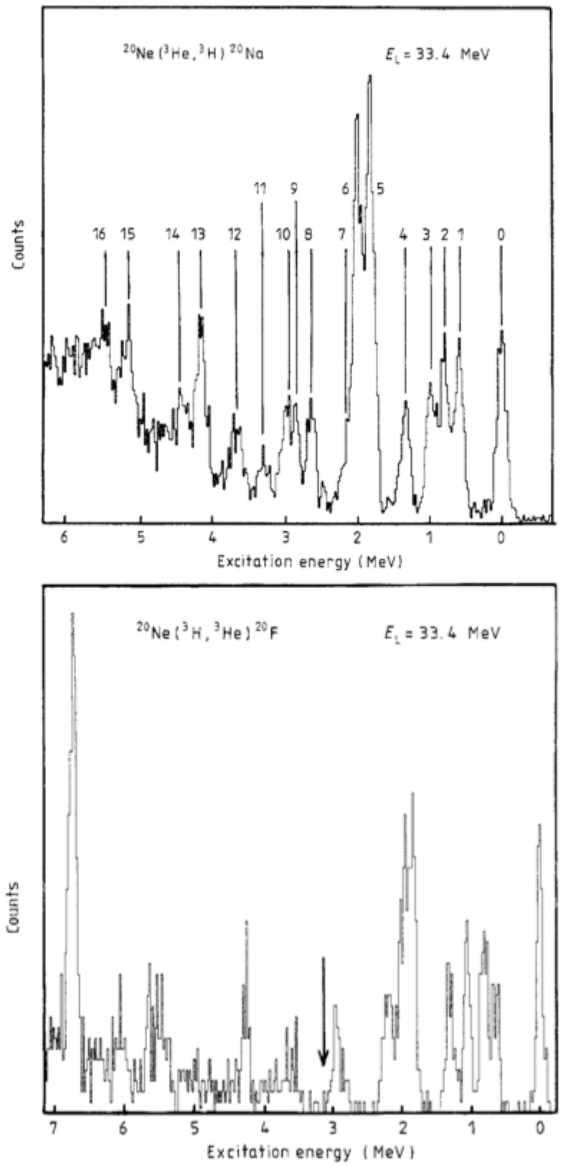

Figure 3.2 *Spectra from the charge exchange reaction study by Clarke et al. [75]. The top spectrum is from the $^{20}Ne(^{3}He,t)^{20}Na$ reaction study and the bottom spectrum is from the $^{20}Ne(t,^{3}He)^{20}F$ reaction study. The arrow in the bottom spectrum shows the position expected for the weakly populated 3173 keV state in ^{20}F [75]. The numbers in the top spectrum correspond to the different levels measured in this study given in Table 1 in Ref. [75]. The resolution in both these studies is relatively poor, with E_{res} ∼100 keV.*

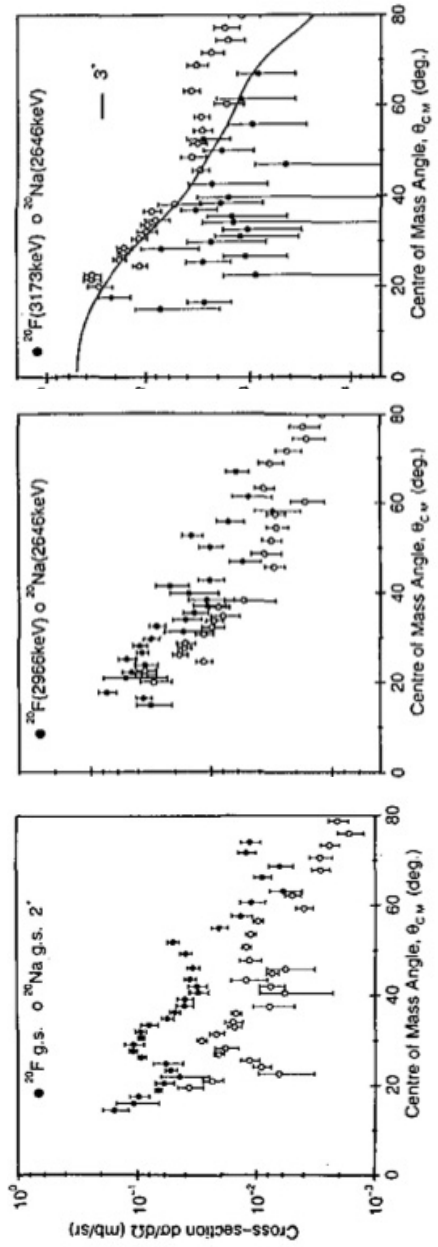

Figure 3.3 *Three plots showing the differential cross sections for the ground states in ^{20}F and ^{20}Na, the 2646 keV state in ^{20}Na and the 3173 keV state in ^{20}F and the 2646 keV state in ^{20}Na and the 2966 keV state in ^{20}F from the charge exchange reactions by Clarke et al. [75]. The large difference between the differential cross section of the 3173 keV state in ^{20}F compared to the 2646 keV state in ^{20}Na is clear. However, there does seem to be a good agreement between the 2966 keV state in ^{20}F and the 2646 keV state in ^{20}Na [76].*

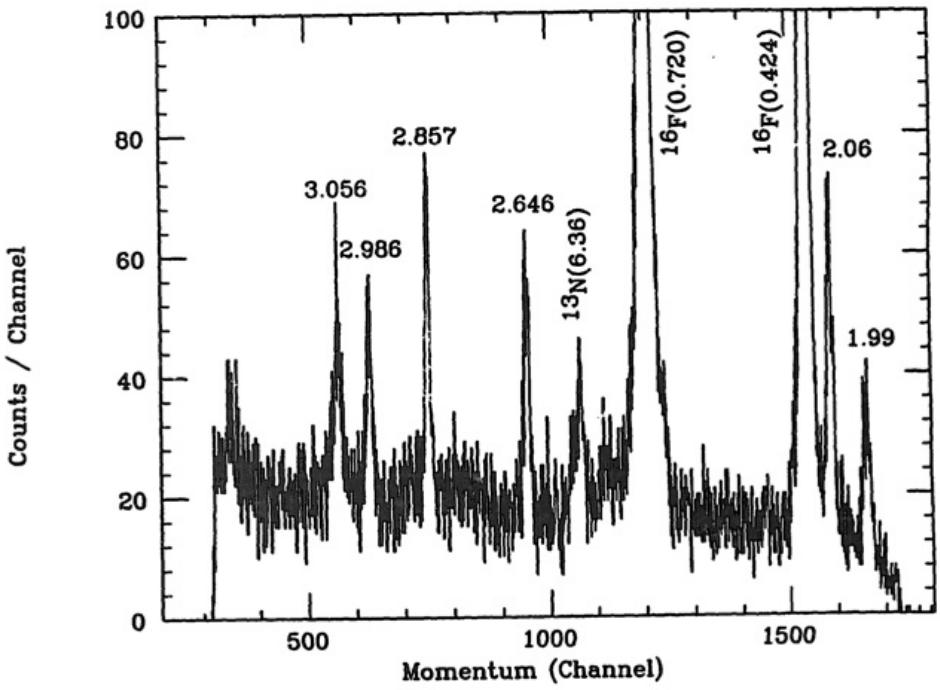

Figure 3.4 *Spectrum from the high precision study by Smith et al. [77]. The energy resolution in this spectrum compared to that of Lamm et al. and Clarke et al. is greatly improved [72, 75].*

from this experiment is shown in Fig. 3.4. This high precision study had limited angles and it was therefore almost impossible for Smith *et al.* to perform angular distributions and determine spin-parity assignments. They do however discuss previous studies [72–74] and place a 1^+ assignment for the key resonance based on these previous studies.

The final charge exchange reaction experiment aimed at finding more information about the level structure of ^{20}Na was performed by Anderson *et al.* at the Indiana University Cyclotron facility [78]. Here the $^{20}\mathrm{Ne}(p,n)^{20}\mathrm{Na}$ reaction was investigated using the beam-swinger neutron time-of-flight facility. The neutrons were detected at three detector stations at three different angles. From the excitation energy spectra obtained in this experiment and DWBA calculations performed, the ∼2645 keV key resonant state was seen to be consistent with $J^\pi = 2^+$ or 3^+ [78].

The charge exchange reaction studies were successful in detailing the basic structure of states above the proton emission threshold in ^{20}Na. However, the different studies found different spin-parity assignment for the key resonance at ∼450 keV, introducing larger errors in the strength of the resonance, which in turn introduced huge uncertainties in the $^{19}\mathrm{Ne}(p,\gamma)^{20}\mathrm{Na}$ reaction rate at astrophysical

temperatures. To measure resonance strengths directly a radioactive ^{19}Ne beam is needed. The next section will discuss direct reaction studies with a radioactive ^{19}Ne beam performed at the Louvain-la-Neuve facility.

3.2 Direct Reactions and Radioactive Beams

By the early 1990s radioactive ^{19}Ne beams became available at the Louvain-la-Neuve facility and therefore direct measurements became possible. Fig. 3.5 shows the layout of the radioactive beam facility at Louvain-la-Neuve. Before any direct measurements of the resonance strength were performed, a theoretical shell model study by Brown *et al.* [80] was completed, which calculated a value for the resonance strength of the first key resonance at ∼450 keV above the proton emission threshold in ^{20}Na. Brown *et al.* compared states in ^{20}Na to those in the mirror nucleus ^{20}F, taking into account the possible configuration of the states as well as how each individual state is populated in charge exchange reactions. They paired the 2646 keV key resonance in ^{20}Na with the 2966 keV 3^+ state in ^{20}F. Brown *et al.* highlighted the consistency between the cross sections of the analogous charge exchange reactions, also highlighted in Ref. [76]. Brown *et al.* calculated the resonance strength for the key resonance based on their spin-parity assignment and on the available knowledge of the mirror state, finding a value of 80 meV for the resonance strength [80].

One of the first experiments to use the newly available radioactive ^{19}Ne beam at Louvain-la-Neuve was performed by Coszach *et al.* [81]. Coszach *et al.* scattered the radioactive ^{19}Ne beam off 200-600 μgcm^{-2} self-supporting polyethylene targets. The protons, recoiling ^{12}C nuclei and the elastically scattered beam particles were measured in two different types of detectors. The first detectors were Passivated Ion-implanted Planar Silicon diode detectors (PIPS) with a thickness of ∼120 μm. These were located at 5 different discrete lab angles. The second detector was a X-Y microstrip detector, from which data were obtained over a continuous angular region of 7° - 14°. From this experiment the energy of two resonances were accurately determined to be 797(2) keV and 887(2) keV [81]. The spin-parity assignments and widths for these resonances were obtained through three parameterization techniques; Breit-Wigner, R and K matrix. All three techniques gave the same result for spin-parity and width values for the 797(2) keV and 887(2) keV resonances within errors, with $J^\pi = 1^+$ and 0^+ and

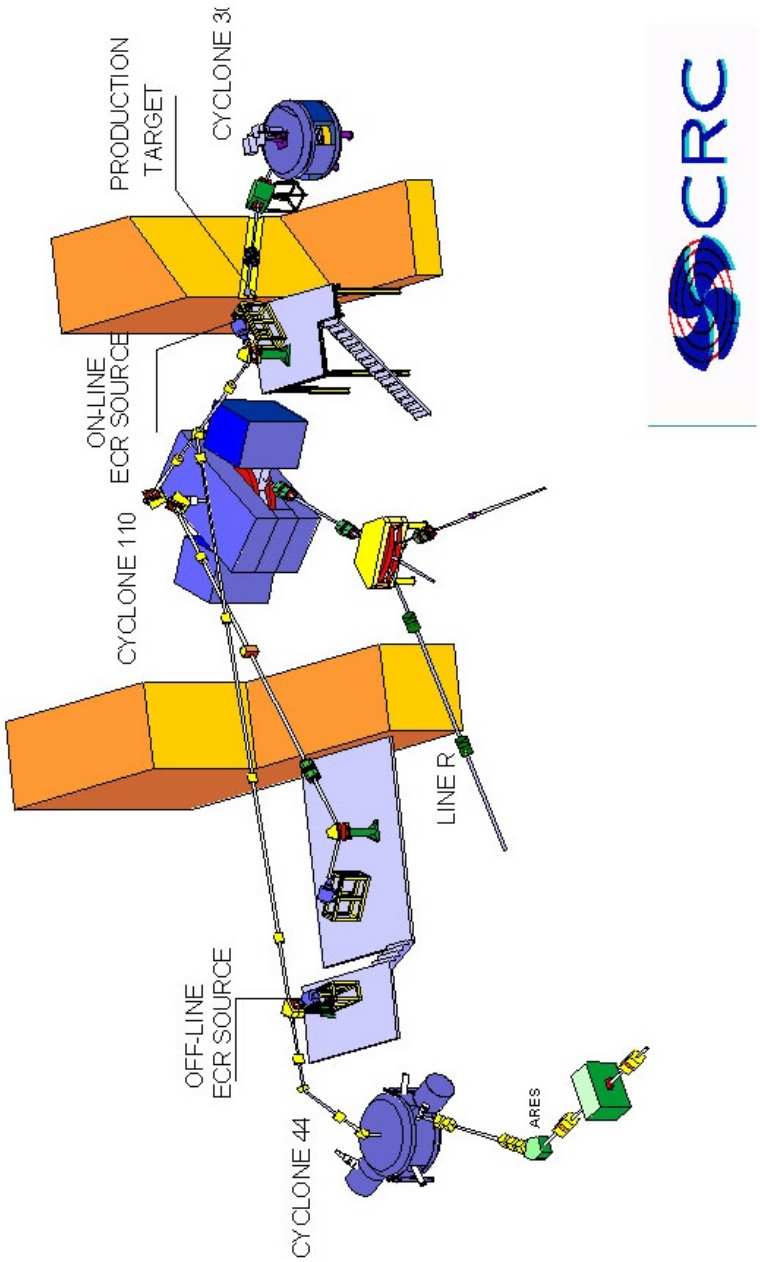

Figure 3.5 *Layout of the radioactive beam facility at Louvain-la-Neuve. Cyclone 30 produces a proton beam, and through reactions with the production target, radioactive beams are produced, which are post-accelerated by cyclone 44 and cyclone 110 [79].*

Γ = 19.8 and 35.9 keV respectively [81].

Around the same time another experiment was independently performed at Louvain-la-Neuve with the radioactive ^{19}Ne beam by Page *et al.* [82]. Here the ^{19}Ne beam was used to measure the β-delayed alpha decay of ^{20}Na, with the ^{19}Ne beam bombarding a polyethylene target in order to produce ^{20}Na ions. Two different detectors, a double sided silicon strip detector (DSSD) and solid state nuclear track detectors (SSNTDs), were utilised in two different techniques in order to investigate the key resonance, which was believed to be at an energy of 447 keV at the time of this experiment. An upper limit of 18 meV with a 90% confidence limit was determined for the resonance strength of the key resonance and the rate of the ^{19}Ne$(p,\gamma)^{20}$Na reaction using these parameters was found to be smaller than previously thought [82].

Further ^{19}Ne radioactive beam studies were performed at the Louvain-la-Neuve facility aimed at gaining more information about low-lying resonances above the proton emission threshold in ^{20}Na. Michotte *et al.* [83] used two different methods, the SSNTD method and the Solenoid and Telescope (STAR) method, in order to measure the cross section of the second, third and fourth resonances above the proton emission threshold in ^{20}Na, which they used to deduce limits for the ^{19}Ne$(p,\gamma)^{20}$Na reaction rate with ^{19}Ne in its ground state. Vancraeynest *et al.* [84] performed a re-analysis of this data and published a thorough examination of the data and the ^{19}Ne$(p,\gamma)^{20}$Na reaction rate. They re-analysed the data fully to obtain the resonance strengths of the four lowest resonances, 448, 661, 797 and 887 keV. An upper limit of 21 meV for the resonance strength was measured for the key resonance at 448 keV [84]. This value is inconsistent with the value calculated by Brown *et al.*, implying that a 3^+ spin-parity assignment is not possible. In response to this three of the four authors of Ref. [80] re-examined their previous calculation for the resonance strength [85]. They took into account more recent results for the mirror ^{20}F and recalculated spectroscopic factors to get a limit on the resonance strength for the key resonance of $\omega\gamma$ >16 meV [85], in agreement with the limit found by Vancraeynest *et al.* and Page *et al.* [82, 84].

The last experiment performed with the radioactive ^{19}Ne beam studying the ^{19}Ne$(p,\gamma)^{20}$Na reaction was by Couder *et al.* [86]. An improved set-up was employed for this experiment using the newly built Astrophysics Recoil Separator, ARES, which is used to measure radiative capture reactions in inverse kinematics. The 448 keV resonance was found to have an upper limit of 15 meV at a 90% confidence limit. This is incompatible with the lower limit calculated by Fortune *et al.* [85], although only just.

The exact energy of the resonance is vitality important for direct reaction experiments and as will be discussed in Chapter 5, the resonance energy used in the radioactive beam experiments has since changed by a considerable amount. A third type of experiment which could potentially determine the energy and spin-parity of the first key resonance above the proton emission threshold in ^{20}Na was performed throughout the 1990's.

3.3 β-delayed Proton Decay Studies

Prior to the first direct measurements an extremely selective type of experiment was performed in order to determine the spin-parity of the ∼450 keV resonance. The key resonance was believed to have a spin-parity of either $J^\pi = 1^+$ or 3^+. A β-delayed proton decay study of ^{20}Mg, if sensitive enough, should be able to determine the spin-parity of the key resonance. When ^{20}Mg β-decays from its 0^+ ground state to states in ^{20}Na Gamow-Teller selection rules indicate that states in ^{20}Na with $J^\pi = 0^+$ or 1^+ are much more likely to be populated as no angular momentum needs to be carried away, making the transitions allowed. When populated states in ^{20}Na then proton-decay to ^{19}Ne, protons from states with $J^\pi = 0^+$ or 1^+ are substantially more likely to be detected. Fig. 3.6 shows the decay scheme for the β-delayed proton decay of ^{20}Mg. If a proton is detected at ∼450 keV this will provide confirmation that for the key resonant state $J^\pi = 1^+$, as well as allowing for the energy of the resonance to be measured. However, if no proton is detected at ∼450 keV then an upper limit on the branching ratio and a lower limit on the logft value for the key resonance can be determined. If the lower limit on the logft value is high enough such that no other known logft values for an allowed β-decay in the sd shell are higher, a 1^+ spin-parity assignment can be ruled out and the key resonance can therefore be inferred to have $J^\pi = 3^+$.
The first of such experiments was performed by Kubono *et al.* [88] at RIKEN. A primary beam of ^{24}Mg at 100 MeV/nucleon and a Be target were used to produce ^{20}Mg ions. The ^{20}Mg ions were implanted into the third detector of a 5 silicon detector array (4 x 100 μm and 500 μm), which was surround by three ΔE - E plastic scintillators and two sets of Ge detectors. Whenever a ^{20}Mg ion was detected with the beam monitor, the primary beam was stopped for 200 ms, just over two half-lives. The key resonance was not detected in this study but Kubono *et al.* did put a lower limit on the logft value of 5.42 if the state did have a 1^+

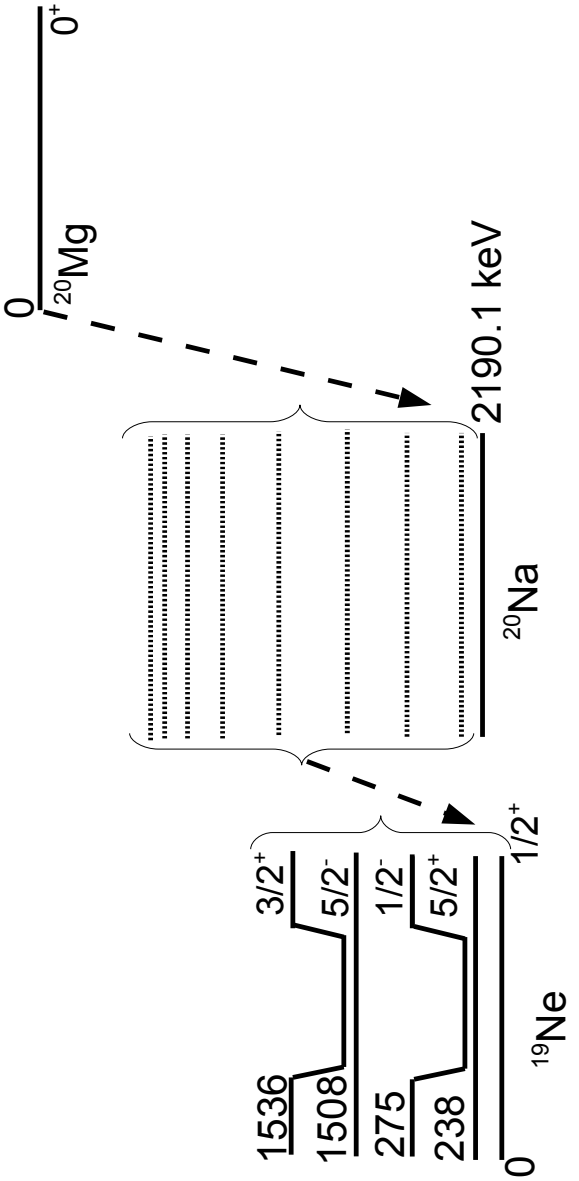

Figure 3.6 *The decay scheme for the β-delayed proton decay of ^{20}Mg. ^{20}Mg β^+-decays primarily to 0^+ and 1^+ states above the proton threshold in ^{20}Na before proton-decaying to states in ^{19}Ne. From Ref. [87] it is known that the proton-decay from states in ^{20}Na populates the ground state and states at 238, 275, 1508 and 1536 keV.*

spin-parity. This limit was not high enough to rule out the possibility of the state having a 1^+ spin-parity assignment. Five other definite proton peaks were detected although no errors were quoted for the energies of these resonances. Fig.

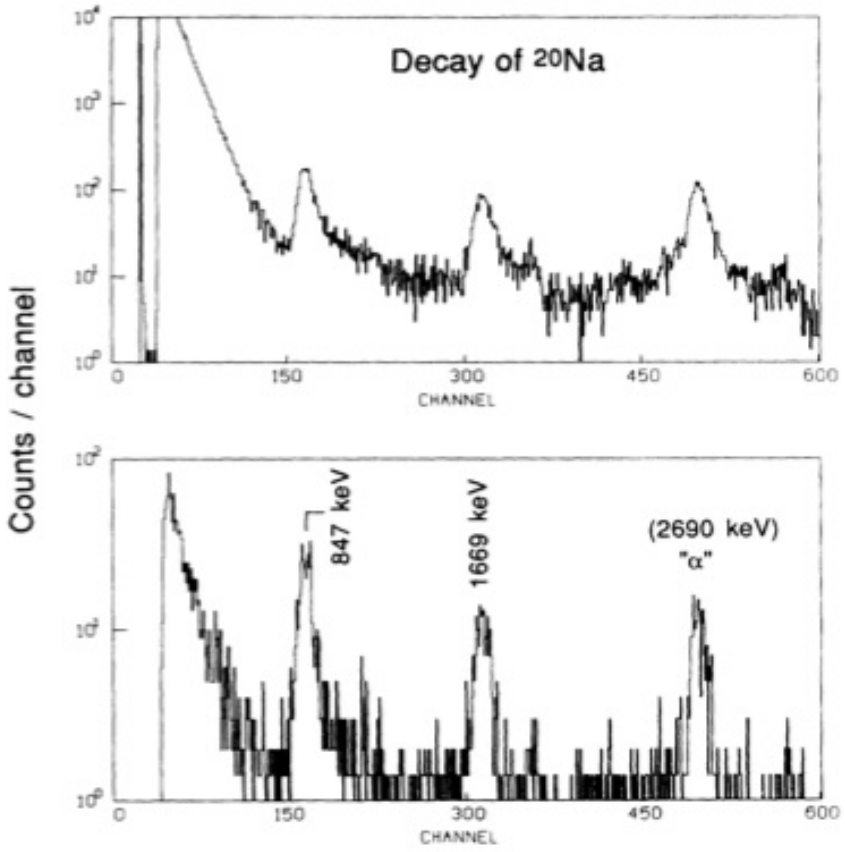

Figure 3.7 *Part of the energy spectrum from the β-delayed proton decay study of ^{20}Mg by Kubono et al. [88]. The top spectrum corresponds to the raw data. The bottom spectrum is the result of coincidences with β-particles detected.*

3.7 shows part of the spectrum gained from this experiment and the reduction in background when a coincidence with β-particles is applied [88].

Another β-delayed proton decay study was performed around the same time by Görres *et al.* [89]. A primary beam of ^{36}Ar was created at the National Superconducting Cyclotron Laboratory at Michigan State University, which bombarded a 250 mg/cm^2 Ni target to create ^{20}Mg ions. Görres *et al.* also used a stack of silicon detectors but with a greater range of thicknesses (500, 50, 100 and 1000 μm). Görres *et al.* took into consideration the background that would occur from β-particles and so implanted the ^{20}Mg beam into the 50 μm silicon detector so that most of the β-particles should escape out of the implantation detector, depositing only a small amount of energy. The energy

calibration came from known proton energies in ^{21}Mg. Again the key resonance was not detected and a lower limit on the logft value of 5.85 was placed, slightly higher than the limit determined by Kubono *et al.* [88] but still not high enough to rule out the possibility of a 1^+ assignment. Four definite proton peaks were detected in this study. Fig. 3.8 shows a section of the spectrum obtained in

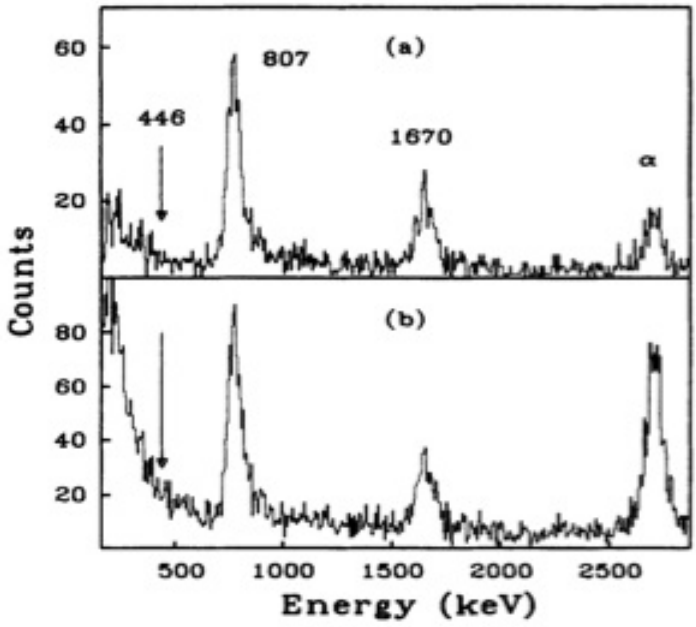

Figure 3.8 *Energy spectrum from the β-delayed proton decay study of ^{20}Mg by Görres et al. [89]. b) shows the ungated spectrum and a) shows the beam off spectrum. The arrow shows the expected position of the key resonance [89].*

this study, highlighting the improvement in the spectrum when data were taken in coincidence with the beam off [89]. The higher logft limit determined in this experiment highlights the improved set-up compared to Ref. [88].

As detector technology improved the β-delayed proton decay of ^{20}Mg was studied again. The improvement in detector technologies enabled β-delayed proton decay studies to be performed with silicon strip detectors, which provide a higher degree of discrimination between signals. Piechaczek *et al.* performed a β-delayed proton decay study at the LISE3 facility, GANIL, where a primary beam of ^{24}Mg at 95 A.MeV bombarded a ^{nat}Ni target in order to produce ^{20}Mg ions through a fragmentation reaction. The ^{20}Mg ions were implanted into a 300 μm silicon strip detector, with 16 segments of 5 x 35 mm^2 each, placed at an angle of 45° to the beam. Two 500 μm large area silicon detectors were placed either side of the 300 μm detector and these were all surrounded by 3 large volume Ge detectors. Fig. 3.9 shows the proton spectrum obtained from this experiment showing all

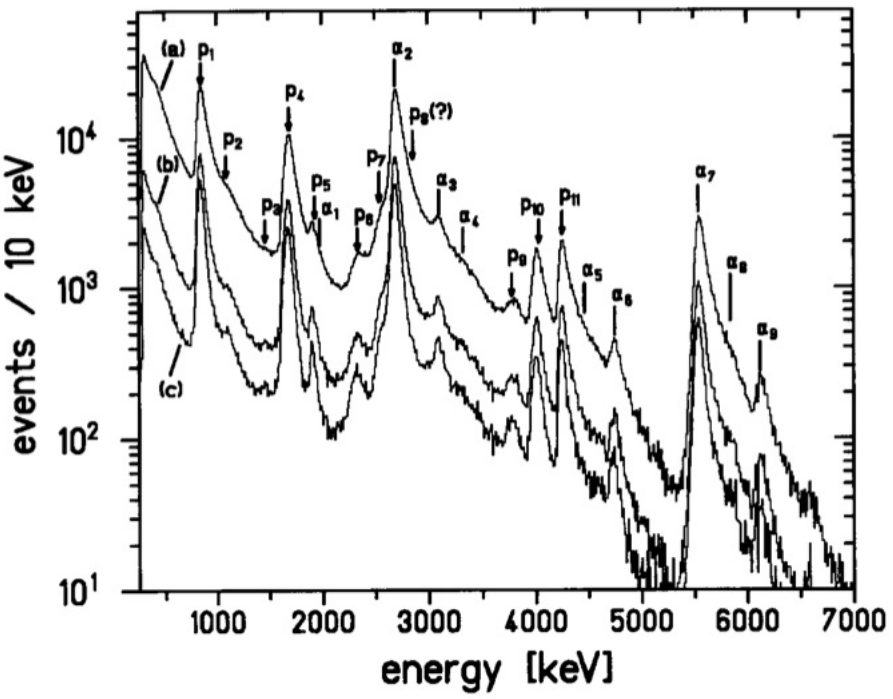

Figure 3.9 *Energy spectrum of the β-delayed proton-decay of ^{20}Mg from Piechaczek et al.. a) Shows the ungated spectrum. b) Shows the spectrum where coincidences are required between the signal in the 300 μm DSSD and a signal in one of the larger detectors in the same area as the original signal. c) Shows the spectrum from any coincidence between a signal in the DSSD and the larger silicon detectors. It is clear from this spectrum the high level of background from β-particles that was present [87].*

11 proton peaks from the β-delayed proton decay of ^{20}Mg detected and α peaks from the β-delayed α decay of ^{20}Na. The calibration for this experiment used a resonance energy for the strongest proton peak, labelled P1 in Fig. 3.9, taken from conference proceedings [90]. However, when the conference proceedings was published the resonance energy had changed by 20 keV due to an incorrect treatment of proton and alpha energy responses in silicon detectors [81]. This therefore made the calibration used in this paper unreliable.

The key resonance was also not detected in this experiment [87]. Piechaczek *et al.* were able to place a more stringent lower limit on the logft value of 6.24 due to increased sensitivity. Although this is a high logft value for an allowed β-decay there are three other allowed β-decays in the sd shell with higher logft values, meaning that a 1^+ spin-parity assignment could not be ruled out [87].

The critical issue as to the spin-parity of the key resonance at $\sim$450 keV above the proton emission threshold in ^{20}Na, despite decades of research, has yet to be confirmed. The next chapter will describe the experiment that took place at Texas A&M University, USA, where new advances in detector technology and secondary beam production were utilised to perform the most sensitive β-delayed proton decay study of ^{20}Mg to date. The lessons learnt from the previous β-delayed proton decay studies were implemented into the new experiment discussed in Chapter 4 and the improved results will be discussed in Chapter 5.

Chapter 4

New Experimental Study of the β-delayed Proton Decay of ^{20}Mg

The current chapter will detail the new β-delayed proton decay study of ^{20}Mg, performed at the Cyclotron Institute at Texas A&M University, USA. This is the most sensitive β-delayed proton decay study of ^{20}Mg to date. The K500 cyclotron at Texas A&M University was used to produce a primary beam of ^{20}Ne, which bombarded a cryogenic ^{3}He target, producing ^{20}Mg through a fusion-evaporation reaction. The ^{20}Mg ions were then filtered out from the other nuclei using the Momentum Achromat Recoil Spectrometer, MARS, before being implanted into a Double-sided Silicon Strip Detector, DSSD, where the beta-delayed protons were measured.

4.1 Methods of Producing ^{20}Mg

Currently, the only way to produce ^{20}Mg is through a secondary beam method or through the ISOL method at TRIUMF. At TRIUMF it is not possible to use a decay spectroscopy station that is needed for a β-delayed proton decay study and as such the secondary beam method was used for the current experiment. Texas A&M University is at the forefront of secondary beam nuclear physics due to its ability to select short-lived isotopes.
Producing ^{20}Mg at a high rate can be difficult as it is a proton-rich nucleus. There are a few different ways of producing proton-rich nuclei. Fragmentation reactions

are type of reaction mechanism useful for producing exotic nuclei, where high energy beams are broken up on a robust target. This type of reaction produces a wide range of nuclei and can produce both neutron-rich and proton-rich nuclei. Fusion-evaporation reactions are another reaction mechanism that can be used to produce proton-rich nuclei and will be described in detail in the next subsection. Both a fragmentation reaction and a fusion-evaporation reaction were trialled before the current experiment was performed. For the fragmentation reaction a primary beam of ^{24}Mg at 48 MeV/u and a ^{9}Be target were used and for the fusion-evaporation reaction a primary beam of ^{20}Ne and a ^{3}He gas target were used. In the production tests it was found that three times more ^{20}Mg was produced at a lower energy through the fusion-evaporation reaction than the fragmentation reaction. It was therefore decided that for the current experiment the reaction mechanism would be fusion-evaporation.

4.1.1 Fusion-Evaporation Reactions

Fusion-evaporation reactions occur when a heavy ion beam fuses briefly with a light ion target, shown in Fig. 4.1. Fusion-evaporation reactions can also occur for light ion beams and heavy targets, however this will not be discussed here. The energy of the beam needs to be high enough to overcome the effective potential barrier and fuse the two ions. Formation of the compound nucleus takes $\sim 10^{-22}$ s and once created the compound will start to either evaporate off nucleons or fission. Whether the compound fissions or not depends on the height of the fission barrier, which in turn depends on the angular momentum and the A and Z of the compound nucleus. The quickest way for the compound to cool is through particle evaporation [91]. For compound nuclei closer to stability, neutron evaporation is more likely to occur because both protons and alpha particles have relatively large Coulomb barriers to overcome. However, if the compound is neutron deficient then the neutron separation energy increases, making charged particle emission competitive with neutron emission. The neutron separation energy can be so great that it is higher than the Coulomb barrier for charged particle emission and therefore charged particle emission is more likely [91]. The evaporated particles have a statistical energy spectrum and each particle that is evaporated takes around 5-8 MeV of energy whilst only removing about 1-2 $\hbar$ of angular momentum. Particle evaporation continues until the particle separation energy is less than the excitation energy of the state above the yrast line. The yrast state corresponds to the lowest energy state for a given angular momentum.

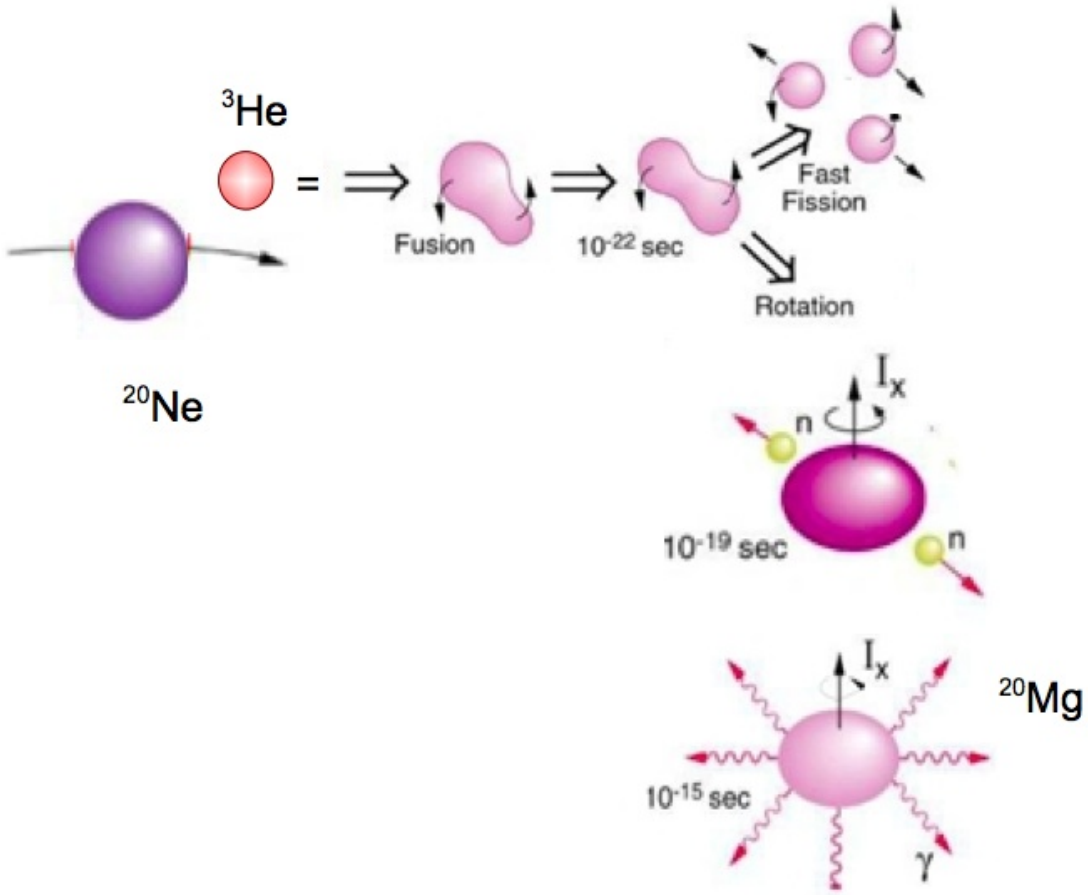

Figure 4.1 *The above figure displays the different stages of the fusion-evaporation reaction for the current experiment. The figure has been adapted from [92].*

For this experiment a beam of ^{20}Ne ions at 25 MeV/u was bombarded onto a ^{3}He gas target. This created an excited compound of ^{23}Mg. This is a neutron deficient nucleus, making charged particle evaporation competitive with neutron evaporation. For the production of ^{20}Mg three neutrons need to be evaporated and therefore the production of ^{20}Mg is suppressed compared to the other evaporation channels.

4.2 Production and Separation of ^{20}Mg

To produce ^{20}Mg through a fusion-evaporation reaction a primary beam from the K500 cyclotron was produced, which then bombarded a ^{3}He gas target. The ^{20}Mg ions then needed to be carefully selected by filtering out contaminant isotopes through MARS. The next section will describe each part of this process.

4.2.1 K500 Cyclotron

The primary ^{20}Ne beam was produced by the K500 Cyclotron at the Cyclotron Institute at Texas A&M University. The stable isotope ^{20}Ne was placed in an Electron Cyclotron Resonance ion source (ECR) where a dense plasma was created. Charged particles were then injected into the K500 cyclotron where they were accelerated to an energy of 25 MeV/u [93]. The ions are held in place in their orbit by a 50 kilogauss magnetic field, generated by 800 Amps of electrical current. This current is carried by 5500 turns of niobium-titanium superconducting wire in a coil, which in turn is surrounded by 100 tons of steel. The acceleration of the ions is achieved by intense rapidly alternating electric fields. The generation, injection, acceleration and delivery of the ions to the target is done in high vacuum, and the path and focus of the beam after the cyclotron is achieved by controlled high-field electromagnets. Once the ^{20}Ne has been accelerated to the required energy it is extracted and sent towards the gas target at the front of MARS. Fig. 4.2 shows the layout of the K500 cyclotron and the possible paths the accelerated ions can take.

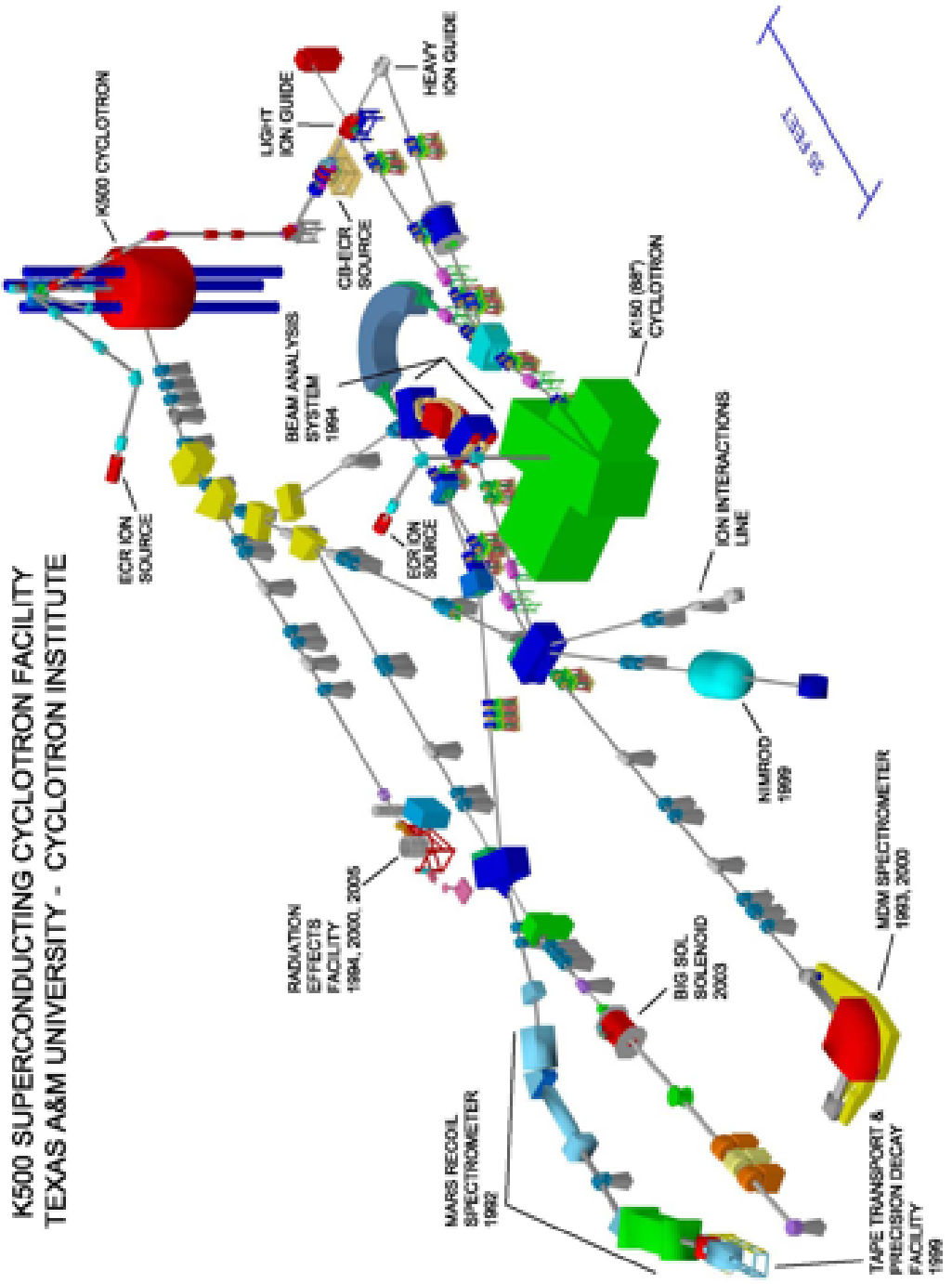

Figure 4.2 *K500 cyclotron and possible paths for the accelerated isotope [93]. The diagram also shows the K150 cyclotron, which is part of a current upgrade project at Texas A&M University.*

4.2.2 Target

The target used was a light ion target of ^{3}He which was contained within a gas cell. The cell used was 10 cm long with Havar windows 19.05 mm in diameter with an average thickness of 4.064 μm. Havar was used for the windows due to its immense strength even when used as a very thin film. Havar also has a similar thermal expansion coefficient to that of steel, of which the body and flanges of the cell were made, making the windows less likely to tear when the gas is cooled. The gas cell was cooled so that the density of the gas increased, thereby effectively increasing the thickness of the target. The pressure of the gas remained roughly steady at 2 atm. The gas becomes heated as it interacts with the ^{20}Ne beam, producing a cylinder of heated gas along the path of the beam reducing the density of the gas and effectively reducing the density of the target along the beam path. To counteract this a magnetic stirrer is used within the gas cell in order to mix the heated and cooler gases to avoid a drop in density along the path of the beam [94].

4.2.3 MARS

The fusion of the ^{20}Ne beam with the ^{3}He gas target creates many different isotopes and these need to be separated from the ^{20}Mg ions before the ^{20}Mg ions are implanted into the DSSD. For this experiment MARS was used. MARS is a series of dipoles, quadrupoles and slits, a velocity filter and a beam dump. MARS can be split into two sections, before and after the velocity filter, as can be seen in Fig. 4.3. Before the velocity filter the quadrupole magnets Q1, Q2 and Q3, with the two dipoles D1 and D2, provide a nearly parallel, achromatic transport of the beam into the velocity filter. After the velocity filter the quadrupoles Q4 and Q5, with the dipole D3, produce a M/Q mass focus at the focal plane of MARS.

When the beam first leaves the gas target it goes through the first slit, SL1, which adjusts the angular acceptance of the beam. Quadrupoles Q1 and Q2 then focus the beam before it goes into the first dipole. The first dipole, D1, gives p/q dispersion in the horizontal direction, providing mass dispersion as the beam enters the beam dump or "coffin". In the beam dump the primary beam is stopped in a Faraday cup and the intensity of the beam is monitored. A slit at

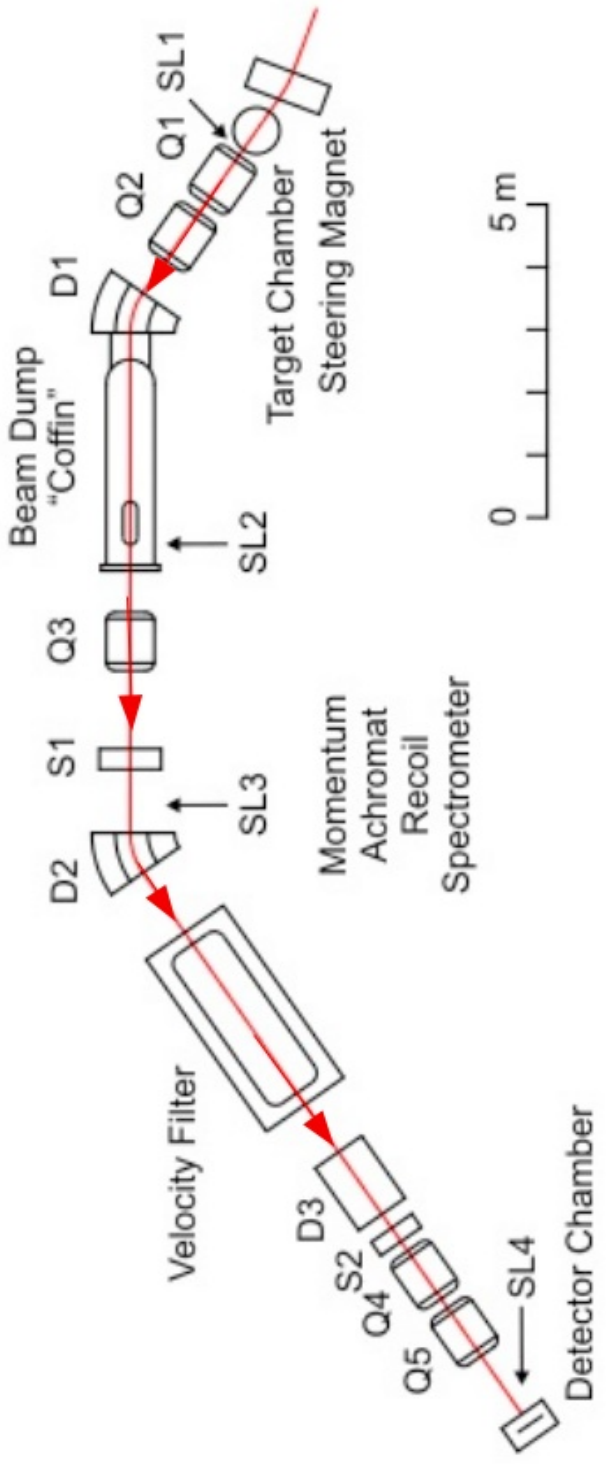

Figure 4.3 *The layout of MARS [95]. The red arrow shows the direction of the ions through MARS.*

the end of the beam dump, SL2, is used to further remove contaminants from the beam and provide horizontal momentum selection. The beam then goes through the third quadrupole Q3 and the third slit SL3, which limits the vertical extent of the recoil ions. Q3, SL3 and D2 ensure that the beam is almost parallel to the velocity filter before the beam enters it [95].

The velocity filter is 3 m long, with a gap of 10 cm between 2 high voltage plates. The electric field between the plates is 50 kV/cm, with a maximum magnetic field of 1 T. Once the beam comes out of the velocity filter it is bent upwards by the third and final dipole D3, in order to match the momentum dispersion to the velocity dispersion. The beam then heads into the last two quadrupoles, Q4 and Q5, which focus the beam in both the vertical and horizontal planes. The final slits, SL4 and SL5, are then used to define the solid angle of the secondary beam and the acceptance value of M/Q, before the beam enters the implantation chamber [95].

The optics of the MARS system allows discrimination of nuclei even when the particles have similar p/q. MARS also has a small transit time from the target chamber to the detector chamber allowing the study of nuclei with very short half-lives. The target area can be adjusted depending on the experiment being performed as the target location can be moved toward Q1, increasing the geometrical solid angle and first order magnification in the mass dispersion plane. For the velocity filter, as the energy of the beam increases, the maximum dispersion of the different components is limited by the E-field, while for lower energies the system is limited by the B-field. The dispersion of the whole system is also limited by the bend in D3. When the angle of D3 increases beam crossover starts to occur, which results in a very large first order magnification in the mass dispersion plane. The maximum mass dispersion starts to flatten out at $\sim$8 MeV/U, which can be corrected in one of two ways, either by lowering the E and B fields in the velocity filter or by readjusting the D3 bend angle. The resolution of the beam depends on three things; the solid angle, momentum acceptance and mass dispersion. Optimisation of all three of these improves the resolution of the beam.

MARS must be configured in order to filter out unwanted isotopes, leaving ideally only the isotope required for the experiment. There are two detectors within MARS, labelled S1 and S2 in Fig. 4.3, and a further detector within the implantation chamber used to monitor the composition of the beam. Fig. 4.4 is a plot of the final composition of the beam. The final analysed beam contained $\sim$89% ^{10}C ions, $\sim$10% ^{20}Mg ions and $\sim$0.5% ^{17}Ne ions, all fully stripped. The

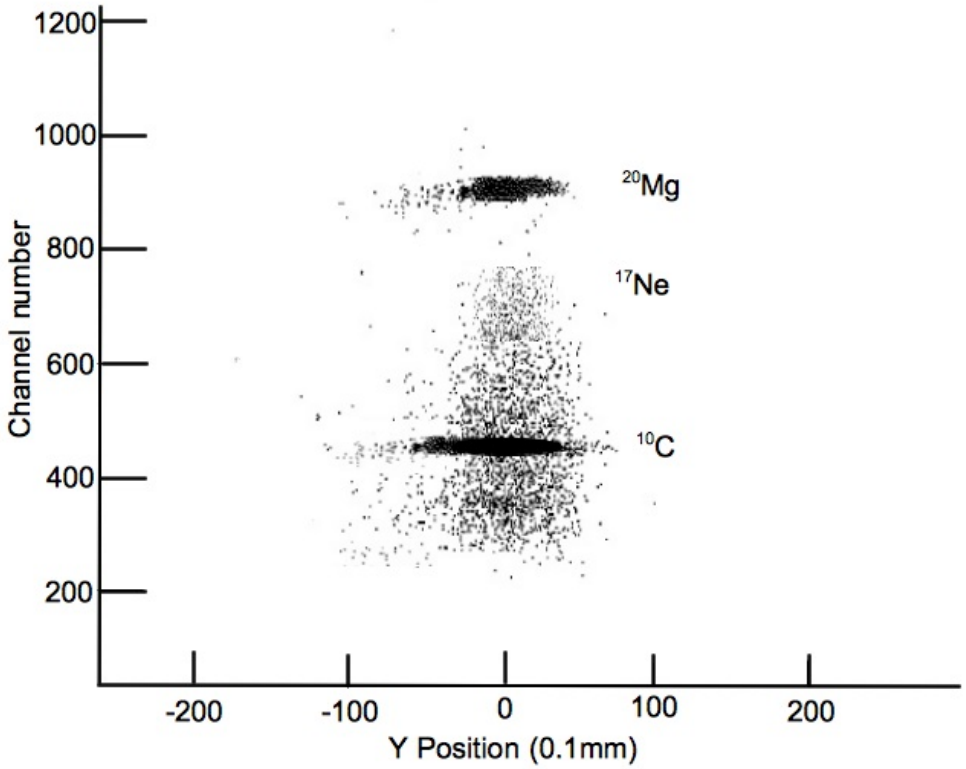

Figure 4.4 *The final composition of the beam, with ∼89% ^{10}C ions, ∼10% ^{20}Mg ions and ∼0.5% ^{17}Ne ions, all fully stripped. .*

^{10}C and ^{17}Ne ions went straight through the main detector into which the ^{20}Mg ions were implanted and were stopped inside the 1 mm thick silicon detector.

4.3 Detectors and the Implantation Chamber

The choice of detector and the set-up of the detectors held the key to the success of the present experiment. The next few sections will detail the reasons behind the choice of the main detector and the set-up of the detectors.

4.3.1 GEANT4 Simulations

There were two different thicknesses of detector available for the main detector, 45 and 100 μm. A GEANT4 simulation was performed to help decide which of these two detectors would be best suited for the experiment. This involved simulating the β-delayed proton decay of ^{20}Mg in both the 45 μm and 100 μm DSSDs and changing the spread of the beam within the detector. By studying the different simulations for the two thicknesses of detector the background from the β-particles and protons around the energy region of interest, $\sim$450 keV, could be studied. β-particles have a range typically of a few mm in silicon and as such most should escape out of the two detectors. However, β-particles are not likely to go straight out of the detector and instead are more likely to cross a few strips before leaving the detector. Protons of energy $\sim$450 keV have a range in silicon of $\sim$7 μm and will therefore most likely not escape out of the detector. However, higher energy protons have a longer range in silicon and can escape out of the detector, depositing a small amount of energy within the detector.
From comparing the simulations for the two detectors it became clear that the level of background from β-particles within the 100 μm detector was too high for the sensitivity that was required in the present experiment. The background from β-particles was substantially less in the 45 μm detector as was expected, although there was now a relatively high background around the region of interest from higher energy protons escaping. The level of background from the escaped protons in the 45 μm detector was less than the level of background from β-particles in the 100 μm detector and as such the 45 μm detector was chosen. The spread of the beam was varied so that the background at different widths of beam could also be investigated. By changing the spread of the beam the maximum

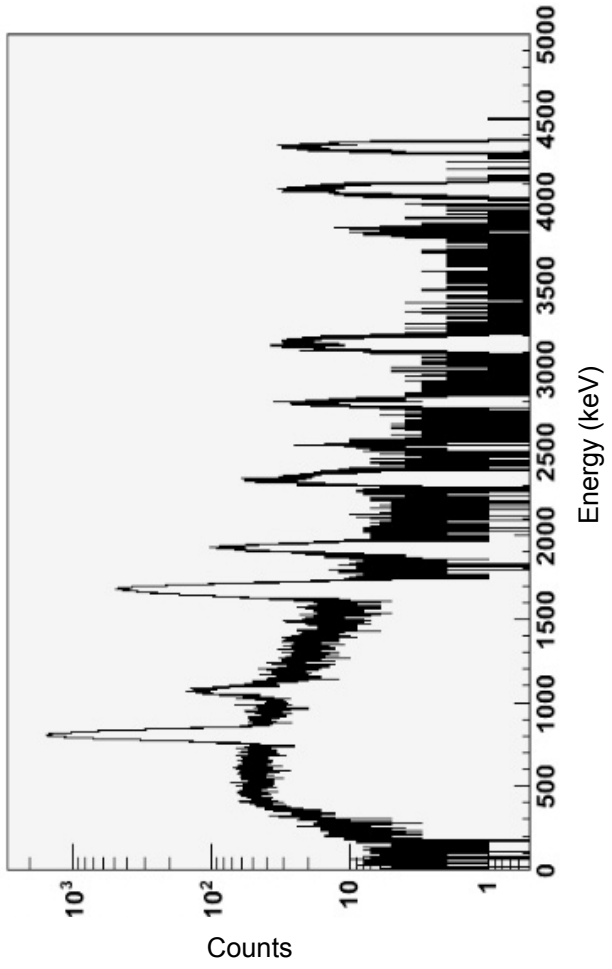

Figure 4.5 *Spectrum gained from a GEANT4 simulation using a 45 µm double sided silicon detector. The GEANT4 simulations were used to help decide the thickness of detector to be used and to give more information about the loss of high-energy protons out of the detector.*

expected percentage loss of counts due to high-energy protons escaping the DSSD could be determined. Fig. 4.5 shows the simulated proton-decay spectrum using a 45 μm detector.
From the GEANT4 simulations it was found that for protons with energies over $\sim$1 MeV the loss of expected counts became substantial due to the protons escaping out of the detector. It will therefore not be possible to gain any information on the branching ratios for resonances over 1 MeV. It is expected that for escaping protons the smaller the amount of energy deposited in the thin DSSD the greater the amount of energy deposited in either of the two thicker silicon detectors. This will be useful when completing the analysis of the proton spectrum.

4.3.2 Detector Set-up and Data Acquisition

In the present experiment three separate silicon detectors were used. The main detector, a 45 μm DSSD into which the ^{20}Mg ions were implanted discussed in the previous section, was segmented into 24 horizontal strips and 24 vertical strips of 1 mm pitch. The high segmentation of the detector and the small thickness minimised the sensitivity to positrons, which have a much greater range in silicon, $\sim$mm, compared to the $\sim$450 keV protons, $\sim$7 μm, emitted from the main resonance of interest. Fig. 4.6 shows a photo of the 45 μm DSSD on the stand used in the experiment. To detect the high energy protons and β-particles escaping the DSSD two thicker silicon detectors, 140 μm and 1 mm, sandwiched the DSSD. These two detectors were not segmented.
Fig. 4.7 shows the set-up within the implantation chamber including the ΔE-E detector telescope mentioned in Section 4.2.3 and used in the tuning of the beam. This detector was moved away once the beam was tuned and the beam passed further into the implantation chamber where Al degrader foils with an angular resolution of 0.1° were used to implant the beam into the centre of the main detector, the 45 μm DSSD. All three silicon detectors were used as a ΔE-E telescope in order to control the implantation of the beam into the DSSD. The beam was implanted into the centre of the DSSD. The detectors were placed on a wedge at a 45^o angle to the beam to increase the relative thickness of the detectors to the beam. This helped with the implantation of the beam. For the beam to be neatly implanted into the centre of the thin DSSD used in this experiment the beam needed to be of low energy with very little straggling.
The electronics set-up for the experiment is shown in Fig. 4.8. The beam was

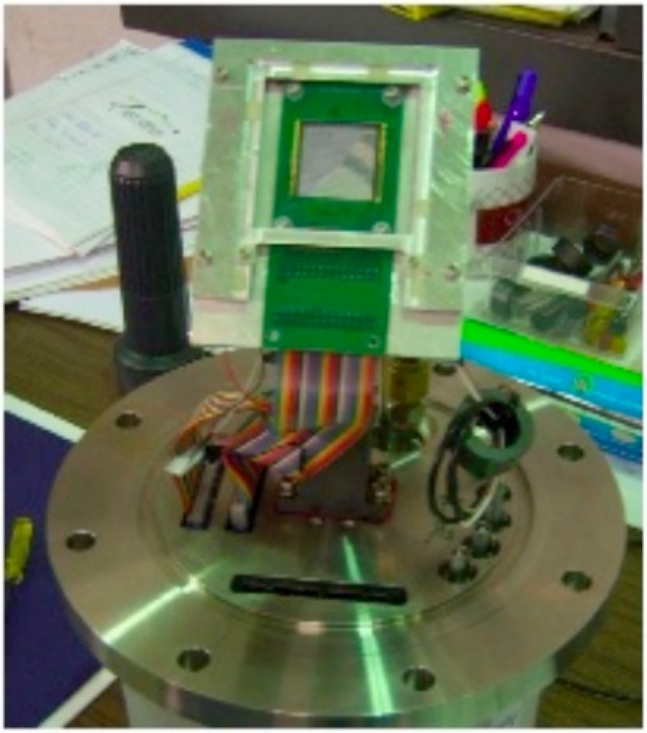

Figure 4.6 *A picture of the 45 μm detector on the 45° stand.*

pulsed to limit beam induced background. For data to be recorded two triggers were required. The first was a timing trigger ensuring data was only collected when the beam was off. The second trigger was an energy trigger from the main DSSD. When the main DSSD measured an energy signal on one side of the detector, which coincided with the timing signal indicating that the beam was off, all three detectors recorded data. A low energy cut-off was applied to all three detectors of 300 keV below which the detector set-up was highly sensitive to electrical noise. With this set-up a total of $\sim 3 \times 10^6$ ^{20}Mg ions over a period of $\sim$2.5 days were implanted into the DSSD. Chapter 5 will detail the analysis of the data collected.

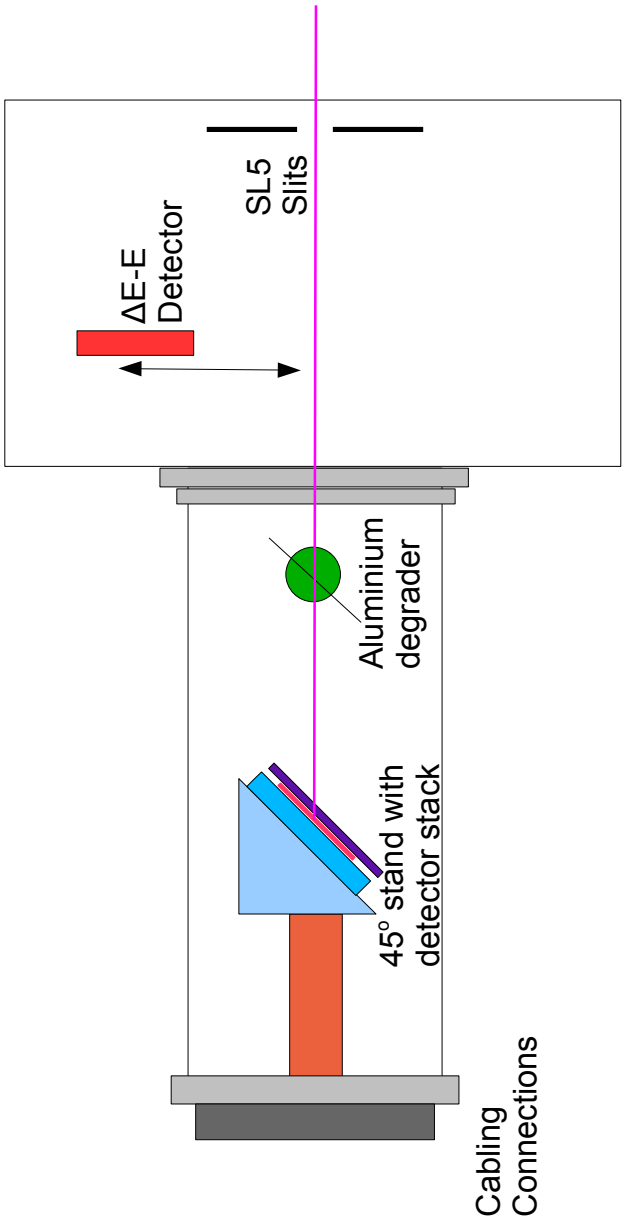

Figure 4.7 *Implantation station for the present experiment.*

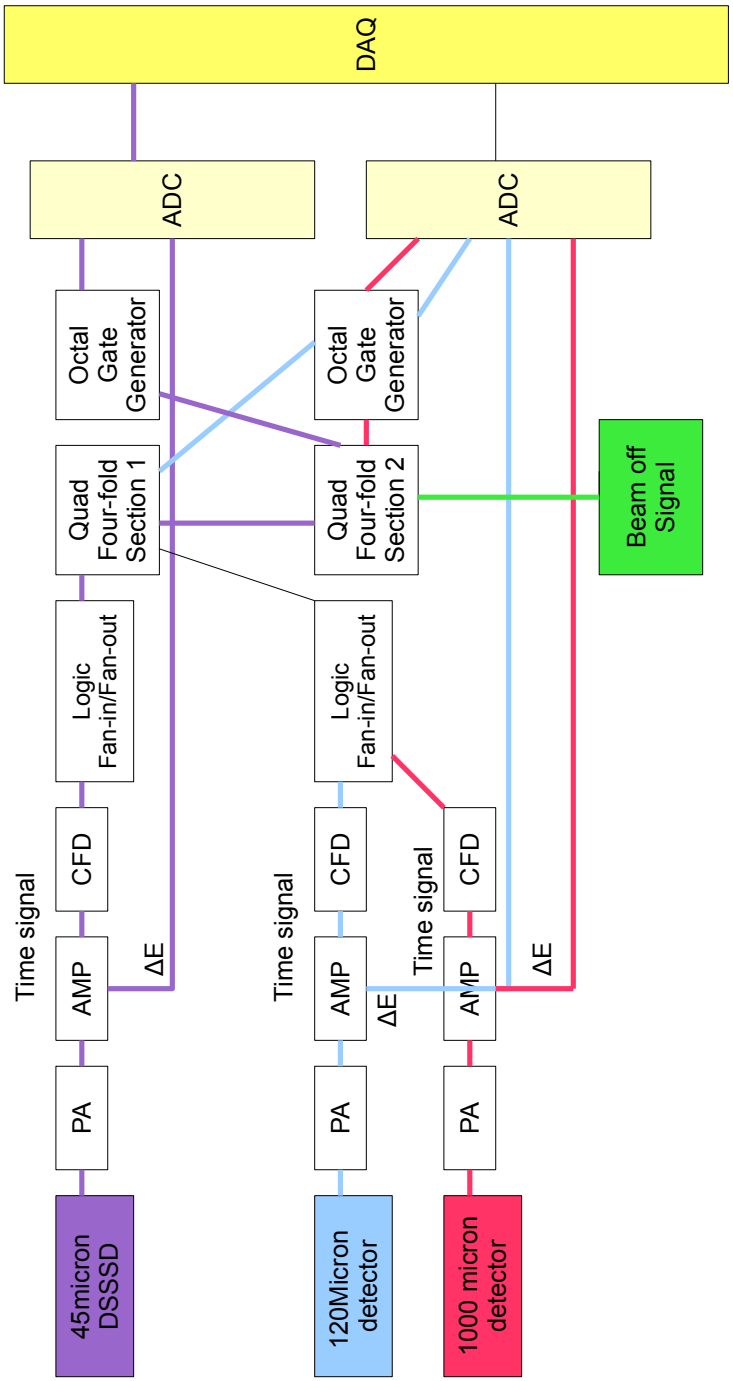

Figure 4.8 *A schematic diagram of the electronics set-up for the current experiment.*

Chapter 5

^{20}Na Analysis and the ^{19}Ne$(p,\gamma)^{20}$Na Reaction rate

Following the β-delayed proton decay study of ^{20}Mg a vast amount of data was obtained requiring a detailed analysis in order to determine energies and spin-parities for states observed, in particular the key resonance at ∼450 keV. This chapter will detail the different stages of the analysis process and the consequences for the ^{19}Ne$(p,\gamma)^{20}$Na reaction rate at astrophysical temperatures.

5.1 Preliminary Analysis of the Proton Spectrum

5.1.1 Calibration of Silicon Detectors

To determine whether or not the key resonance at ∼450 keV had been detected an accurate calibration of the DSSD was required. An initial calibration using strong α-lines from ^{148}Gd and ^{228}Th sources was used to look at the data online. However, due to the different energy responses of α-particles compared to protons an internal calibration for the DSSD was necessary. For the internal calibration well-known resonance energies from previous experiments were used. The strongest proton peak in the spectrum, the 797(2) keV peak, is known accurately from a measurement of the (p,p) scattering of ^{19}Ne [81] and was used as the main point in the current calibration. Higher lying lines were also needed to establish an energy dispersion in order to complete the calibration. These

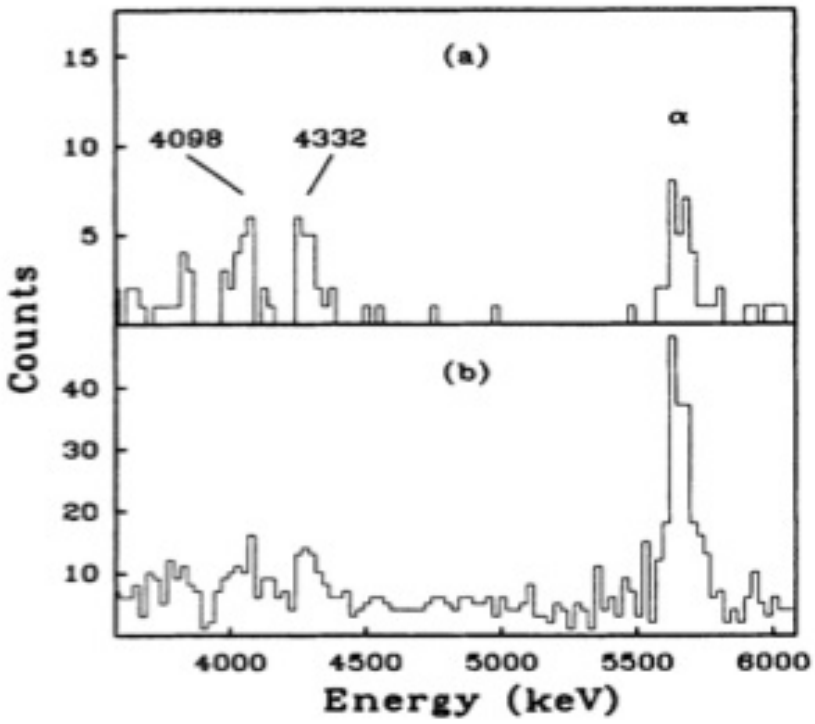

Figure 5.1 *Energy spectrum from the β-delayed proton decay study of ^{20}Mg by Görres et al. [89] showing the 4432 keV proton peak. b) shows the ungated spectrum and a) shows the beam off spectrum [89].*

extra lines came from the β-delayed proton decay study of ^{20}Mg by Görres *et al.* [89], as mentioned in Chapter 3, spectra from which are shown in Fig. 3.8 and Fig. 5.1.

The 1670(10) keV proton peak is a combination of three proton peaks from three separate proton decays [87] but in Ref. [89] the individual proton peaks were indistinguishable and only one Gaussian function was fitted to the peak. For the calibration in the present experiment, although at least two of the three proton peaks could be distinguished, only one Gaussian function was fitted to the 1670 keV peak. This did not however introduce any errors into the calibration. Görres *et al.* [89] calibrated with respect to precise, well-known, β-delayed proton decay lines from ^{21}Mg [96]. A thin silicon detector was used in Ref. [89], much like this experiment, and as such in Ref. [89] and here β-summing effects were neglected. No internal calibration was available for the two thicker silicon detectors so the final calibration for these detectors was based on the strong α-lines from the ^{148}Gd and ^{228}Th sources. This did not introduce any errors as an exact calibration was not needed for these detectors.

There was a high level of electrical background at very low energies in the DSSD requiring some basic analytical techniques to reduce this before more advanced analysis could occur. An equal energy cut was applied to the data, which required that the energy measured on one side of the detector be within $\pm$40 keV of the energy measured for the same event on the other side. As protons at the energies detected were mostly short-ranged, the counts cut by the equal energy requirement were mostly signals from β-particles, escaping protons and general electrical noise. As well as reducing the high level of background at very low energies the equal energy cut also gave a good check of the energy calibration of the DSSD, as most of the signals were within $\pm$40 keV of each other. Fig. 5.2 shows the difference in energy between signals measured on the front and back of the DSSD. A range of $\pm$40 keV was used based on the full width at half-maximum of the proton peaks in the spectrum. About 25% of the total counts were cut using the equal energy requirement.

High multiplicity events were also cut. As the protons of interest do not have a long range in silicon, for each event only one strip is expected to fire on each side of the DSSD. It is possible for more than one strip to fire either due to β-particles and escaping protons travelling across more than one strip creating inter-strip signals or due to random electrical noise causing numerous numbers of strips to fire at once. The multiplicity one requirement reduced all three types of background, producing Fig. 5.3, cutting out a $\sim$1/3 of the counts. Comparing

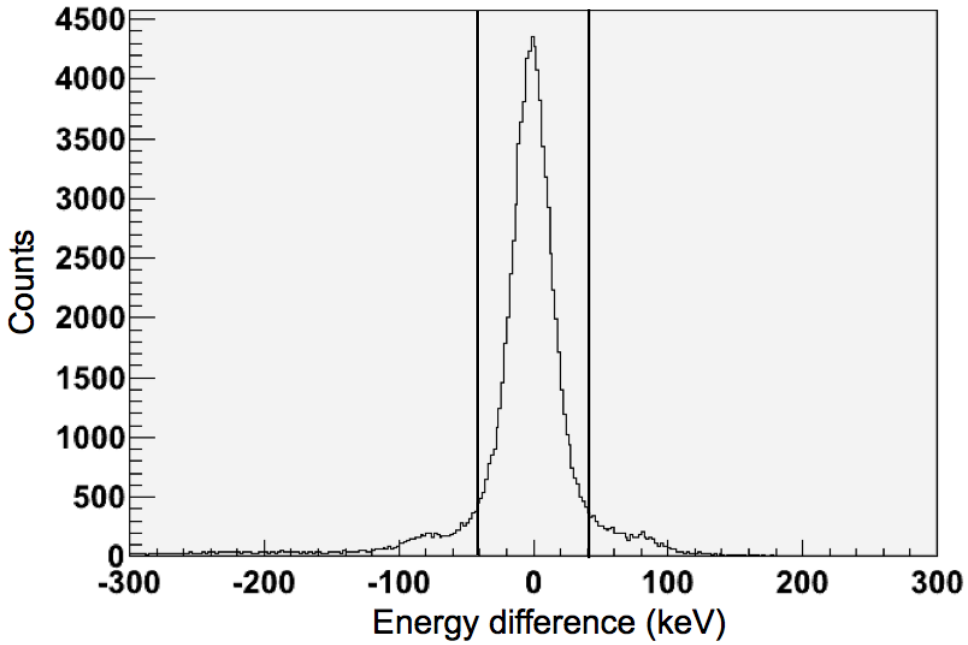

Figure 5.2 *Energy difference plot showing the difference between signals recorded on the front and back of the DSSD. Most energy signals were equal to one another within 40 keV.*

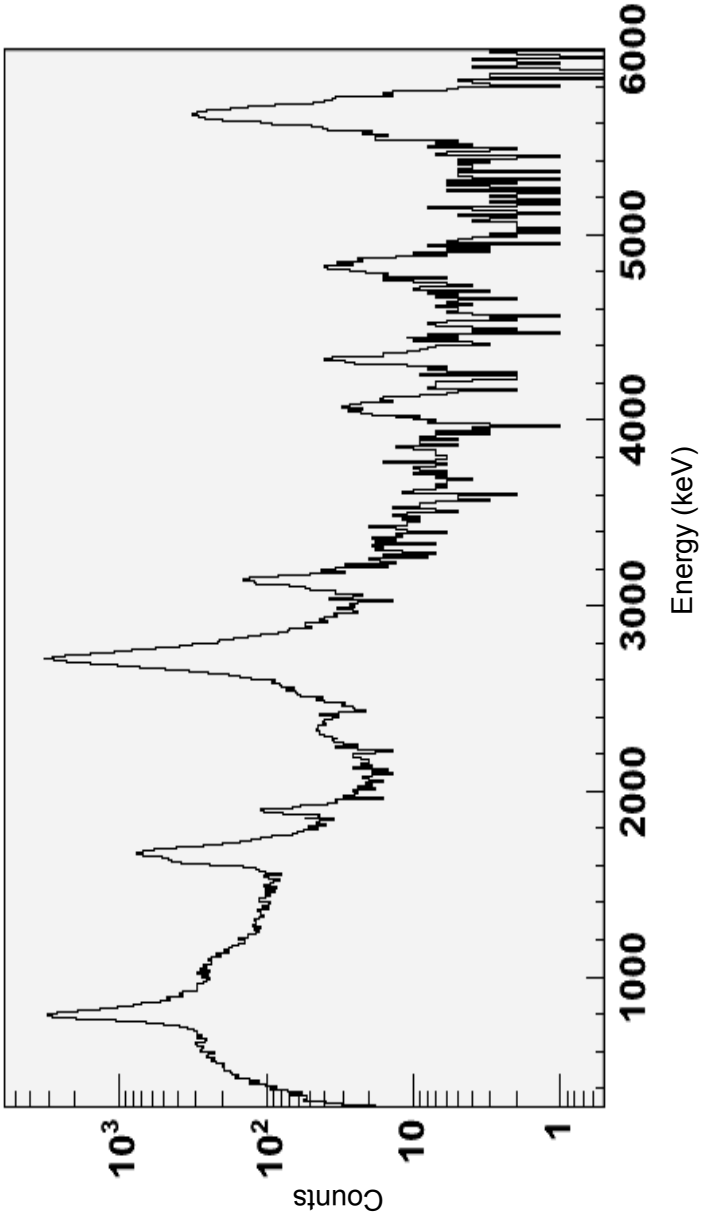

Figure 5.3 *Proton spectrum after equal energy and multiplicity one conditions have been applied. There is already a noticeable improvement in the proton spectrum compared to Fig. 3.9, the proton spectrum from Ref. [87].*

this proton spectrum to Fig. 3.9, the proton spectrum from Ref. [87], it is clear that there has already been a large reduction in background from β-particles from the basic analytical techniques used and the vastly improved experimental set-up. This is most noticeable in the reduction in the β-tails on the right of the proton peaks, visible in Fig. 3.9 but not in Fig. 5.3.

5.1.2 Exploring Coincidences Between all Detectors

Although Fig. 5.3 is a clean proton spectrum with the background from β-particles significantly lower than previous β-delayed proton decay studies of ^{20}Mg [87–89], the background at low energies due to escaped protons is still quite high. Protons escaping the DSSD was a known source of background and was discussed in Section 4.3.1. In exploring the coincidences between the silicon detectors the aim was to specifically reduce the background around the region of interest, $\sim$450 keV, whilst keeping as many counts in the other proton peaks as possible. It was also essential to keep in mind that for every event a β-particle would always be produced.

The coincidences between the DSSD and the two thick silicon detectors were firstly investigated by plotting signals from the DSSD against the signals from the thicker silicon detectors, an example of which is shown in Fig. 5.4. The strong proton and alpha lines are characterised by horizontal lines where a proton or alpha in the DSSD is in coincidence with mostly β-particles. The greater the energy of the proton as it escapes the DSSD the smaller the amount of energy the proton deposits in the DSSD and the greater the energy the proton deposits in either thick silicon detector. This behaviour was expected to be seen in Fig. 5.4 as diagonal lines from the strong proton and alpha lines, showing a correlation between low energy background noise in the DSSD and high energy signals in the thick silicon detectors. This is difficult to see in Fig. 5.4 especially at low energies in the DSSD, above $\sim$700 keV in the 1 mm silicon detector, where it is impossible to distinguish between signals from escaped protons and β-particles.

As the escaping protons could not be clearly identified at low energies a different approach was taken in order to understand the coincidences between the thicker silicon detectors and the DSSD. An energy gate on the thick silicon detectors was placed and the coincidence proton spectrum produced was investigated. By changing the gate so that the coincidence proton spectrum for all energies in either thick silicon detector were investigated a correlation between the energy

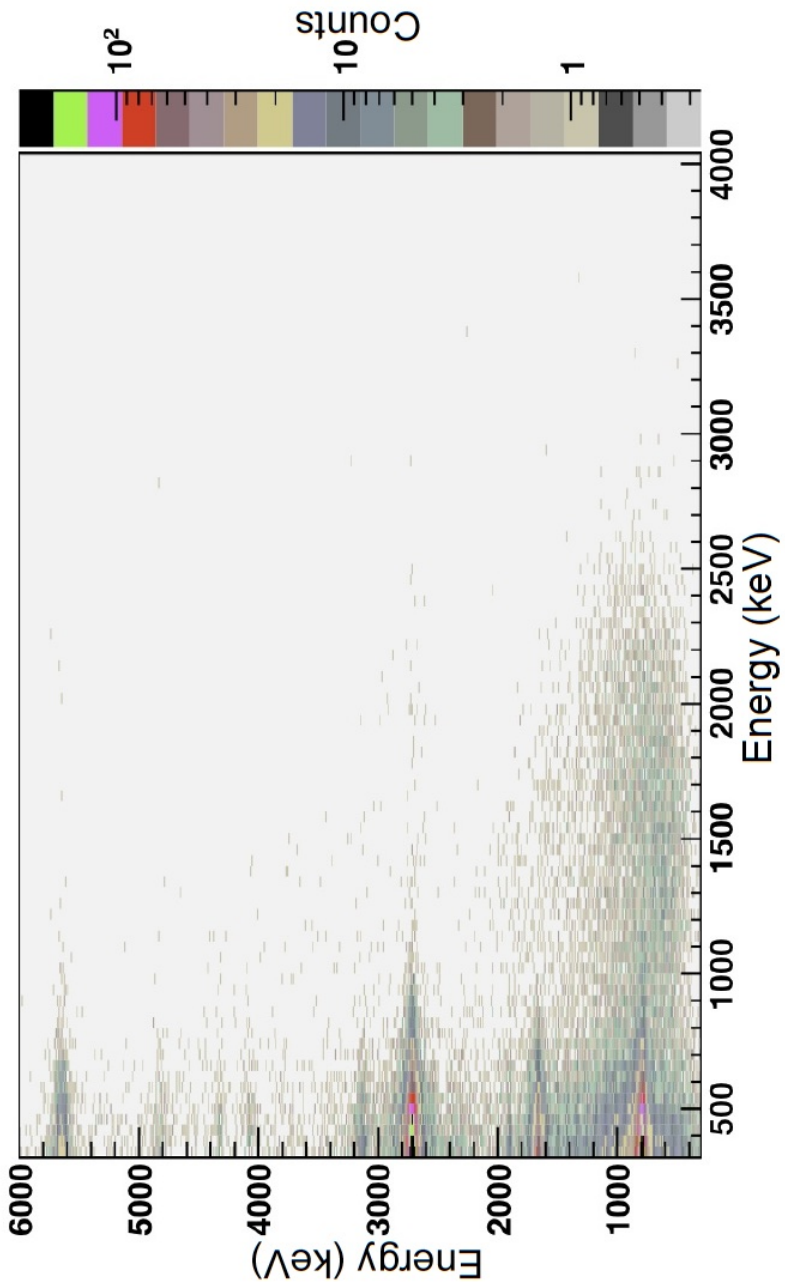

Figure 5.4 *Coincidences between signals in the 1 mm silicon detector and signals in the DSSD. See text for details.*

of signals in the thick silicon detectors and the background around the region of interest in the DSSD was found. It was clear that above ∼1 MeV in the thick silicon detectors the spectrum was dominated by escaped protons. Fig. 5.5 shows the reduction in counts for coincidences below 1 MeV for both thick silicon detectors. When both vetoes are combined the effect is increased. It is clear from these spectra that the energy cut-off is cutting out background around the region of interest whilst retaining the majority of the counts in the proton peaks. Under 10% of the overall counts are lost.

5.1.3 Background Subtracted Proton Spectrum

The final proton spectrum is shown in Fig. 5.6. The original proton spectrum from Fig. 5.3 is shown on top of the final proton spectrum to show the significant reduction in the background around the region of interest whilst the counts in the proton and alpha peaks remain nearly untouched. The different proton peaks and their energies are shown in the spectrum and the α peaks are also labelled.

5.2 Key Resonance in ^{20}Na at ∼450 keV

With the great reduction in the background around the region of interest the key resonance needed to be fully investigated. The next few sections will detail the analysis of the key resonance and the implications of this analysis on the $^{19}\mathrm{Ne}(p,\gamma)^{20}\mathrm{Na}$ reaction rate.

5.2.1 Energy of the Key Resonance

From studying the proton spectrum in Fig. 5.6 it is clear that no proton at ∼450 keV has been detected. Therefore an upper limit on the proton decay branch in order to calculate a lower limit on the logft value needed to be calculated, which required the exact energy of the key resonance. The key resonance was known to be around ∼450 keV but its precise location had yet to be determined. The most recent β-delayed proton decay study, Ref. [87], used a value of 450 keV for the key resonance, corresponding to an excitation energy of 2645 keV. The location of the key resonance is vitality important when working out the limit on the branching ratio as the limit depends on the level of background at the energy

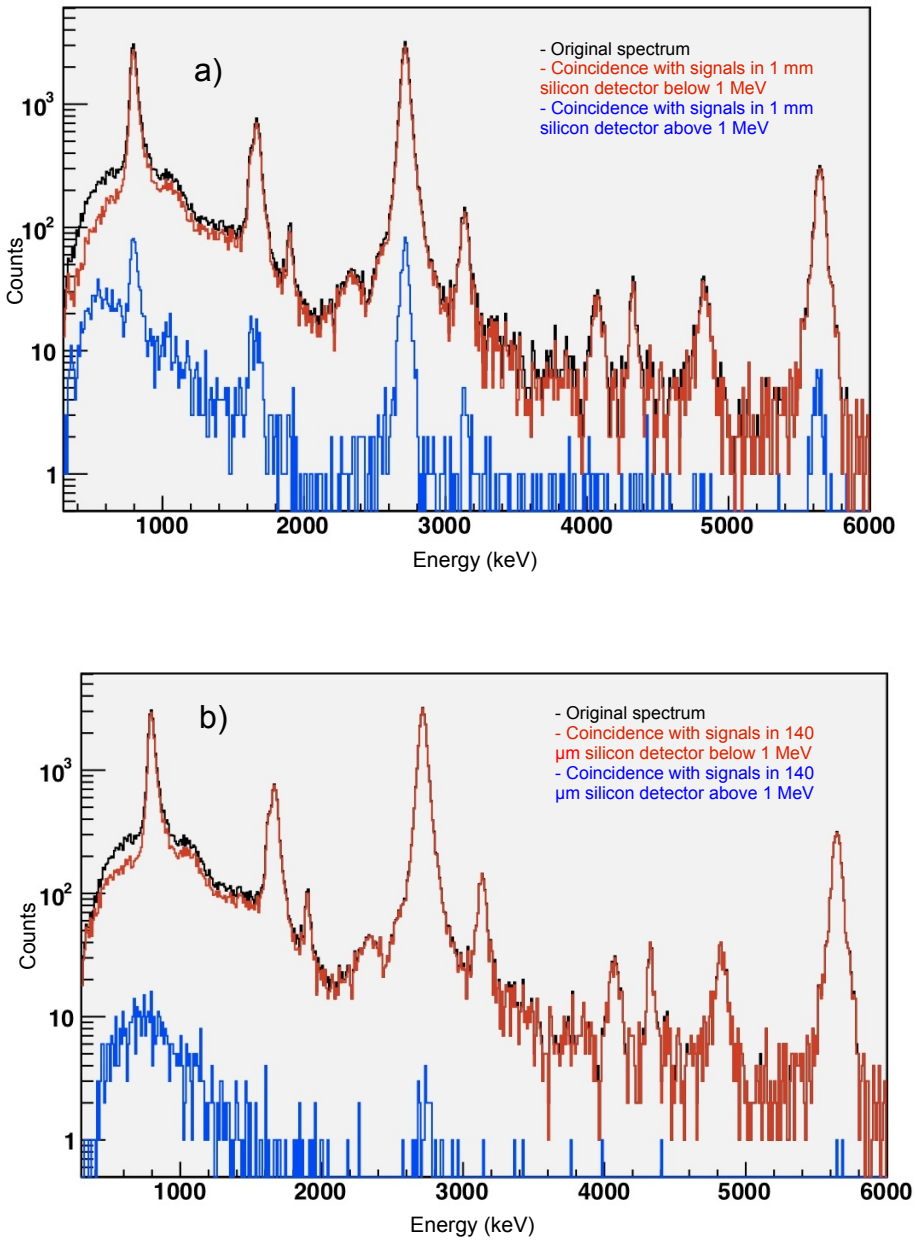

Figure 5.5 *a) The proton spectrum produced in coincidence with signals in the 1 mm detector below 1 MeV and above 1 MeV compared to the original proton spectrum as shown in Fig. 5.3. b) The proton spectrum produced in coincidence with signals in the 140 µm detector below 1 MeV and above 1 MeV compared to the original proton spectrum as shown in Fig. 5.3.*

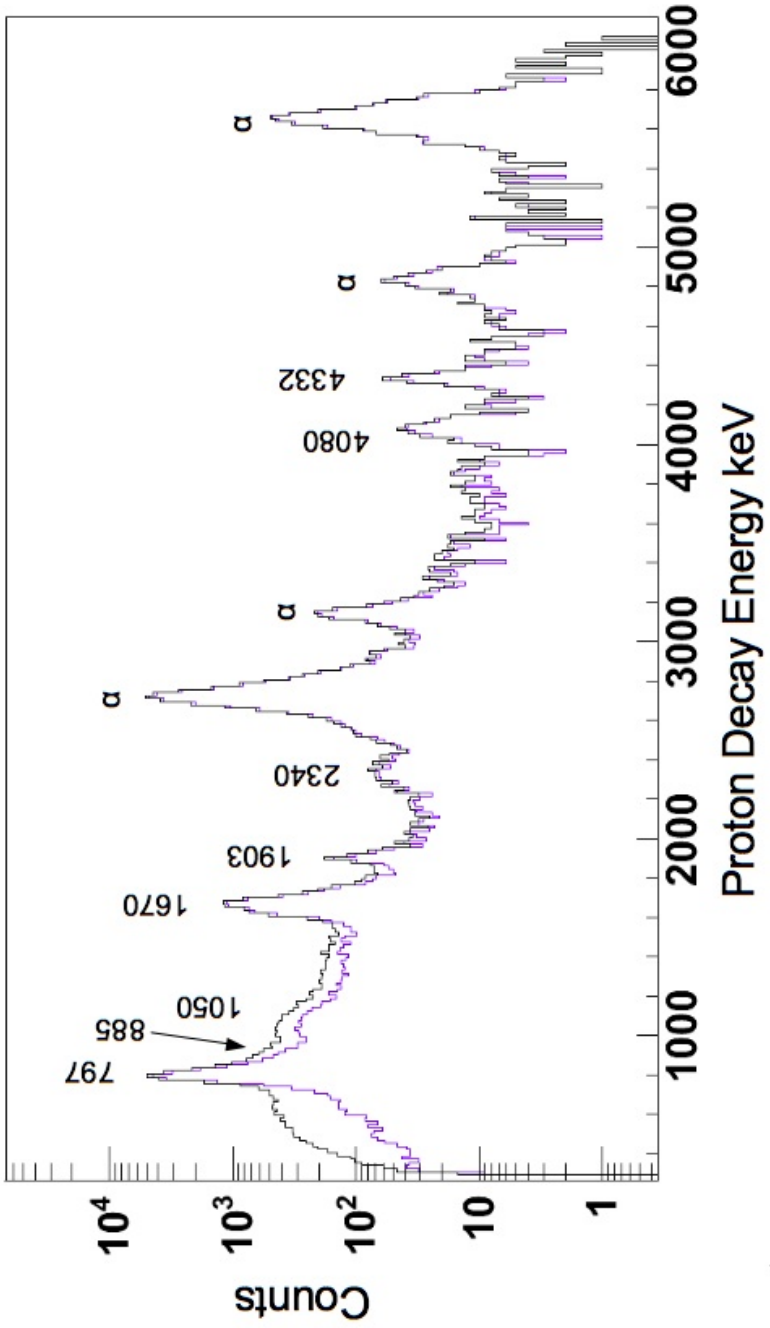

Figure 5.6 *The black proton spectrum corresponds to the raw data. The purple proton spectrum shows the final spectrum, where anti-coincidences with both the 140 μm and 1 mm silicon detectors above the energy threshold of ∼1 MeV were implemented.*

of the key resonance. From a careful study of previous experiments the exact location of the key resonance has been derived.
The accurately measured resonance at 797(2) keV that was used previously in the calibration of the DSSD will also be used here and will be combined with work from another study. The high resolution study of the ^{20}Ne(^{3}He,t)^{20}Na reaction using a magnetic spectrograph, performed by Smith *et al.* [77], gave an accurate value of 340(2) keV for the energy difference between the key astrophysical resonance in ^{20}Na and the 2986(9) keV state, the 797(2) keV resonance. By combining the energy difference of 340(2) keV with the 797(2) keV resonance a value of 457(3) keV is found for the key resonance, corresponding to an excitation energy of 2647(3) keV.

5.2.2 Limit on the Logft Value for the 457 keV Resonance

Using the new, accurate value for the energy of the key resonance of 457(3) keV, the limit on the proton decay branch and a limit on the logft value could be calculated. Firstly the background around the region of interest needed to be understood and this was achieved by fitting a 4th order polynomial to the background, once over the whole of the region and once not including the region where the key resonance was expected. It was found that there was no discernible difference between the two fits. Fig. 5.7 shows the region of interest with the 4th order polynomial fitted to the background. The number of counts in the background was then compared to the number of counts in the 797(2) keV peak, which from the GEANT4 simulations discussed in Section 4.3.1, was known not to suffer significant losses due to protons escaping. By comparing the two a higher limit on the proton decay branch of 0.02% at a 90% confidence level was found, corresponding to a lower limit on the logft value of 6.9.
The most recent limit determined by Piechaczek *et al.* of 6.24 [87], although high for an allowed β-decay, was not high enough to rule out the possibility of a 1^+ spin-parity assignment. Three other isotopes have higher logft values for allowed β-decay, namely ^{17}N, ^{17}Ne and ^{18}N. With the higher limit found in this study only one higher logft value remains, from the β-decay of ^{17}N, which has a logft value of 7.1(1) [59]. A logft value of 6.9 is high for an allowed β-decay in the sd-shell and from other resonances in ^{20}Na a logft value of $\sim$4 is expected. This therefore makes a 1^+ assignment highly unlikely, strongly favouring instead a 3^+ assignment, for which a logft value of $\sim$12 is expected making the branch negligible.

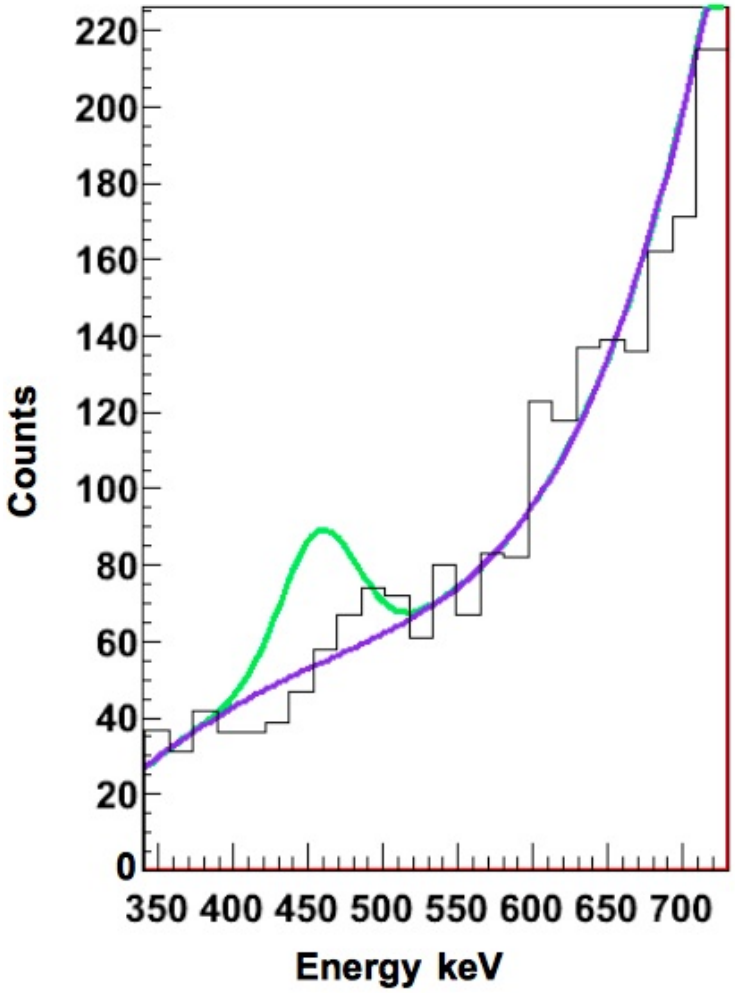

Figure 5.7 *The highlighted spectrum around the region of interest with the 4th order polynomial fitted to the background. The peak expected for a 0.1% branching ratio, the limit set by Ref. [87], is shown above the fitted background. It is clear that if the key resonance had this branching ratio then a proton peak would have been seen at 457(3) keV.*

5.2.3 Mirror Analysis of the 457 keV Resonance

The mirror ^{20}F can provide vital evidence to support the $J^{\pi} = 3^{+}$ assignment for the 457 keV key resonance from this study. In the mirror nucleus ^{20}F there are no states between 2194 and 2865 keV [97], therefore the analogue of the 2647(3) keV state must be above 2865 keV. The possible states that could be the mirror of the 2647(3) keV state in ^{20}Na are the 2865 (3^{-}), 2966 (3^{+}), 2968 (4^{-}) and the 3172 keV (0^{-}, 1^{+}) in ^{20}F. The two that have been argued most strongly as being the analogue state of 2647(3) keV in previous studies are the 2966 and the 3172 keV states. The 3488 keV state in ^{20}F has previously been considered to be the analogue state of the 2647(3) keV state, however, the shift in energies between the two states is considered too large. Also in the β-decay of ^{20}O the 3488 keV state is strongly fed [98], unlike the 2647 keV state in the β-decay of ^{20}Mg and has therefore been discounted.

The 3172 keV state in ^{20}F has been argued strongly in the past as being the analogue state to the 2647(3) keV key resonance in ^{20}Na. In the study by Fortune *et al.* [85], they point out that even the 3172 keV state requires a large energy shift to be paired with the 2647(3) keV state. The 3172 keV state in ^{20}F is also expected to have an exotic structure with a $(\mathrm{sd})^{6}\mathrm{p}^{-2}$ configuration [85]. It is believed to be a $2\hbar\omega$ intruder state as it decays mostly to the 984 keV 1^{-} level, which is expected for a $2\hbar\omega$ intruder state [97].

The 2647(3) keV key resonance is expected to have a strong $2\mathrm{s}_{1/2}$ single-particle occupancy, which in the mirror energy region can only be satisfied by the 2966 keV 3^{+} state. More evidence comes from the charge exchange reactions ^{20}Ne(^{3}He,t) and ^{20}Ne(t,^{3}He), where the population of the 2647(3) keV resonance is roughly an order of magnitude too large to be the analogue state of 3173 keV, though it is consistent with the 2966 keV state [76]. The 2647(3) keV key resonance in ^{20}Na is therefore paired with the 2966 keV 3^{+} state in ^{20}F. Section 5.3.2 will discuss the mirror assignments of the other states above the proton threshold in ^{20}Na in detail.

5.2.4 The Effect of the 457 keV Spin-Parity Assignment on the ^{19}Ne$(p,\gamma)^{20}$Na Reaction Rate

From the work on the key resonance in ^{20}Na in this β-delayed proton decay study of ^{20}Mg the ^{19}Ne$(p,\gamma)^{20}$Na reaction rate will be affected, due to both the new,

accurate resonance energy and the spin-parity assignment. The energy of the state has an exponential affect on the reaction rate so any slight change in the resonance energy can cause a large change in the reaction rate. The new evidence strongly suggesting a 3^+ spin-parity assignment for the key resonance at 457(3) keV will affect the resonance strength of this state, which has a linear dependence on the reaction rate. As was mentioned in Section 2.2.2, the resonance strength has two separate parts to it, ω and γ. γ is calculated from the widths of the ground state proton decay, γ-decay and the decay width of the total resonance. As there is no experimental data for the ground state proton decay and γ-decay widths these have to be extracted from the mirror state, the 2966 keV state in ^{20}F for the key resonance. Fortune *et al.* [85] published the most up-to-date limit on the resonance strength for a 3^+ spin-parity assignment, where they used the γ-decay width, ground and first proton decay width and lifetime for the 2966 keV state in ^{20}F. They also took into account the slight difference in the spectroscopic factors between the mirror states, including the Coulomb, charge asymmetry and charge independent reactions and combining this with isospin-nonconserving calculations they estimated the lower limit for the resonance strength to be 16 meV. Although this limit is higher than the upper limit found in Ref. [86], in Ref. [86] a value of 448 keV was used for the resonance energy which, due to the nature of the experiment, can have a large affect on the resonance strength limit measured. The change in energy may also have an affect on the limit calculated by Ref. [85] as the greater the energy of the resonance, the bigger the proton width. However, with the other uncertainties associated with calculating the resonance strength the difference in the proton width will be small in comparison and shall therefore be ignored. Therefore for the strength of the key resonance with a 3^+ assignment the lower limit of 16 meV shall be used [85].

For the resonance strength for the 1^+ assignment the value calculated by Vancraeynest *et al.* [84] of 6 meV will be used. Again, a lower resonance energy was used to calculate the resonance strength but, as has been previously mentioned, with all the other uncertainties involved the error this introduces into the calculation of the resonance strength will be small and therefore this will be ignored. Ref. [84] calculated this resonance strength value by taking the gamma partial width from Ref. [72] and the calculated proton partial widths using neutron spectroscopic factors from Ref. [99].

Fig. 5.8 shows the difference in the reaction rate for a 3^+ and a 1^+ spin-parity assignment and resonance energies of 448 keV and 457 keV. The increase in energy has decreased the reaction rate slightly for temperatures below $\sim$0.8 GK.

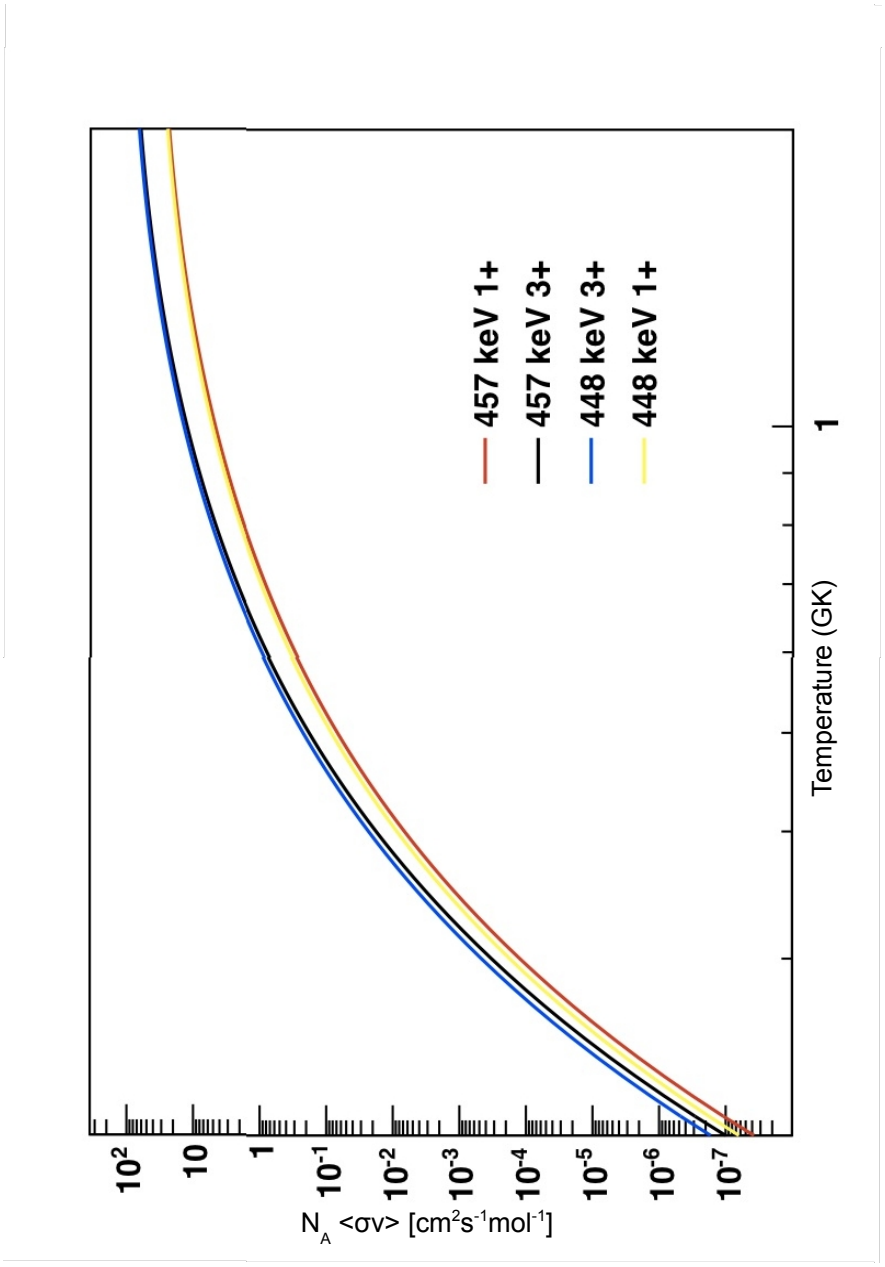

Figure 5.8 *The $^{19}Ne(p,\gamma)^{20}Na$ reaction rate for the 457 keV resonance showing the effect of the different spin-parity assignments and different resonance energies.*

A 3^+ spin-parity assignment results in a higher reaction rate at astrophysical temperatures than a 1^+ assignment with the difference in reaction rates increasing with increasing temperature.

5.3 The Level Structure of ^{20}Na above the Proton Threshold

After fully analysing the data in relation to the key astrophysical resonance at 457(3) keV, the rest of the resonances observed in this study were investigated. The next sections will describe the analysis of the other proton decay energies measured in the present experiment and their mirror assignments.

5.3.1 Proton Energies Measured in the Present Experiment

Many other resonances above the proton threshold in ^{20}Na were detected in this experiment. Most of the proton decay energies measured agree within errors with previous measurements. Table 5.1 gives the excitation energies, the proton decay energies and the final states that each proton decays to in ^{19}Ne [87] for this experiment, and Table 5.2 details all the excitations energies previously measured. The only slight disagreement in energies comes from the 1903(5) keV proton decay energy. This is compared to the previous measurement of 1928(16) keV [87], somewhat higher, although the energies do agree within 2σ.
Due to the increased sensitivity of the present experiment compared to previous β-delayed proton decay studies [87–89], a new proton was detected in the present study. The proton in question is at 885(15) keV. This new transition is very close to the 0^+ resonance at 887(2) keV detected in Ref. [81] from the ^{19}Ne(p,p) scattering, which supplied the 797(2) keV resonance energy used in the calibration and in the derivation of the key resonance energy. The energy for this new state was determined by fitting a 4th order polynomial to the background and skewed Gaussian fits to the 797(2) keV peak and the two indistinguishable peaks at $\sim$1050 keV. Two different fits were used, one with just the four fits previously mentioned and one with an extra skewed Gaussian function. The fitting procedure required rough positions for the centre of the skewed Gaussian functions and relative number of counts. Through multiple derivations the final energies of the

Table 5.1 *The proton decay energies, shown in Fig. 5.6. The final excitation energies were derived using the latest accurate threshold energy value [70], and assuming final states in ^{19}Ne as reported in [87].*

Excitation energy in ^{20}Na (keV)	Proton decay energy (keV)	Final state in ^{19}Ne [87]
2647(3)	457(3)[a]	0
2987(2)	797(2)[b]	0
3075(15)	885(15)	0
3860(10)	1670(10)[c]	[d]
4093(5)	1903(5)	0
4769(10)	2307(12)	275
	2344(15)	238
	1034(16)	1536
	1094(14)	1508
6267(16)	4077(16)	0
6522(16)	4332(16)[c]	0
	4057(20)	275
	4094(20)	238

a) Key astrophysical resonance energy derived here using a precise measurement of the energy difference of this state [77] with respect to the excited state at 2987(2) keV - see text for details.
b) Precise resonance energy measurement taken from a $^{19}Ne(p,p)$ resonant scattering study [81].
c) Proton calibration energies taken from the work of Görres et al. [89]
d) This proton line consists of a dominant branch to the ground state and two weaker transitions from the 4093(5) keV state in ^{20}Na to the 238 and 275 keV excited states in ^{19}Ne [87]. In the earlier work of Görres et al. [89], only a single transition was assigned at 1670(10) keV. Therefore a single centroid value for the peak structure is used for the 1670 keV proton decay.

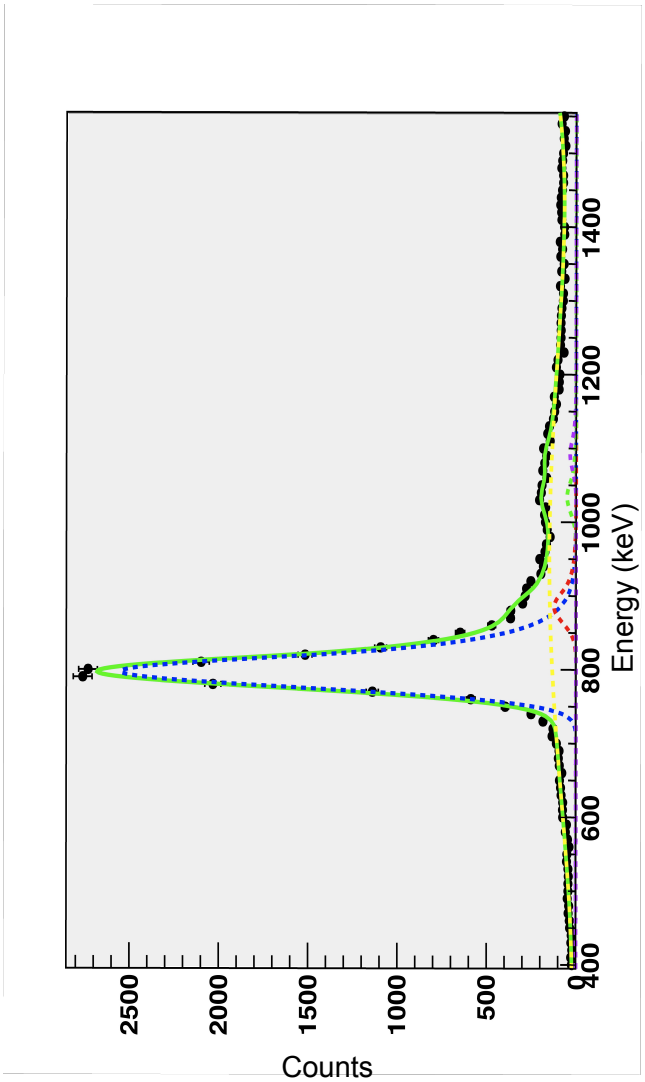

Figure 5.9 *Spectrum showing the combined fit used to find the energy of the 885(15) keV proton peak. The light green line shows the total fit, the yellow dashed line shows the background fit, the blue dashed line the 797 keV proton peak fit, the red dashed line the 885 keV proton peak fit, the green dashed line the 1034 keV proton peak fit and the purple dashed line the 1094 keV proton peak fit.*

centre of the Gaussian fits and number of counts in the peaks were found. By including a skewed Gaussian fit around ∼885 keV the χ^2 of the combined fit is reduced by a factor of ∼2. The final fit is shown in Fig. 5.9. The β-delayed proton decay branch for this state could be measured using the known branch 11.5(14)% for the 797(2) keV, resulting in a branch of 0.5(1)%, corresponding to a logft value of 5.41(9). No other branches were estimated for higher energy states or transitions due to the uncertainty in the proton escape fraction, which increases rapidly as the energy of the protons increases.

The remaining proton peaks in the spectrum that have not been discussed already are a combination of two or more proton decays. The ∼2340 keV proton peak is made up of two proton decays from the 4769(10) keV state to the 238 and 275 keV states in ^{19}Ne [87]. This wide proton peak has very few counts, making fitting the individual contributions difficult. The same fitting technique that was used to determine the energy of the 885(15) keV proton-decay energy was used to fit the two contributions that make up the ∼2340 keV proton peak, shown in Fig. 5.10. Through this technique the energy of the two contributions that make up the ∼2340 keV proton peak were measured to be 2310(12) and 2344(15) keV. From Ref. [87] it is known that the difference between these two contributions is 37 keV, in agreement with the difference measured here within errors. Two other proton decays from the 4769(10) keV state can be seen in this study at ∼1050 keV. The ∼1050 keV proton peak is made up of two transitions from the 4769(10) keV state to the 1508 and 1536 keV states in ^{19}Ne [87]. These two proton decays were included in the fit for the 885(15) keV proton peak shown in Fig. 5.9 and the energies for these decays were measured to be 1034(16) and 1094(14) keV.

A more complicated proton peak is found at ∼4080 keV. This proton peak contains one proton decay from the 6267(16) keV state to the ground state in ^{19}Ne and two proton decays from the 6522(16) keV state to the 238 and 275 keV states in ^{19}Ne [87]. The counts of the three proton decays here are low due to the three decays having small branching ratios [87] and a high percentage loss of protons due to the protons escaping out of the thin DSSD. Fig. 5.11 shows the fit for these three proton decays, with measured energies of 4057(20), 4077(16) and 4094(20) keV. The 4077(16) keV proton decay from the 6267(16) keV state is known to have a higher branching ratio than the two proton decays from the 6522(16) keV state, which is clear from the spectrum [87].

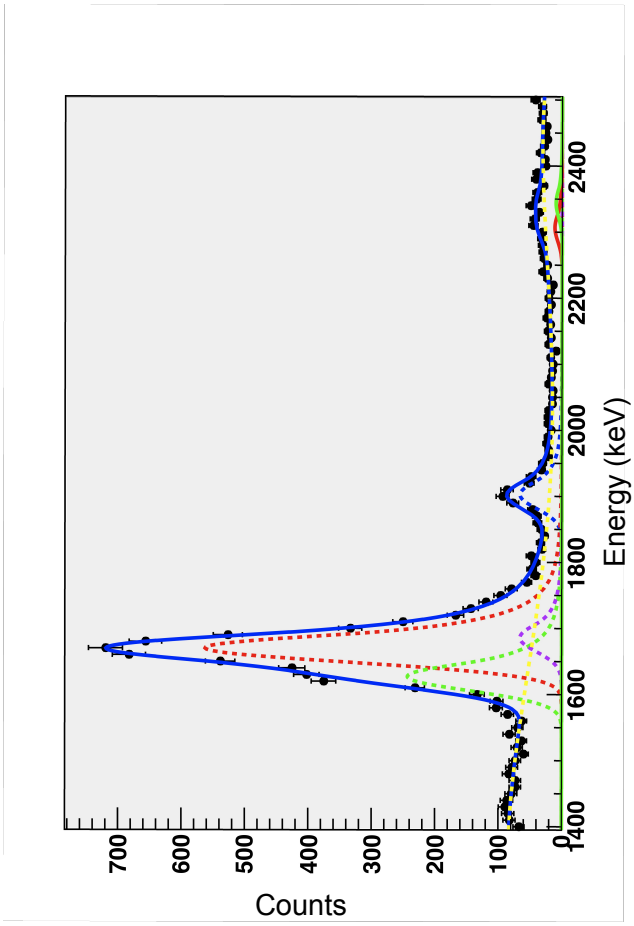

Figure 5.10 *Spectrum showing the contributions that make up the wide proton peak at ∼2340 keV, the 1903(5) proton peak and the 1670 keV proton peak. The ∼2340 keV peak is made up of a one contribution at 2310(12) keV and one at 2344(15) keV. Although the fits are shown for the different contributions in the 1670 keV proton peak, as this peak was used as a calibration point where only one peak was fitted, no energy values for the individual contribution have been given.*

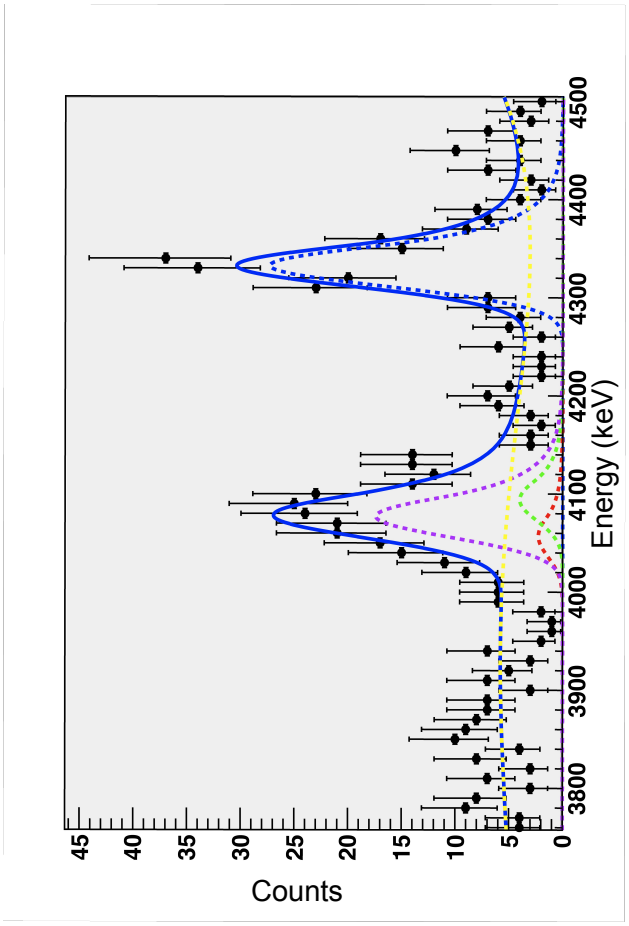

Figure 5.11 *Spectrum showing the contributions that make up the wide proton peak at ∼4080 keV. The ∼4080 keV peak is made up of two proton decays from the 6522(16) keV state, one proton decay at 4057(20) keV and one at 4094(20) keV and one proton decay at 4077(16) keV from the 6267(16) keV state.*

Table 5.2 *Table showing all states previously measured in ^{20}Na. For studies which measured the resonance energy rather than excitation energy, the proton emission threshold value given in the study rather than the new value is used to calculate the excitation energy.*

[46]	[73]	[74]	[72]	[75]	[77]	[88]	[89]	[87]	[81]	[100]	[69]	present
Shell-model	(^{3}He,t)	(p,n)	(^{3}He,t)	(^{3}He,t)	(^{3}He,t)	^{20}Mg(βp)	^{20}Mg(βp)	^{20}Mg(βp)	(^{19}Ne + p)	(^{3}He,t) re-analysis	(^{12}C,2n)	
	610(15)	580(15)	606(20)	595(20)							599.47(5)	
	802(15)	790(15)	808(20)	801(20)							798.56(6)	
	990(15)	993(15)	996(20)	996(20)				984.24(10)			984.5(5)	
											1031.9(7)	
	1347(15)	1353(15)	1338(20)	1350(20)							1348.9(4)	
											1828.91(13)	
											1836.8(5)	
	1832(15)	1843(15)	1841(20)	1819(20)							1848.2(7)	
	1967(20)		1993(20)	1992(20)							1991.7(6)	
2126	2034(20)	2016(20)	2064(20)	2100(40)							2059.2(6)	
2856	2637(15)	2651(20)	2649(20)	2640(20)	2646(9)	2657				2649(16)		2647(3)
2876	2842(15)	2852(20)	2863(40)	2860(20)	2857(9)					2867(11)		
2996	2967(20)		2972(13)	3010(20)	2986(9)	3046	3006(10)	3001(2)	2996(7)	2997(11)		2987(2)
3046		3053(20)	3035(15)		3056(9)	3046						
			3100(14)						3086(7)	3082(12)		3075(15)
	3302(30)			3290(20)						3324(11)		
3580	3644(30)	3636(20)		3690(60)							3698(1)	
	3840					3868	3869(11)	3874(15)				3860(10)
	4160			4150(60)		4090		4123(16)				4093(5)
				4560(60)								
								∼4800				4769(10)
	5200			5170(60)								
	5590			5430(60)				∼5600				
								6266(30)				6267(16)
						6440	6533(15)	6521(30)				6522(16)

5.3.2 ^{20}Na Level Scheme Above the Proton Threshold

From the numerous experiments that have been performed over the last few decades there is a wealth of information on the states in ^{20}Na. Table 5.2 details the excitation energies of all the states published previously. Ref. [69] identified and paired all states below the proton emission threshold in ^{20}Na with the analogous states in the mirror ^{20}F. Fig. 5.12 shows the decay scheme for ^{20}Na and it's

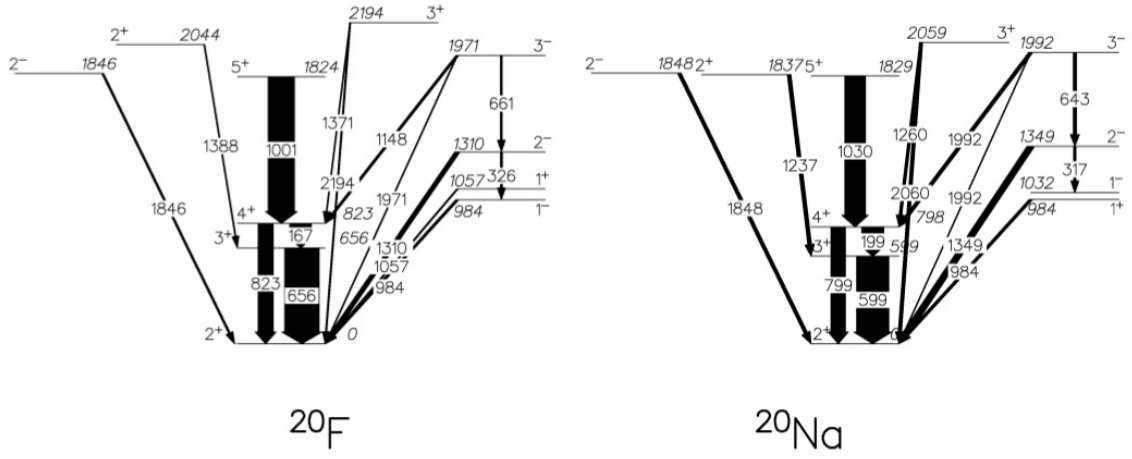

Figure 5.12 *Mirror scheme for ^{20}F and ^{20}Na for states below the proton-threshold in ^{20}Na [69].*

mirror ^{20}F under the proton emission threshold of ^{20}Na from Ref. [69]. For states above the proton emission threshold there is less certainty to the decay scheme. The energy and spin-parity of the key resonance at 2647(3) keV has already been discussed in Section 5.2 and has been identified as the mirror of the 2966 keV 3^+ state in ^{20}F. Precise energies for two resonances were determined in (p, p) scattering of ^{19}Ne at 797(2) and 887(2) keV [81]. The 887(2) keV resonance corresponds to an excitation energy of 3077(2) keV and was seen in the present β-delayed proton decay study (see Section 5.3.1 for more detail). The 797(2) keV resonance corresponds to an excitation energy of 2987(2) keV and has been paired with the 3488 1^+ keV state in ^{20}F, with the large Coulomb shift being associated with a large $2s_{1/2}$ component in the wave function [80, 85]. This state is the same as the 3001(2) keV state in Table 3 of Ref. [87]. As has been previously explained in Chapter 3, Ref. [87] used a value for the resonance energy of this state from a conference proceedings [90], which was later increased by 20 keV due to an incorrect treatment of energy responses of proton and alpha particles in silicon detectors and became the 797(2) keV resonance [77].
Table 3 from Ref. [87] gives a compilation of all results from previous experiments.

A compilation of (^{3}He,t) experiments leads to an adopted excitation energy of 2983(7) keV, with a spin-parity of $>3^-$ or $>4^+$ [87]. However, from the four experiments this state is compiled from only one measures the spin-parity of the state. The one paper that Ref. [87] takes the spin-parity assignment from is by Clarke *et al.* [75], where an angular distribution was performed. Clarke *et al.* went on to re-examine their data, comparing the angular distributions of their (^{3}He,t) and (t,^{3}He) experiments [76]. In this later paper Clarke *et al.* propose that the 3010(20) keV state is actually the mirror of the 3488 state 1^+ keV in ^{20}F [75]. As the original Clarke paper is the only evidence of a higher spin state at that energy, and as this work is in contradiction with Clarke *et al.*'s later work, it is clear that the 2983(7) keV state reported in Ref. [87] is actually the 2987(2) keV 1^+ state.

Another state is seen at 2858 keV in ^{20}Na in many of the previous studies. From Ref. [76] and the comparisons of angular distributions of states in ^{20}Na and ^{20}F, the 2858 keV state is paired with the 2857 3^- state. For negative parity 5p-1h states, the Coulomb energy difference is expected to be very small or negative for mirror states [80, 85], in agreement with this assignment.

In Smith *et al.*'s [77] high resolution study of the ^{20}Ne(^{3}He,t)^{20}Na reaction they report a state at 3056(9) keV. It could be argued that this state is the same as the 3077(2) keV state from Ref. [81]. However, as mentioned in Section 5.2.1, in Ref. [77] a magnetic spectrograph was used, which gives very accurate measurements of energies between states. Using this information the 3056(9) keV state becomes the more accurate 3057(3) keV, which is clearly not in agreement with the 3077(2) keV state. It should also be mentioned that the 3056 keV peak in Ref. [77] is wider than the other peaks in the spectrum, shown in Fig. 5.13 [77]. The left side of the 3056 keV peak is broader than the others suggesting another higher lying state, possibly the 3077(2) keV state.

In Lamm *et al.*'s [72] (^{3}He,t) study three different states at 2972(13), 3035(15) and 3100(14) keV were measured, in agreement with the 2987(3), 3057(3) and 3077(2) keV states. A subset of the original authors took this work and re-examined these three states [100]. Where Lamm *et al.* fitted three Gaussian functions to the wide peak at ∼3050 keV, Ref. [100] only fitted 2. Instead of two states at 3035(14) keV and 3100(15) keV, Ref. [100] quotes just one state at 3082(12) keV. From all previous results Ref. [100] found an average value of 3070(8) keV for the state but recognises the error that arises from the use of the mass of ^{20}Na in some of the studies. Ref. [100] also highlights that if you compare the resonance energies rather than excitation energies, therefore ignoring any errors from the mass of

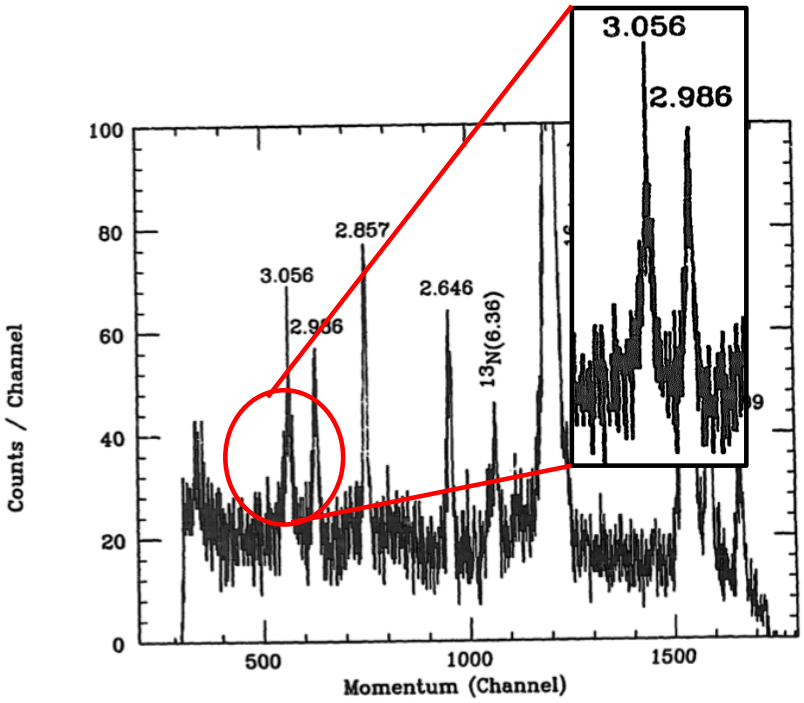

Figure 5.13 *Spectrum from Smith et al.. The highlighted section shows the 2986(9) keV peak and the 3056(9) keV peak. The left hand side of the 3056(9) keV peak is wider than the 2986(9) keV peak, suggesting the possibility of another state on the shoulder of the 3056(9) keV peak [77].*

^{20}Na, two very different resonance energies come to light, 857(5) keV and 887(2) keV. It is therefore sensible to conclude that there are two separates states here at 3057(3) and 3077(2) keV.

In the shell model study by Brown *et al.* [80], it was first argued on the basis of Coulomb energy shifts of negative-parity states that the 3057 keV state was the mirror of the known 2968 keV (4^-) state in ^{20}F. However, due to the error in the conference proceedings [90] this state was attributed to the 0^+ resonance, as the energy from the conference proceedings [90] was used instead of the published value, which is 20 keV higher [81]. Brown *et al.*'s original pairing will therefore be kept and the 3057(3) keV state will be paired with the 2968 keV 4^- state in ^{20}F.

One final state remains to be discussed. The 3172 keV state in ^{20}F, originally thought to be the mirror of the key resonance, has been assigned as either 0^- or 1^+ [101]. Fortune *et al.* [85] argued that this state is most likely to be a 1^+ state of 6p-2p character from its production in the ^{18}O(^{3}He,p) reaction [102]. Further strength to this state not having a predominate $(sd)^4$ configuration comes from the state not being fed by the β-decay of ^{20}O [98] or by neutron capture on ^{19}F [97]. For states with one or two holes the excitation energy in the proton-rich partner is expected to be higher [103]. There is only one state remaining below 3.6 MeV in ^{20}Na at 3315(9) keV [101]. From a process of elimination this state is paired with the 3172 keV state in ^{20}F. The non-observation of this state in the current β-delayed proton decay study of ^{20}Mg is consistent with the non-observation of the β-branch from the 3172 keV state in ^{20}F in the β-decay of ^{20}O. The pairing of the states in ^{20}Na just above the proton emission threshold with their mirrors in ^{20}Na is shown in Fig. 5.14. The definitive spin-parity assignments will now be input into the ^{19}Ne$(p,\gamma)^{20}$Na reaction rate and compared to previous estimates.

5.4 The ^{19}Ne$(p,\gamma)^{20}$Na Reaction Rate

To evaluate the rate of the reaction ^{19}Ne$(p,\gamma)^{20}$Na, the resonance strengths for the first four resonances above the proton threshold in ^{20}Na need to be determined. Most of the resonance values were taken from Ref. [84], except for the resonance strength for the key resonance, which was taken from Ref. [85] and is in agreement with the value measured in Ref. [84] of $\omega\gamma < 21$ meV. The resonance strength

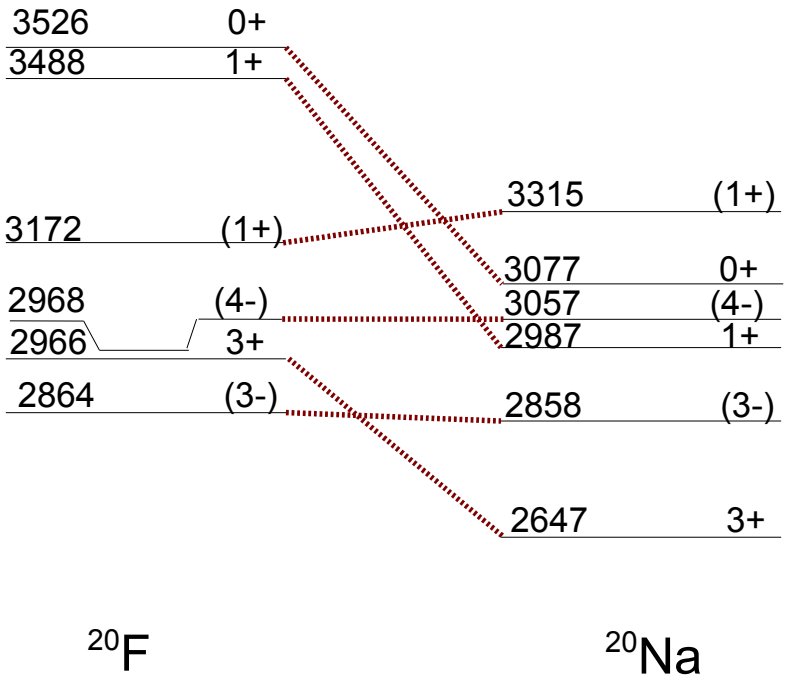

Figure 5.14 *Mirror scheme for states ^{20}Na and ^{20}F above the proton emission threshold in ^{20}Na.*

for a resonance in ^{20}Na is calculated using the equation,

$$\omega\gamma = \frac{2J_f + 1}{4}\frac{\Gamma_{p0}\Gamma_\gamma}{\Gamma} \tag{5.1}$$

where J_f is the spin of the ^{20}Na resonance and ^{19}Ne is in its ground state [84]. The total width is described by the equation,

$$\Gamma = \Gamma_\gamma + \Gamma_{p0} + \Gamma_{p1} + \Gamma_{p2}. \tag{5.2}$$

In Ref. [84] the single-particle proton widths were calculated using elastic scattering from a folding potential and were then scaled by spectroscopic factors calculated using the shell model. The partial gamma-decay widths for M1 and E2 transitions were found through shell model calculations, which are expected to produce reliable results [97]. For the one E1 transition the gamma partial width was adapted from Ref. [85]. The calculated widths for the 797 and 887 keV resonances agree with those measured in Ref. [81]. The direct capture reaction rate is taken from Vancraeynest *et al.* [84].

The individual reaction rates for the first four resonances, including the original two different spin-parity assignments for the key resonance, the direct capture rate and the total reaction rate are shown in Fig. 5.15. There is a clear increase in the rate for the ^{19}Ne$(p,\gamma)^{20}$Na reaction for a 3^+ spin-parity assignment for the key resonance compared to a 1^+ spin-parity assignment. Fig. 5.15 also shows how clearly the ^{19}Ne$(p,\gamma)^{20}$Na reaction rate is dominated by the 457 keV resonance, with the 797 keV resonance starting to have a slightly increased influence over $\sim$1 GK.

The present reaction rate has been compared to the most recent theoretical study [104], shown in Fig. 5.16. There is a large difference in the energy of three of the four resonances used in Ref. [104], especially for the key resonance and the 797 keV resonance. This could explain the disparity above $\sim$0.2 GK, where the current reaction rate is nearly an order of magnitude lower. From Fig. 5.8 the difference in the energy of the key resonance clearly had a large impact on the reaction rate, and that is also obvious here. A new theoretical study of the reaction rate using the most up-to-date resonance energies and spin-parity assignments would be desirable.

The results gained in the current experiment have great implications for X-ray bursters. The ^{19}Ne$(p,\gamma)^{20}$Na reaction decides the flow of nuclides up to higher masses and as such an accurate reaction rate calculation is very important. As previous direct reaction measurements used an incorrect resonance energy for

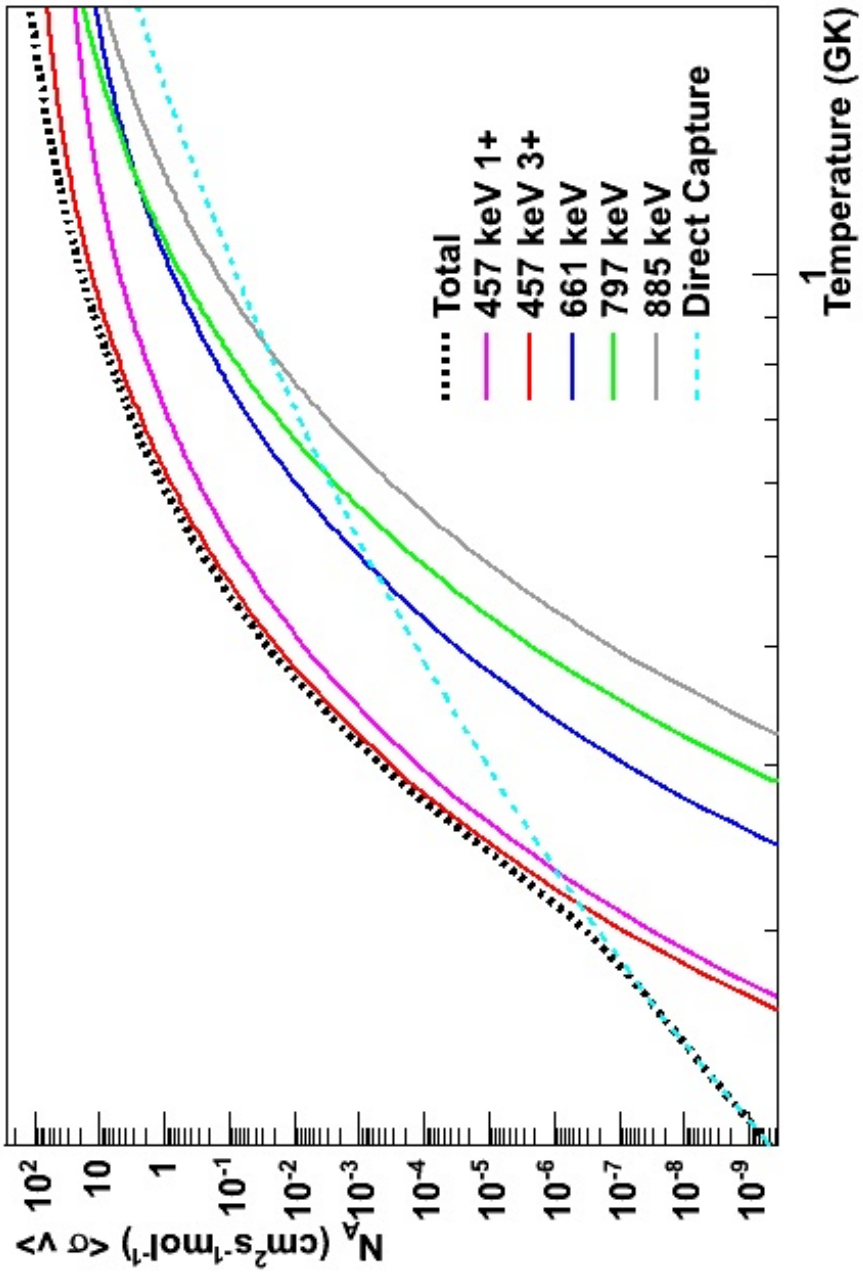

Figure 5.15 *The rate of the $^{19}Ne(p,\gamma)^{20}Na$ reaction for the four lowest resonances above the proton emission threshold in the compound nucleus ^{20}Na, with the different possibilities for the spin-parity assignment of the key resonance. The total reaction rate is calculated by combining the resonant reaction rates and the direct capture reaction rate [84].*

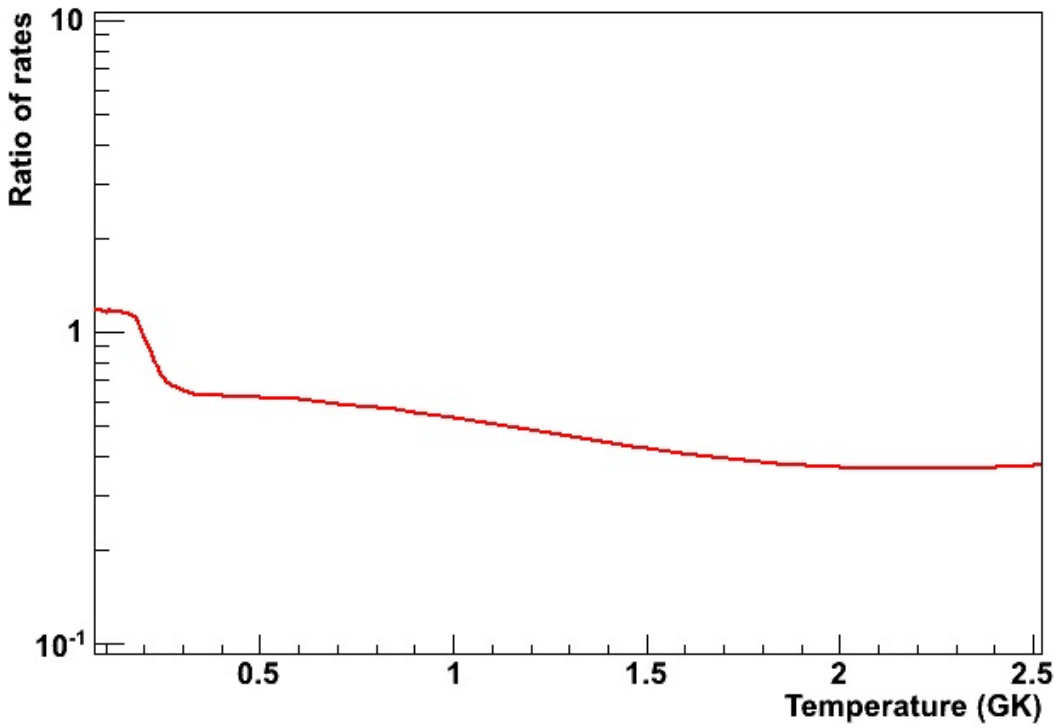

Figure 5.16 *Ratio of present total reaction rate to the most recent theoretical prediction [104].*

the key resonance at 457(3) keV, a new direct measurement to determine the resonance strength would be desirable. There is currently a proposal to study the direct reaction at TRIUMF submitted, which is set to be proposed to the next programme advisory committee.

Chapter 6

Level Structure of ^{30}S and the ^{29}P$(p,\gamma)^{30}$S Reaction Rate

The second experiment to be discussed in this thesis is a detailed γ-ray spectroscopy study of ^{30}S. In this thesis work, performed at the Argonne National Laboratory, USA, ^{30}S was produced via a fusion-evaporation reaction with a heavy target and a light ion beam. Similar to ^{20}Na, ^{30}S is a $T_z = -1$ isotope and it is astrophysically important for both novae and X-ray bursters, as discussed in Chapter 1. This chapter will detail the previous work on ^{30}S, the design of the current experiment and the current results.

6.1 Previous Work on ^{30}S

The ^{29}P$(p,\gamma)^{30}$S reaction rate in explosive astrophysical conditions is dominated by resonant capture to low-spin excited states above the proton emission threshold of 4395.6(7) keV in ^{30}S [105]. In particular, levels located between 4.5 and 5.6 MeV are expected to dominate the ^{29}P$(p,\gamma)^{30}$S reaction rate in classical novae and X-ray bursters as they lie within the Gamow Window ($E_{c.m.} \sim$ 100 - 1100 keV) for the temperature range 0.1 - 1.5 GK [106, 107].

There have been many experiments and studies aimed at gaining more information about the ^{29}P$(p,\gamma)^{30}$S reaction rate and the astrophysically important nucleus ^{30}S. The ^{29}P$(p,\gamma)^{30}$S reaction rate was first evaluated theoretically by Wiescher and Görres [106] and then later by Iliadis *et al.* [107]. In Ref. [107]

two states above the proton emission threshold at 4733(40) and 4888(40) keV, with spin-parities of 3^+ and 2^+ respectively were estimated using the isobaric mass multiplet equation (IMME) to dominate the reaction rate at astrophysical temperatures. The reaction rate values calculated in Ref. [107] agreed with the previous paper [106] for temperatures less than 0.06 GK and greater than 0.9 GK. However, for temperatures between 0.07 and 0.8 GK the reaction rate values deviated by up to 3 orders of magnitude [107]. In order to evaluate the reaction rate precisely the energy and spin-parity assignments for all states above the proton emission threshold in ^{30}S need to be determined.

The first experiment to see either of the states presumed to dominate the reaction rate was performed by Bardayan *et al.* [108] at ORNL Holifield Radioactive Ion Beam Facility (HRIBF). Using a proton beam and a ZnS target, the $^{32}\mathrm{S}(p,t)^{30}\mathrm{S}$ reaction was studied. Tritons were detected and identified using the silicon detector array SIDAR. This was the first experiment to detect the 4704(5) keV state. Angular distributions for this state were compared to DWBA calculations, however, these were consistent with both 3^+ and 2^+ spin-parity assignments. A tentative 3^+ assignment was given to this state based on the work by Iliadis *et al.* [107] and the expected energy of the 3^+ state. However, as the angular distribution for this state was inclusive, more work was required. No firm spin-parity assignments were found for states above the proton emission threshold [108].

A further independent $^{32}\mathrm{S}(p,t)^{30}\mathrm{S}$ experiment was performed a few years later by Setoodehnia *et al.* [109]. This study was performed at the Wright Nuclear Structure Laboratory at Yale University. Here protons were accelerated using the FSTU tandem Van de Graaff accelerator to 34.5 MeV and bombarded a target of CdS evaporated onto natural carbon foil. Tritons from the (p,t) reaction were focused at the spectrographs focal plane and momentum and energy losses were measured in the position sensitive ionisation drift chamber [109]. The two resonances expected to dominate the $^{29}\mathrm{P}(p,\gamma)^{30}\mathrm{S}$ reaction were detected in this experiment, with excitation energies measured to be 4693(5) and 4814(3) keV. No experimental measurement of the spin-parity of these two states was performed, however Setoodehnia *et al.* did perform their own IMME calculations and as such they tentatively assign the 4693(5) keV state $J^\pi = 3^+$ and the 4814(3) keV state $J^\pi = 2^+$ [109]. Other states above the proton emission threshold were also given tentative spin-parity assignments, with only one firm spin-parity assignment of $J^\pi = 3^-$ for the 5318(4) keV state. From the measurements of the energies of the two important resonances in ^{30}S, the $^{29}\mathrm{P}(p,\gamma)^{30}\mathrm{S}$ reaction rate was explored and

found to be up to 20 times larger than the rate found in Ref. [107].

Setoodehnia *et al.* [110] performed another experiment one year later, studying the ^{28}Si(^{3}He,$n\gamma$)^{30}S reaction. The experiment was performed at the University of Tsukuba Tandem Accelerator Complax (UTTAC), where the 12 UD Pelletron tandem accelerator was used to produce 9 MeV ^{3}He ions, which bombarded a 25 μm thick target foil of natural silicon [110]. In this experiment the two important resonances were measured to be 4688.0(4) and 4810.4(6) keV. Tentative spin-parity assignments were placed on these two states from comparing the measured branching ratio sequences with the prospective mirror assignments in ^{30}Si. The tentative spin-parity assignments for the 4688.0(4) and 4810.4(6) keV were $J^{\pi} = 3^{+}$ and 2^{+} respectively [110]. One further state was given a tentative spin-parity assignment, the 5132.7(4) keV state, but no states above the proton emission threshold were given firm spin-parity assignments.

The two most recent studies of ^{30}S were published by Almaraz-Calderon *et al.* [111]. The two studies conducted were aimed at investigating proton- and α-unbound states up to energies of $\sim$12 MeV in ^{30}S. The first study was performed at the Research Centre for Nuclear Physics at the University of Osaka, Japan. Here the ^{32}S$(p,t)^{30}$S reaction was investigated using a 98.7 MeV proton beam and a ^{32}S target. The resulting tritons were detected in a spectrometer. The second study was conducted at the Nuclear Science Laboratory of the University of Notre Dame, where the ^{28}Si(^{3}He,n)^{30}S reaction was studied using a 15 MeV pulsed ^{3}He beam and a natural silicon target. Sixteen liquid-organic scintillation detectors were used to measure the neutrons. Between the two experiments 53 states in ^{30}S were identified, with tentative spin-parity assignments for 16 of the states being given. Twenty-five levels were identified for the first time, however only one of the two states expected to dominate the ^{29}S$(p,\gamma)^{30}$S reaction rate at astrophysical temperatures was identified. The 4.6825(57) MeV state was weakly observed in the (p,t) study and no spin-parity assignment was given [111].

Although there has been much interest in the astrophysically important nucleus ^{30}S, so far only one state above the proton emission threshold in ^{30}S at 5318(4) keV has a definite spin-parity assignment [109]. Definitive spin-parity assignments and accurate resonance energies above the proton threshold are vital for gaining an accurate rate for the reaction ^{29}P$(p,\gamma)^{30}$S. A detailed gamma-ray spectroscopy study is a good way of measuring the energies of states and determining spin-parity assignments through the measurement of angular distributions, as discussed in Chapter 2.

6.2 Experimental Procedure

The current experiment utilised GAMMASPHERE, a germanium detector array system at Argonne. A beam of ^{3}He ions at 13 MeV and 5-pnA was produced by the Argonne Tandem Linac Accelerator System, ATLAS, which then bombarded a $\sim$120 μg/cm^2 ^{28}Si target placed at the centre of GAMMASPHERE. ^{30}S nuclei were produced through the fusion-evaporation reaction ^{28}Si(^{3}He,n)^{30}S via the 1n evaporation channel. The main fusion-evaporation channels open were the $1p$ and the $2p$ channels from ^{31}S to ^{30}P and ^{29}Si. γ-ray coincidence techniques were used in the analysis stage to select ^{30}S events.

6.2.1 ATLAS

ATLAS is a superconducting linear accelerator, able to produce a range of stable beams of isotopes from protons to uranium. ATLAS consists of a sequence of machines with each accelerating charged atoms, feeding the beam into the next machine for additional energy. The initial production of the beam starts in one of two 'injector' accelerators: a 9 MV electrostatic tandem Van de Graaff or a 12 MV low-velocity linac and electron cyclotron resonance, ECR, ion source, known as the Positive Ion Injector (PII).
The main body of ATLAS consists of an initial 20 MV 'booster' linac and the 20 MV ATLAS linac. There are 62 superconducting split-ring resonators that create an accelerating field through the linac. The outer housing of the resonators is made from niobium bonded explosively to copper. The interior components are made from pure niobium, with liquid helium in direct contact for cooling. Each resonator is individually controlled, allowing individual adjustment of the RF phases and therefore allowing a wide range of effective velocities. The beam is steered and focused by superconducting solenoids in-between the resonators, providing magnetic fields. The accelerating structure of ATLAS consists of a large electric charge that flows back and forth 97 million times a second in the drift tubes. Between the tubes there is a potential difference of $\sim$800,000 V. Fig. 6.1 shows the floor plan for ATLAS. For this experiment the ^{3}He beam was directed towards the target area IV, where it bombarded a ^{28}Si target.

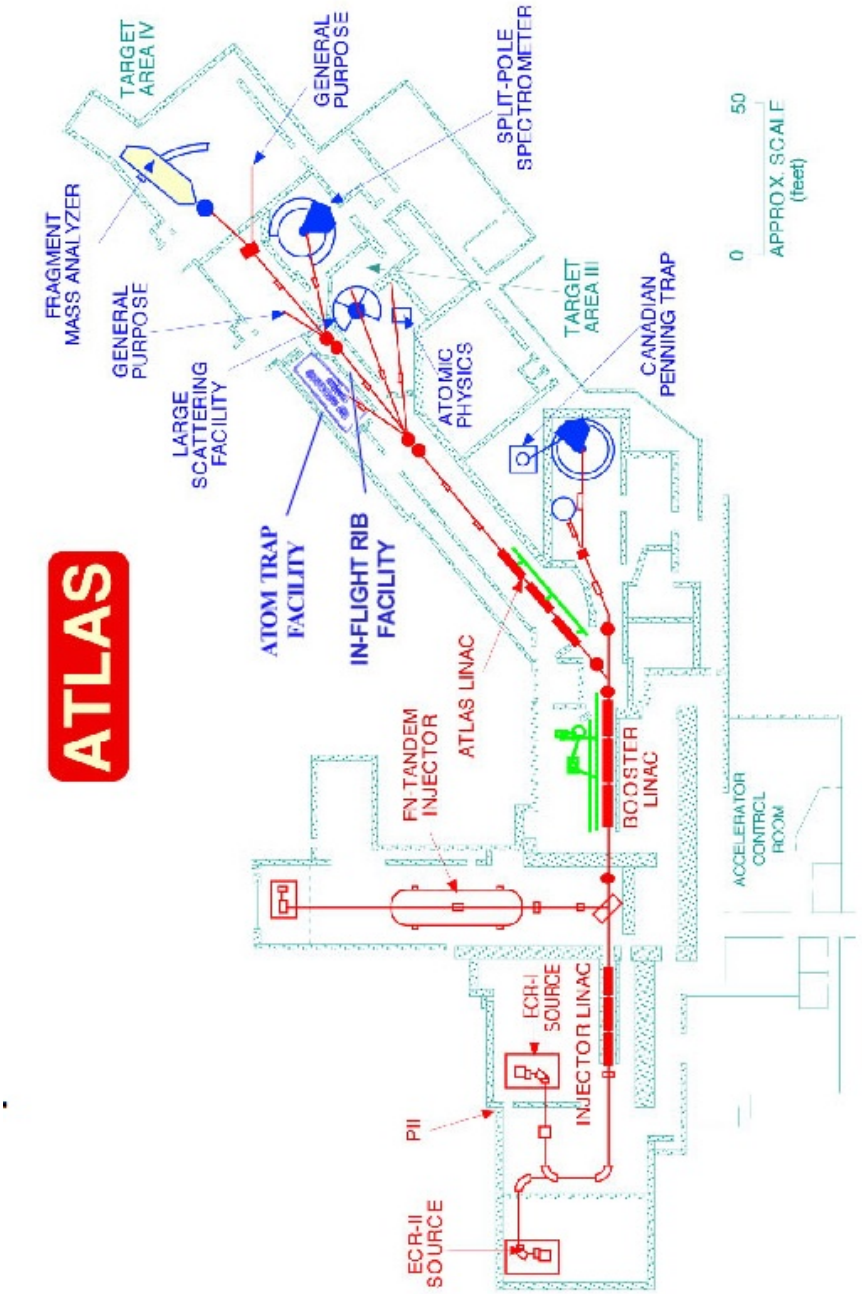

Figure 6.1 *Floor plan of ATLAS [112].*

6.2.2 GAMMASPHERE

GAMMASPHERE is a detector array system that is designed to detect prompt electromagnetic radiation of energies from 50 keV to 8 MeV, consisting of 122 polyhedrons (110 hexagons and 12 pentagons). The hexagons are detector modules and the pentagons make up the support structure and the entrance and exit of the beam line. The detector modules are in 17 different rings of constant angle θ with respect to the beam, allowing the energy and angular distribution of the γ-radiation to be detected and measured. Table 6.1 shows the number of

Ring	No. of detectors	θ(degrees)	$\cos^2\theta$
1	5	17.27	0.911
2	5	31.72	0.724
3	5	37.38	0.631
4	10	50.07	0.412
5	5	58.28	0.276
6	10	69.82	0.119
7	5	79.19	0.035
8	5	80.71	0.026
9	10	90.00	0.00
10	5	99.29	0.026
11	5	100.81	0.035
12	10	110.81	0.119
13	5	121.72	0.276
14	10	129.93	0.412
15	5	142.62	0.631
16	5	148.28	0.723
17	5	162.73	0.911

Table 6.1 *Ring number and corresponding angle θ with respect to the beam line. $cos^2\theta$ is included to demonstrate the symmetry of the system.*

detectors in each ring and the associated angle.

Each individual γ-ray module contains a n-type high-purity germanium detector, a Compton suppression shield, electronics and cryogenics. The germanium detectors have individual solid angles of 0.053 sr and opening angles of 7.4^0. If all 110 modules are working and online there is a nearly 4π coverage by the germanium detectors. In the current experiment 97 of the 110 modules were in operation. Two types of γ-ray detectors are used, made from relatively high-Z materials giving a high probability that the γ rays will interact via the photoelectric effect within the detector volume. The germanium crystals are 71 mm in diameter and 84 mm long and give a measurement of the energy of

γ rays that interact with it. The Compton suppression shield is made from Bismuth germanate (BGO). BGO shields have poor energy resolution, >6 %, but they detect a large percentage of the γ rays due to the density of the system. The coolant system uses liquid nitrogen and is used with every detector module, reducing the thermal energy of valence electrons across the band gap into the germanium crystals. Fig. 6.2 shows a schematic drawing of a detector module of

Figure 6.2 *Schematic drawing of a detector module in GAMMASPHERE [113].*

GAMMASPHERE, with the individual components labelled.
There are three different scenarios that can occur within a detector module. The first and the most desirable occurs when a photon deposits all of it's energy into a germanium crystal via the photoelectric effect. The second is where photon Compton scattering occurs out of the germanium crystal and energy gets deposited in the BGO shield. The third is where a photon misses the germanium crystal completely and deposits all it's energy in the Hevimet shield. The second two events are processed in anti-coincidence with the germanium crystal and the events are vetoed.

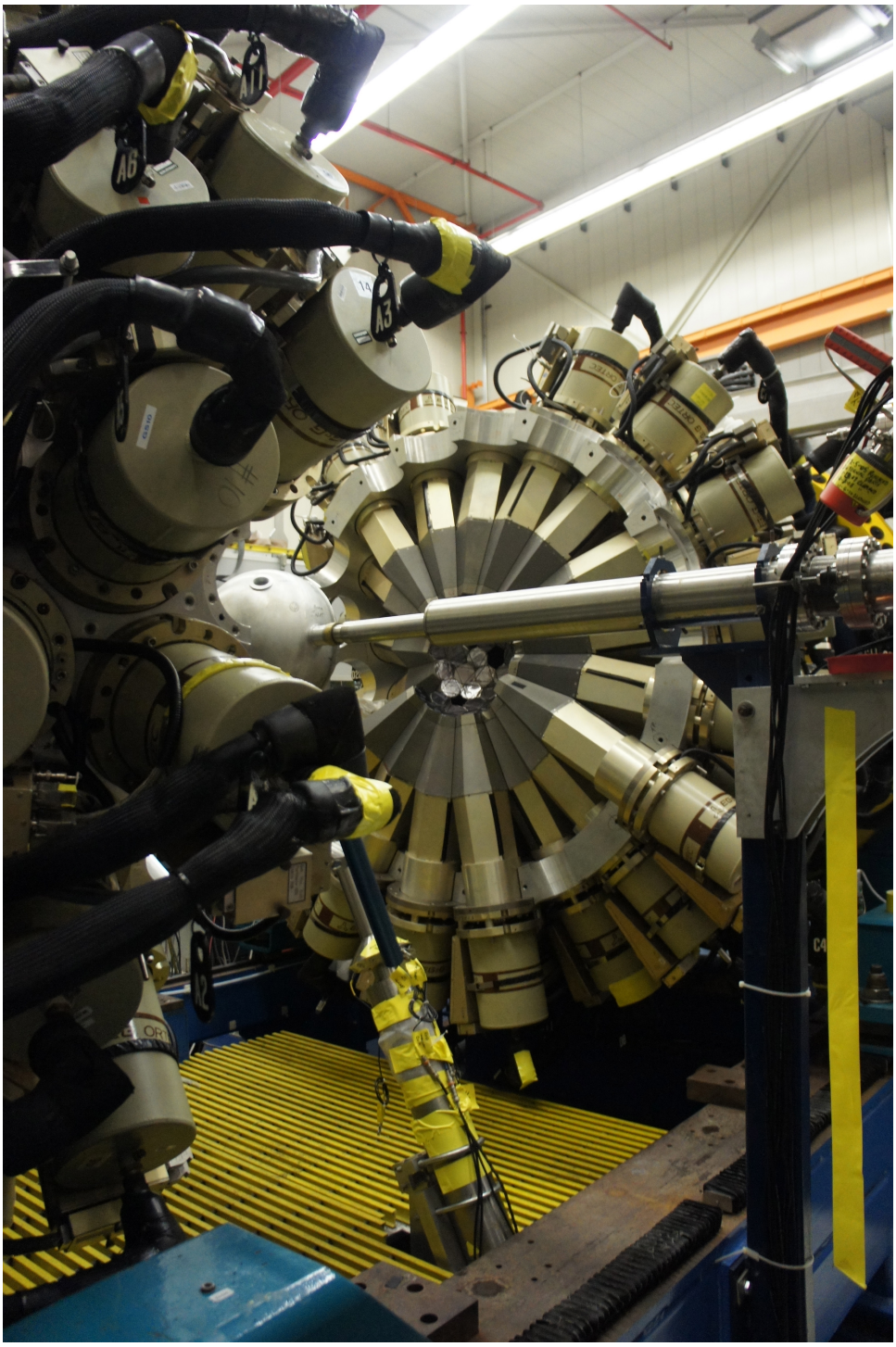

Figure 6.3 *Picture of GAMMASPHERE open.*

The resolution of the γ rays detected in the germanium crystals is dominated by Doppler broadening due to the motion of the recoiling nucleus. The opening angle θ of the germanium detector dictates the extent of the Doppler broadening. To

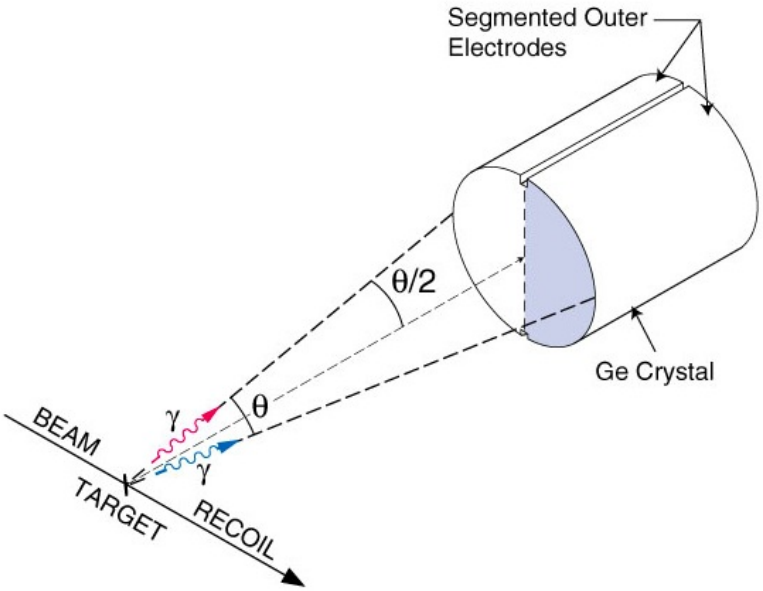

Figure 6.4 *An array module of GAMMASPHERE electrically segmented into 2 D-shaped halves [114].*

improve the granularity of the array modules with an opening angle greater than 0^o, $\sim$70 modules are electrically segmented into 2 D-shaped halves, shown in Fig. 6.4. For high-resolution signals the total energy is read from a common electrode at the centre and low-resolution signals are read separately from each half. This causes the effective angular size of the germanium crystal to be reduced by a half, therefore improving the total resolving power of the GAMMASPHERE array by 2. The total photopeak efficiency for the 110 detectors is estimated to be 10% for 1.3 MeV γ rays, resulting in a $<$2.4 keV resolution. The high resolution of GAMMASPHERE enables the energy of γ rays to be determined to a high degree of accuracy.

Figure 6.5 *Picture of the target and stand used in the current experiment.*

6.3 Preliminary Analysis

6.3.1 Calibration of GAMMASPHERE

For the calibration of GAMMASPHERE two radioactive γ-ray sources were used, ^{152}Eu and ^{56}Co. These sources were placed at the target position in GAMMASPHERE, shown in Fig. 6.5, and data was collected. This data was used to determine the relationship between the channel number and the actual energy, and the detection efficiency of GAMMASPHERE. The fitting programme 'gf3' was used to measure the centroid, area and associated error for each of the strong γ-decays in each source [68]. These were fitted to the equation,

$$E_\gamma = a_0 + a_1 x + a_2 x^2 ..... \tag{6.1}$$

where a_0, a_1 and a_2 are constants and x is the channel number. Energy calibrations for GAMMASPHERE normally require no more than a first or second order fit. For the present experiment a second order fit was used. The constants a_0, a_1 and a_2 were calculated using the 'ENCAL' code in the RadWare software programme.

In order to gain the relative efficiency for the modules in GAMMASPHERE a relative efficiency curve was produced. This required the areas of the fitted

photopeaks to be compared with known relative intensities of γ-ray lines from the sources used. Once the relative intensities were normalised they could be combined into the efficiency curve,

$$E = exp[(A + Bx + Cx^2)^{-G} + (D + Ey + Fy^2)^{-G}]^{-1/G} \tag{6.2}$$

where E is the relative efficiency and x and y are,

$$x = ln(Ey/100keV) \tag{6.3}$$

$$y = ln(Ey/1000keV) \tag{6.4}$$

with Ey in keV [115]. The seven parameters are constants and are found by fitting the efficiency curve in 'EFFIT' from the RadWare software package. Efficiencies at low energies are described by the constants A, B and C, whereas the efficiencies at higher energies are described by the constants D, E, and F. The final parameter, G, is an interaction parameter between the two regions and provides the efficiency at the turnover point.

6.3.2 Doppler Correction

In the type of experiment that was performed here the velocity of the recoiling ion produces a Doppler shift, therefore the energy of the γ ray measured is not the true energy of the γ ray. For a γ ray produced from a source moving with velocity v, detected at an angle θ with respect to velocity, the measured energy $E_{\gamma'}$ is related to the true energy $E_{\gamma 0}$ by the relativistic Doppler equation,

$$E_{\gamma'} = E_{\gamma 0}\frac{(1-\beta^2)^{1/2}}{1-\beta\cos\theta} \tag{6.5}$$

where β=v/c. However, in this experiment the recoils were moving non-relativistically therefore the non-relativistic formula was used,

$$E_{\gamma'} = E_{\gamma 0}(1+\beta\cos\theta). \tag{6.6}$$

It is reasonable to assume that the distribution of recoil velocities for the same isotope are narrow and therefore a mean value of β can be calculated from classical

considerations and used in the data sorts.

6.4 Main Analysis

Once the calibrations and Doppler corrections had been applied to the data the main analysis could be started. This involved looking at the γ-ray singles spectrum, γ-γ coincidence matrices and γ-γ-γ coincidence cubes, using the computer programmes 'gf3', 'ESCL8R' and 'LEVIT8R' respectively from the Radware software package [68]. The γ-ray singles spectrum was used to fit the two strongest transitions, the only 2 γ-decays seen in the singles spectrum. The γ-γ coincidence matrices and the γ-γ-γ coincidence cubes were used to fit the γ-ray transitions that were not seen in the γ-ray single spectrum as well as providing information on the decay scheme.

For a two-dimensional matrix, counts at a particular location must have two simultaneous γ rays of energy E_1 and E_2 measured, with the matrix symmetric about x=y. Similarly for a three-dimensional cube, for a count at a particular location three simultaneous γ rays of energy E_1, E_2 and E_3 must be measured, with the cube symmetric about x=y=z.

To perform the analysis a 'gate' is set, where the energies of one of the transitions is specified and a projection is made onto the remaining axis. This creates a one-dimensional axis, which should contain only transitions that are in coincidence with the gated transition. A level scheme can therefore be completed by determining the coincidence relationships between the transitions in the matrices and cubes.

When determining whether or not a particular assignment in a level scheme is correct two rules must be obeyed. The first is that the total energy from parallel paths must be equal, demonstrated in Fig. 6.6. The second is that the spins of the final and initial levels reflect the angular momentum carried away by the γ-ray transitions. To determine the angular momentum carried away the angular distributions must be measured.

In order to study the angular distributions for γ-ray transitions the relative efficiencies of each individual ring of detectors was required due to the different number of detectors in each ring. This was performed in the same way as the overall efficiency for the data as described in section 6.3.1, but for the individual rings. Once this was determined, and the individual ring spectra were generated,

the intensity of the γ-ray transitions could be compared as a function of $\cos^2\theta$. As angular distribution is expected to be a function of $\cos^2\theta$, pairs of rings on opposite sides about 90^o were combined. The peak areas for a given transition were measured in the combined rings and the area was divided by efficiency for each respective ring and relative intensities were fitted with,

$$W(\theta) = 1 + a_2 P_2 \cos^2\theta + a_4 P_4 cos^2\theta \tag{6.7}$$

using 'LEGFT' in the RadWare software programme, where $P_{2,4}$ are Legendre polynomials and $a_{2,4}$ are a_k coefficients. These are used to determine the angular momentum carried away by the γ-ray transition as described in Chapter 2. Two examples of the angular distributions of two of the transitions measured are shown in Fig. 6.7 and Fig. 6.8.
Due to the low statistics for some of the γ-ray transitions an additional angular correlation analysis was performed. The R_{dco} ratio is a ratio of the γ-ray intensity at forward and backward angles to the intensity at 90^o,

$$R_{dco} = I(0^o) + I(\sim 180^o)/I(\sim 90^0). \tag{6.8}$$

Using known levels from this experiment, R_{dco} values were found to be 1.15(3) for $\Delta J = 0$, 0.57(4) for $\Delta J = 1$ and 1.30(5) for $\Delta J = 2$. Once the energy and ΔJ of the level is determined, the current result can be compared to previous results, shown in Tab. 6.2, and the mirror ^{30}Si. The spin-parity and mirror assignment of the level can then be derived.

6.4.1 Subthreshold Level Structure of ^{30}S

The proton emission threshold energy for ^{30}S is relatively low with only 4 measured states below it. The lowest state at 2210.1(1) keV was seen in the ungated spectrum, shown in Fig. 6.9. The other γ ray seen in the ungated spectrum shown in Fig. 6.9 is from the 3404.1(1) keV state to the 2210.1(1) keV state, producing a γ ray of energy 1194.1(1) keV. The excitation energies of these states are in good agreement with previous measurements within errors, shown in Table 6.2. From an angular distribution study of the observed 2210 and 1194 keV γ rays coincident with each other a_2 and a_4 values of 0.14(1)/-0.08(2) and 0.06(1)/0.00(2) respectively were obtained, consistent with $\Delta J = 2$ and 0

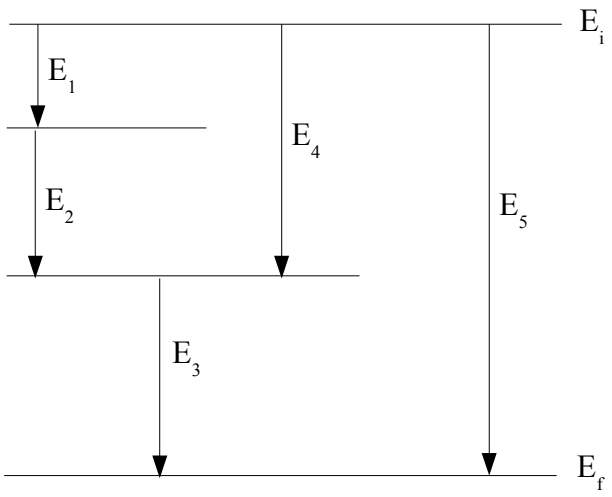

Figure 6.6 *A schematic diagram showing γ-ray decay sequences. $E_1 + E_2 + E_3$ and $E_4 + E_3$ must equal E_5.*

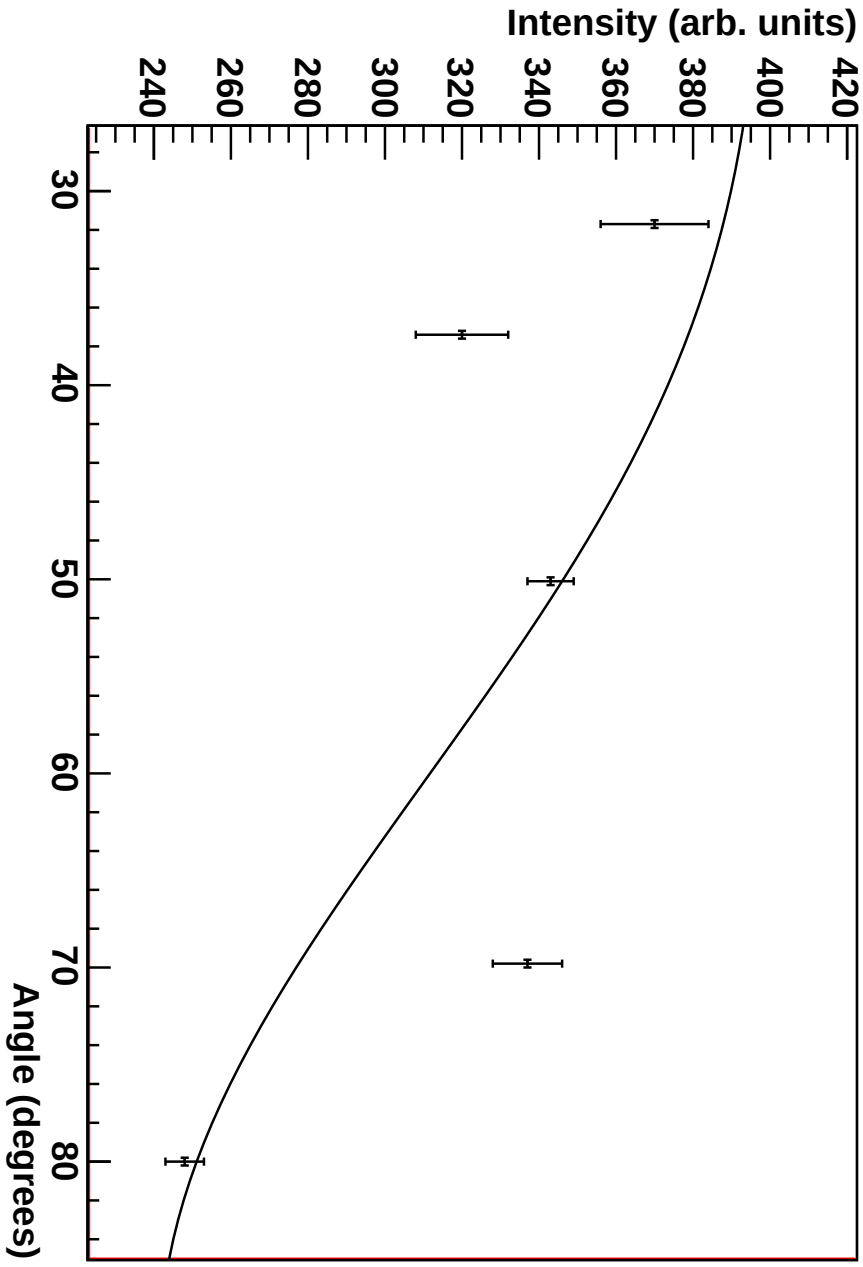

Figure 6.7 *The angular distribution for the 2922 keV γ-ray l=2 transition. See text for more details.*

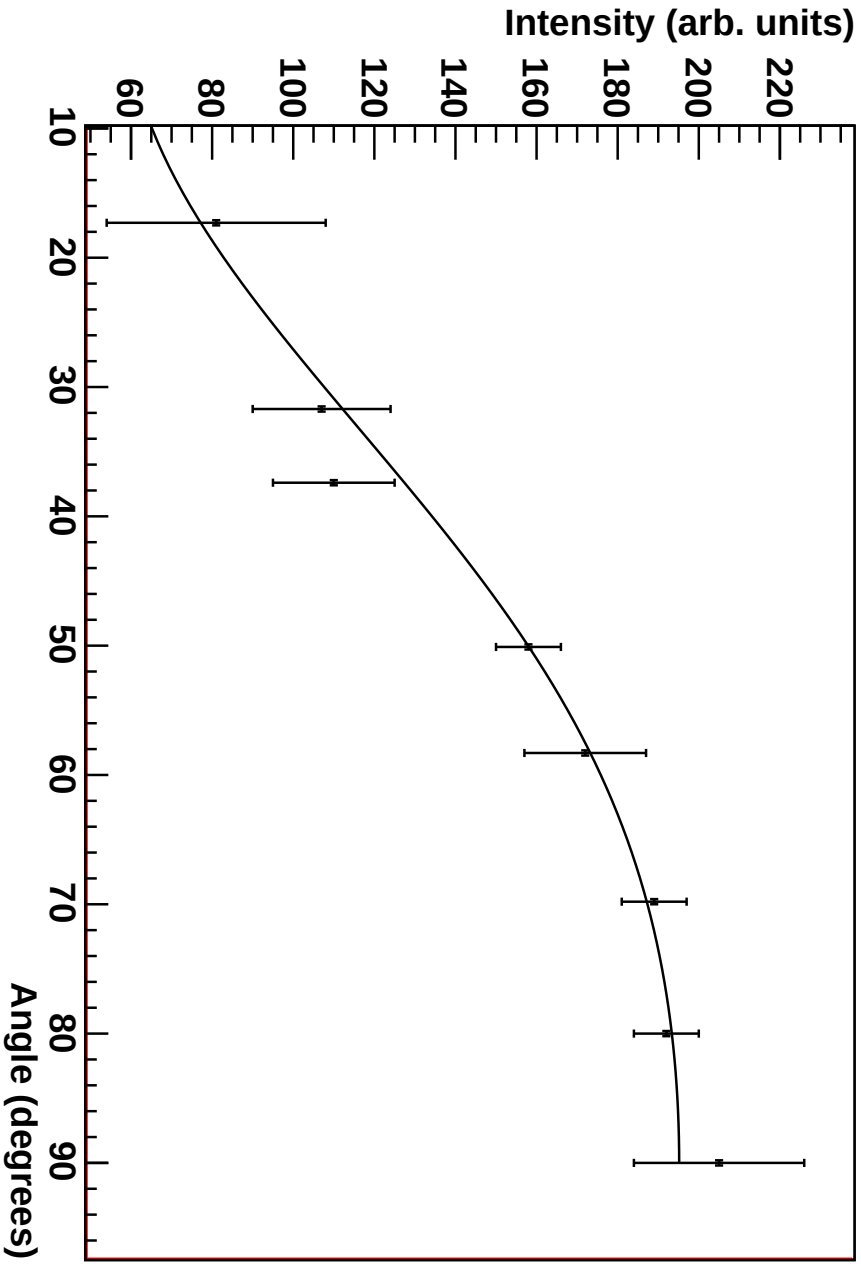

Figure 6.8 *The angular distribution for the 2477 keV l=1 γ-ray transition. See text for more details.*

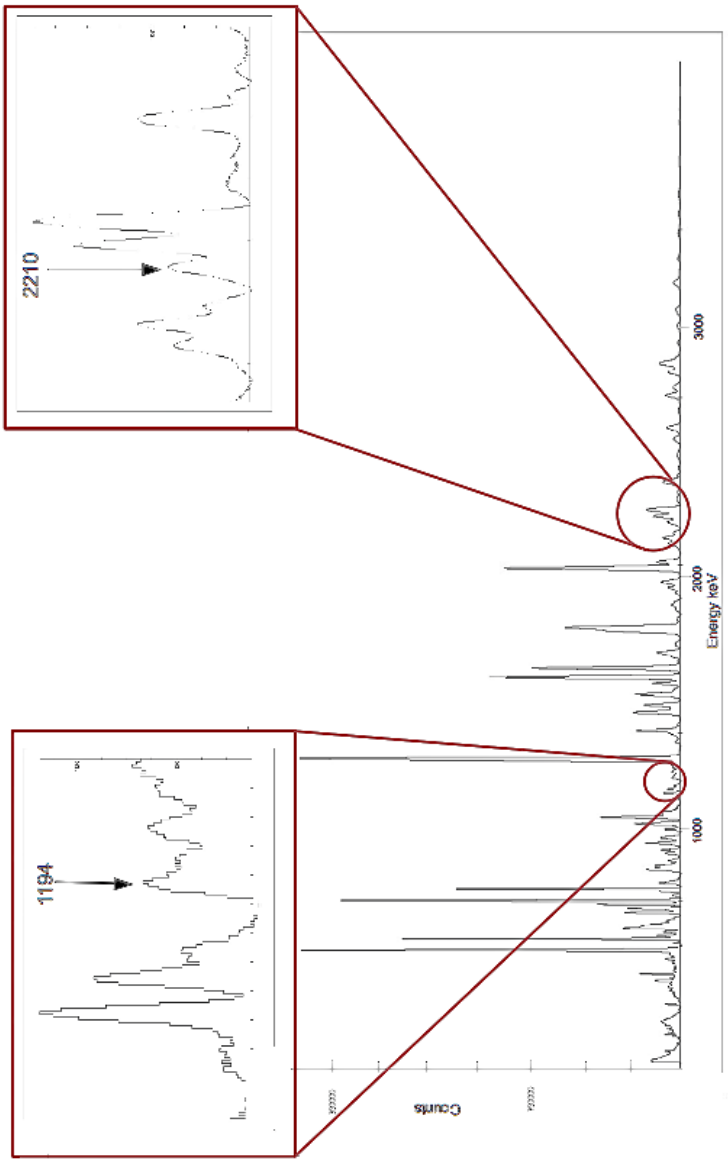

Figure 6.9 *γ-ray singles spectrum. The 1194.1(1) and the 2210.1(1) keV γ rays are shown in the highlighted areas. The main source of contamination came from ^{30}P and ^{29}Si.*

transitions respectively. The 2210 and the 3404 keV states were therefore assigned $J = 2$. Previous studies [108, 109, 116] have assigned spin-parity assignments of 2^+ to both these states, therefore for this experiment we consequently adopt the assignments 2_1^+ and 2_2^+ for the 2210 and 3404 keV states.
The final two states below the proton emission threshold of ^{30}S seen in this experiment were seen in a gate on the 2210.1(1) keV γ ray. Two γ-ray transitions are seen at 1457.9(4)and 1467.0(4) keV, corresponding to states at 3668.0(4) and 3677.1(4) keV, in agreement with previous measurements within errors. The 3677 keV state had previously been tentatively assigned as 1^+ [108]. The present γ ray observed from the 3677 keV state to the 2^+ 2210 keV state was found to have a_2/a_4 values of -0.09(13)/-0.12(14) and a R_{dco} ratio of 0.41(34), consistent with a $\Delta J = \pm 1$ indicating that the 3677 keV has a spin assignment of either $J = 1$ or 3. From examining the mirror ^{30}Si in the energy range 3.0-4.5 MeV there are no $J = 3$ states, and only one 1^+ state that is known to exhibit a strong γ-ray branch to a 2_1^+ state [117, 118]. Therefore the 3677 keV state is assigned $J^\pi = 1_1^+$. The final γ-ray transition below the proton emission threshold at 1458 keV was measured to have an isotropic angular distribution, implying a $J = 0$ spin assignment for the 3668 keV state in ^{30}S. Comparing this to the mirror nucleus ^{30}Si, the 0_2^+ 3788 keV level is the only $J = 0$ state in the energy range 3.0-4.5 MeV [118], therefore the 3668 keV state in ^{30}S is assigned $J^\pi = 0_2^+$.

6.4.2 Level Structure Above the Proton Emission Threshold in ^{30}S

The 4687.6(2) keV level

The lowest state above the proton emission threshold in ^{30}S is at 4687.6(2) keV, with two transitions seen from this state to the 2210 and 3404 keV 2^+ states, producing γ rays of energy 1283.4(3) and 2477.4(1) keV. The angular distribution for the 2477.1(1) keV transition is shown in Fig. 6.8. These two transitions were also seen in Ref. [110] with energies of 1283.3 and 2477.1(2) keV, in agreement with the energies found here. The energy of the 4687.2 keV level also agrees with the energy measured in Ref.'s [109–111]. The 1283.4(3) γ ray was seen in a gate on the 2210 keV γ ray, and more clearly seen in a coincidence cube gated on the 2210 and 1193 keV γ rays, shown in Fig. 6.12. The 2477.4(1) keV γ ray

Table 6.2 *Table comparing all previously measured states in ^{30}S.*

(p,t) [116]	J^π [116]	(^{3}He,$n\gamma$) [119]	J^π [119]	(^{3}He,n) [120]	J^π [120]	(β^+p) [121]	(p,t) [108]	J^π [108]	(^{3}He,$n\gamma$) [122]	(p,t) [109]	J^π [109]	(^{3}He,$n\gamma$) [110]	J^π [110]	$(p,t)/(^3\mathrm{He},n)$ [111]	J^π [111]	present	J^π
g.s.	0^+						0000(4)	0^+				g.s					
2239(18)	2^+	2210.7(5)	2				2210.7[a]	2^+	2209.9(11)	2210.6[a]		2210.9(3)	2^+	2208.5(22)		2210.1(1)	2^+
3438(14)	2^+	3402.6(5)	1,2				3402.6[a]	2^+	3402.2(14)	3402.6[a]		3404.7	2^+	3405.8(12)		3404.1(1)	2^+
		3667.5(10)							3664.2(13)					3600(26)		3668.0(4)	0^+
3707(25)	(0^+)	3676(3)	1				3680(6)	(1^+)		3680(4)				3677.3(70)		3677.1(4)	1^+
							4704(5)			4693(5)	(3^+)	4688.0(4)	(3^+)	4682.5(57)		4687.6(2)	3^+
										4814(3)	(2^+)	4810.4(6)	(2^+)			4808.7(3)	2^+
										5136[a]	(3^+)	5132.7(4)	(4^+)	5130.0(18)	4^+	5132.7(4)	4^+
		5136(2)	(4^+)	5145(10)													
							5168(6)	$4^+/0^+$									
5207(22)						5217.4(7)				5226(3)	(0^+)			5217.8(18)	0^+	5218.8(3)	3^+
5306(25)				5288(10)	3^-					5318(4)	3^-			5312.1(20)	3^-		
5426(25)				5425(10)	(1,2)	5389(2)	5383(8)	$(3^-,2^+)$		5396(4)	(2^+)			5382.0(7)	2^+		
5897(27)				5912(10)	(3,4)	5842(4)	5843(5)	(1^-)						5835.5(13)	4^+	5848.0(4)	4^+

was seen in a gate on the 2210 keV γ ray, shown in Fig. 6.11. From an angular distribution of the 1283 and 2477 keV γ rays, a_2/a_4 values of -0.10(9)/-0.11(11) and -0.47(3)/-0.04(4) respectively reveal $\Delta J = \pm 1$, indicating a $J = 1$ or 3 spin assignment. From a comparison with the mirror nucleus in the energy range 4.2-5.0 MeV, there are no known $J = 1$ states and only one $J = 3$ state at 4828 keV with $J^\pi = 3_1^+$ [117, 118]. The 4688 keV state in ^{30}S is therefore assigned $J^\pi = 3_1^+$, corresponding to a resonance energy of 292.0(9) keV.

The 4808.7(3) keV level

A proton-unbound state at 4808.7(3) keV is indicated due to a low intensity γ ray at 2598.6(4) keV observed in a gate on the 2210 keV state, shown in Fig. 6.11. This γ-ray transition was also seen in Ref. [110] were it was measured to have an energy of 2599.5(5) keV, in agreement with the energy measured here. The precise excitation energy of the state however, is in slight disagreement, with the energy found in Ref. [110] at 4810.4(6) keV compared to 4808.7(3) keV measured here. Another transition was seen for this state at 1404.5(1) keV shown in the Fig.'s 6.11 and 6.12, also seen in Ref. [110] at 1405.7 keV. The a_2/a_4 values and R_{dco} ratio for the 1404.5(1) keV γ ray were measured to be 0.12(12)/-0.05(15) and 1.13(13), consistent with a $\Delta J = 0$ transition implying a $J = 2$ assignment for the 4809 keV state. In the mirror ^{30}Si there is only one known $J = 2$ level in the energy range 4.2-5.0 MeV at 4810 keV with $J^\pi = 2_3^+$. Therefore the γ rays 1404 and 2599 keV are assigned to the 2_3^+ 4809 keV excited state in ^{30}S, corresponding to a resonance energy of 413.1(10) keV.

The 5123.1(1) and 5848.0(4) keV levels

Fig. 6.11 shows two γ-ray transitions in coincidence with the transition from the 2210 keV state to the ground state at 2921.8(1) and 3637.7(4) keV, indicating levels at 5123.1(1) and 5848.0(4) keV. The angular distribution for the 2921.8(1) keV transition is shown in Fig. 6.7. The excitation values are in agreement with previous experiments within errors [110, 117] shown in Table 6.2. However, they disagree with the values found in Ref. [111], where the two states were measured to have energies of 5130.0(18) and 5835.5(13) respectively. a_2/a_4 values of 0.37(2)/-012(3) and 0.30(4)/-0.05(6) were measured for the 5123 and 5848 keV states respectively, consistent with $\Delta J = \pm 2$. The observed distributions are anisotropic, allowing 0^+ assignments to be ruled out and the 5132 and 5848 keV

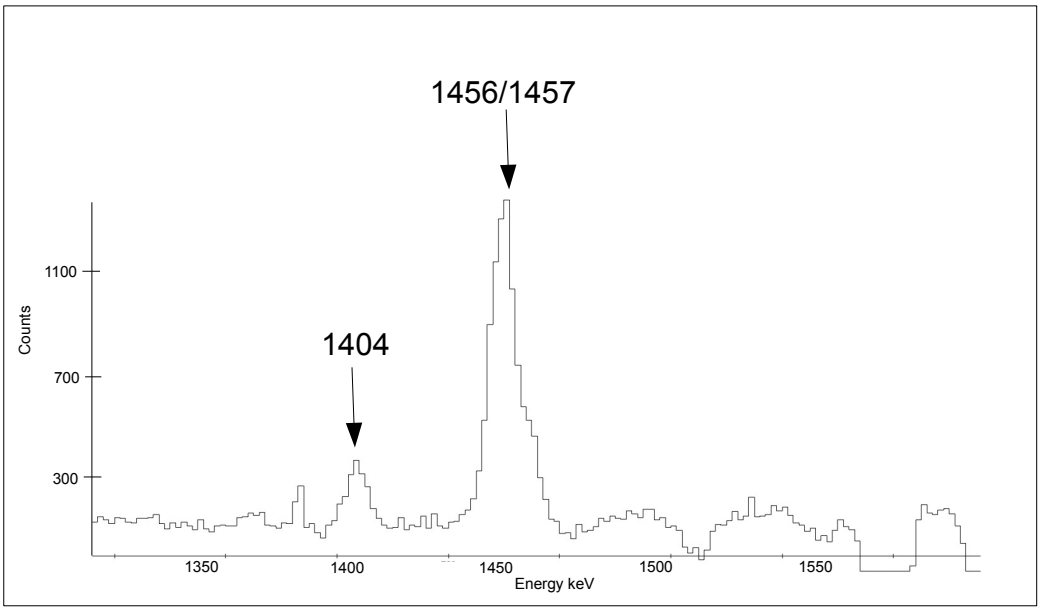

Figure 6.10 *Spectrum created from a coincidence with the 2210 keV γ ray. The 1404 keV γ-ray transition comes from the 4808.7(3) keV state to the 3404.1(1). The 1457 keV γ-ray transition comes from the 3668.0(4) to the 2210.1(1) keV and the 1467 keV γ-ray transition comes from the 3677.1(4) keV to the 2210.1(1).*

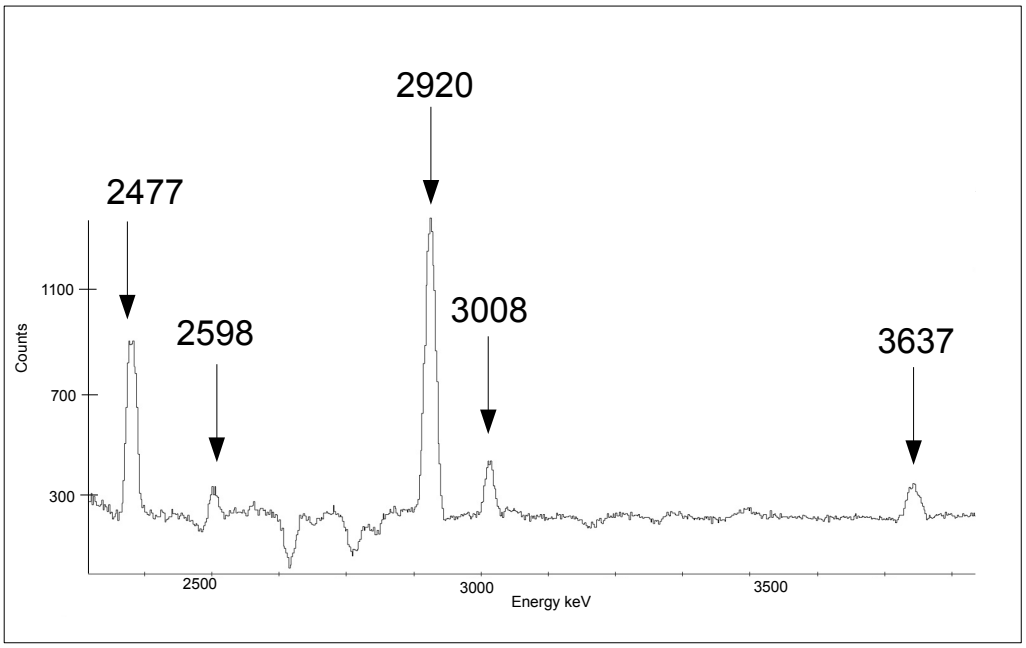

Figure 6.11 *Spectrum created from a coincidence with the 2210 keV γ ray. The 2477 keV γ-ray transition comes from the 4687.6(2) keV to the 2210.1(1) keV state. The 2398 keV γ-ray transition comes from the 4808.7(3) keV state to the 2210.1(1) keV state. The 2920 keV γ-ray transition comes from the 5132.1(1) keV to the 2210.1(1) keV state. The 3008 keV γ-ray transition comes from the 5218.8(3) keV state to the 2210.1(1) keV state. The 3637 keV γ-ray transition comes from the 5848.0(4) keV state to the 2210.1(1) keV state.*

levels are therefore assigned 4_1^+ and 4_2^+ respectively.

The 5218.8(14) keV level

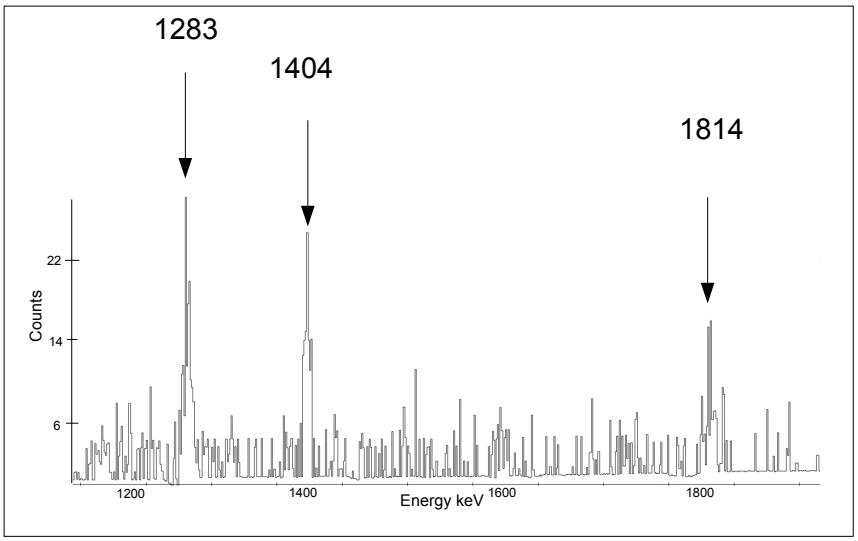

Figure 6.12 *Spectrum created from a coincidence with both the 2210 and 1194 keV γ rays. The 1283 keV γ-ray transition comes from the 4687.6(2) keV state to the 3404.1(1) keV state. The 1404 keV γ-ray transition comes from the 4808.7(3) to the 3404.1(1) state. The 1814 keV γ-ray transition comes from the 5218.8(3) keV state to the 3404.1(1) keV state.*

An excited state at 5218.8(14) keV has been previously identified in a β-delayed $2p$ decay of ^{31}Ar [121] and in a ^{32}S$(p,t)^{30}$S transfer reaction [109]. In this study two γ-decays to the 2210 and 3404 keV levels are observed at 1814.4(3) and 3008.5(2) keV, shown in Fig. 6.11 and 6.12, indicating an excited state at 5218.8(3) keV, in good agreement with Ref.'s [111, 121]. The two γ-decay branches were found to have a_2/a_4 values of -0.32(11)/0.02(12) and -0.28(9)/0.03(11) respectively and R_{dco} ratios of 0.56(34) and 0.59(10), consistent with $\Delta J = \pm 1$, indicating either a $J = 1$ or 3 spin assignment. In the mirror nucleus ^{30}Si in the energy range 5.0-6.0 MeV there are no observed $J = 1$ states and only two $J = 3$ states at 5228 and 5485 keV with $J^\pi = 3_2^+$ and 3_1^- respectively. The 5485 keV state has already been firmly assigned to the 5314 keV 3_1^- state not observed in this study. Therefore the 5219 keV level is assigned $J^\pi = 3_2^+$.

The 5168(6) and 5391(3) keV levels

Two previously reported levels at 5168(6) and 5391(3) keV in ^{30}S in ^{32}S(p,t) studies by Bardayan *et al.* [108] and by Setoodehnia *et al.* [109], corresponding to resonance energies of 769(7) and 992(4) keV, respectively were not observed in this study. Only two states in the mirror ^{30}Si in the energy range 5.0-6.0 MeV remain unmatched, at 5372 and 5614 keV with $J^\pi = 0_3^+$ and 2_4^+ respectively. In Ref. [108], the state at 5168(6) keV was observed and highlighted to be a likely doublet with angular distributions that indicated assignments of 4^+ and 0^+ for this level. As the 5132 keV state, very close in proximity to the 5168 keV level reported in Ref. [108], has already been found to be 4_1^+, the 5168 keV state is therefore concluded to have a $J^\pi = 0_3^+$. This leaves the other unobserved state at 5391 keV with $J^\pi = 2_4^+$, also consistent with the angular distributions reported in Ref. [108]. From barrier penetrability calculations, the proton widths of $l_p = 0$ and $l_p = 2$ captures to the excited states in ^{30}S at 5168 and 5391 keV respectively, are expected to be several orders of magnitude larger than the corresponding γ-widths, implying that these transitions would not be expected to be seen here. Fig. 6.13 shows the mirror assignments for ^{30}S and ^{30}Si above the proton emission threshold as have been discussed here. Fig. 6.13 also compares the original shell model predictions to the current knowledge.

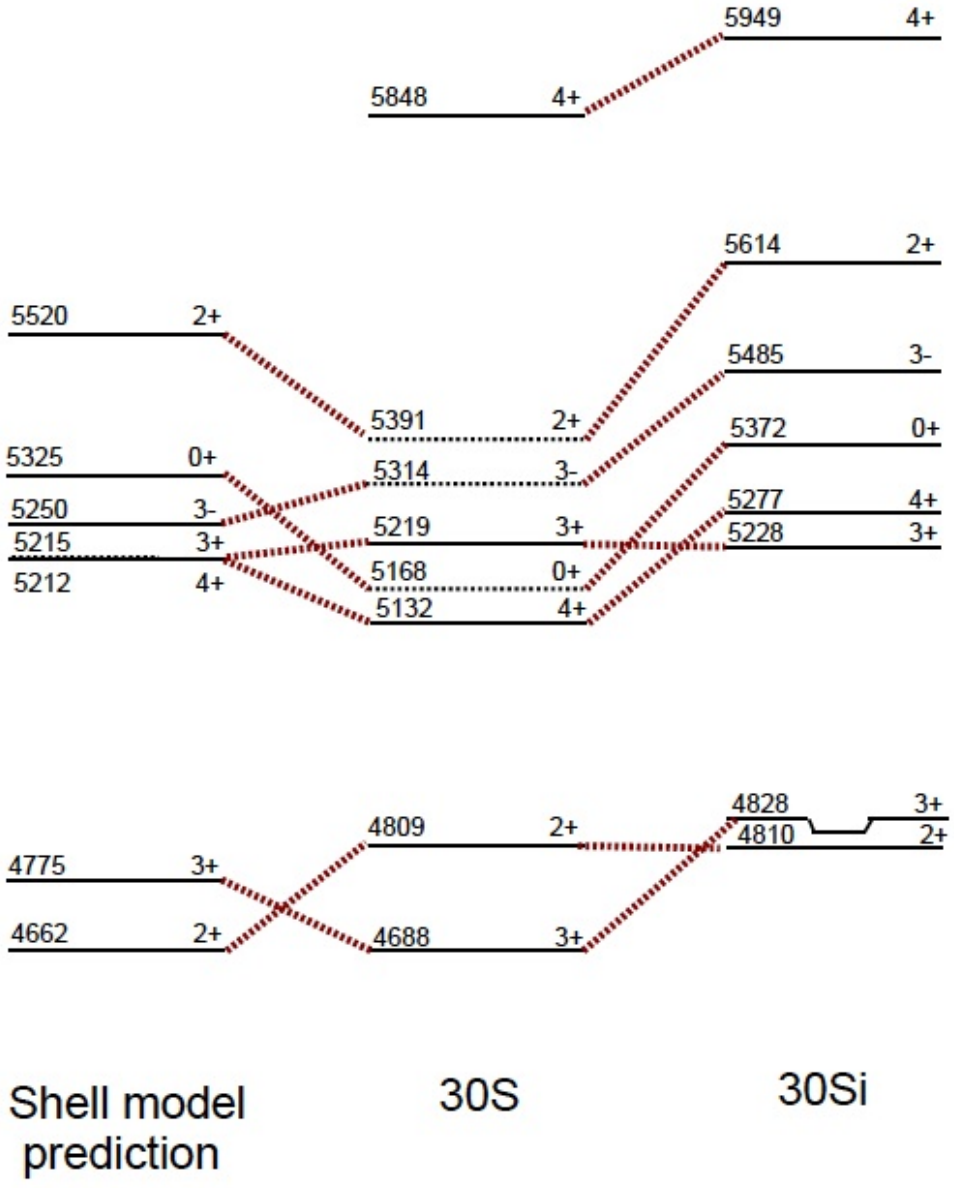

Figure 6.13 *Mirror diagram, showing the assignments of excited states in ^{30}S with their analogous states in ^{30}Si over the energy range 4.6-5.9 MeV. The original shell model predictions are also shown, from Ref. [106].*

6.4.3 The ^{29}P$(p,\gamma)^{30}$S Reaction Rate

The new precise resonance energies and the firm spin-parities above the proton emission threshold in ^{30}S have been used to calculate an updated reaction rate for the $^{29}\mathrm{P}(p,\gamma)^{30}\mathrm{S}$ reaction. From Ref.'s [106, 107] it is known that the direct capture rate has a negligible affect on the overall reaction rate and was therefore not included in the total reaction rate. To calculate the reaction rate, firstly the proton and γ-ray partial widths needed to be estimated.

As mention in Chapter 2, to calculate the proton partial widths spectroscopic factors from transfer reactions of the mirror are used. Spectroscopic factors from mirror states in ^{30}Si were used [123]. For states that were too weak to be seen in Ref. [123], a value of 0.01 is presumed for the spectroscopic factor, C^2S. The analog states of the two lowest-lying resonances at 292 and 413 keV were measured to have spectroscopic factors of 0.04 and 0.11 respectively, with no errors quoted [123].

The gamma partial widths were estimated using lifetimes from the proposed mirror states. The 992 keV resonance has no lifetime for its analog mirror available and therefore for the γ-ray partial width the value reported in the most recent theoretical study of the reaction $^{29}\mathrm{P}(p,\gamma)^{30}\mathrm{S}$ by Iliadis et al. [104] is used. Fig. 6.14 shows the contribution from the first 8 resonances and the total reaction rate. For temperatures from 0.1-0.4 GK, the reaction rate is found to be dominated by the two key resonances highlighted by Ref. [107] at 292 and 413 keV with $J^\pi = 3^+$ and 2^+ respectively. At temperatures greater than 0.5 GK, corresponding to those found in X-ray bursters, the reaction rate is found to be dominated by the 413 keV 2^+ resonance, with an additional contribution from the 823 keV 3^+ resonance at temperatures greater than $\sim$2 GK.

A ratio of the current reaction rate to the most recent theoretical estimate by Iliadis *et al.* [104] is shown in Fig. 6.15. Fig. 6.15 shows that the current reaction rate is in good agreement with Ref. [104]. Earlier estimates differ more greatly. The current reaction rate is approximately 2 orders of magnitude lower than the reaction rate in Ref. [107].

Taking into account the inaccuracies in the calculation of the proton and partial widths, it is now expected that the current reaction rate has an uncertainty of $\sim$2 for novae and X-ray burster environments. This therefore means that precise calculations of novae ejecta are now possible, as well as providing greater knowledge of the flow of reactions as a X-ray burst approaches its peak.

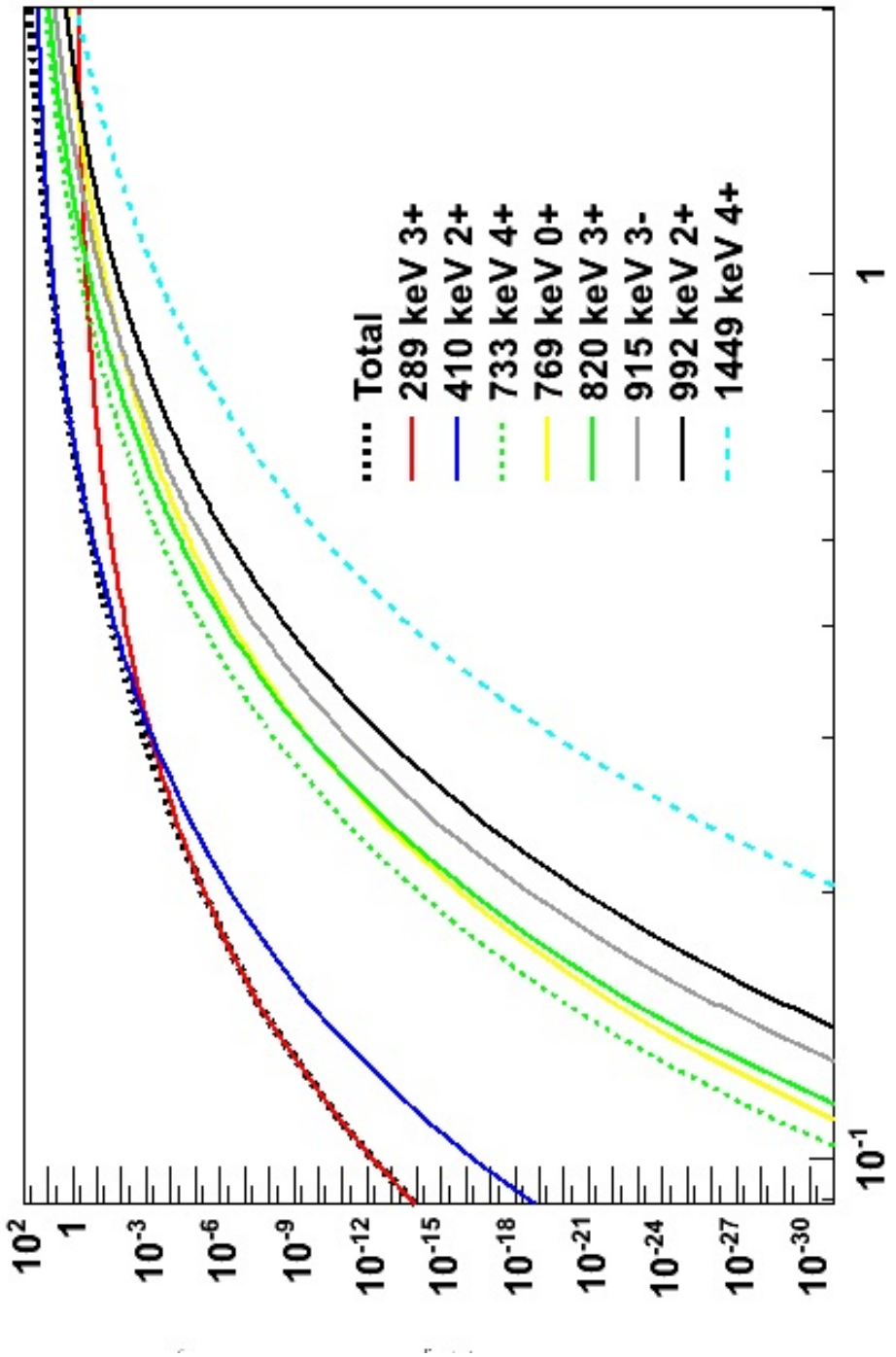

Figure 6.14 *Reaction rate for the $^{29}P(p,\gamma)^{30}S$ reaction, showing the different contributions from the individual resonances.*

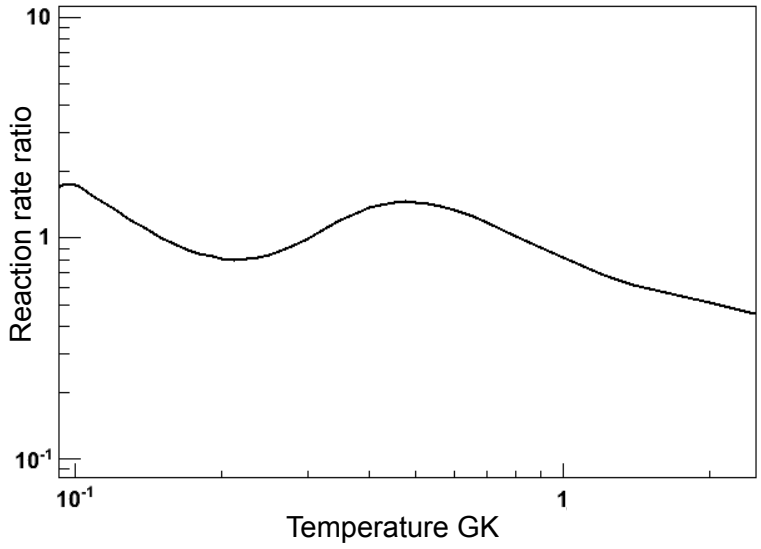

Figure 6.15 *The current reaction rate as a ratio of the most recent theoretical estimate by Iliadis* et al. *[104].*

Table 6.3 *Present data found in the current experiment on ^{30}S.*

E_x (keV) present	E_r (keV)	E_γ (keV)	I_γ	a_2/a_4	R_{dco}	Assignment
2210.1(1)		2210.0(1)	100.0(7)	0.14(1)/-0.08(2)	1.21(3)	$2_1^+ \rightarrow 0_1^+$
3404.1(1)		1194.1(1)	44.9(2)	0.06(1)/0.00(2)	1.12(4)	$2_2^+ \rightarrow 2_1^+$
3668.0(4)		1457.9(4)	3.2(1)	-0.01(11)/-0.13(13)	0.90(10)	$0_2^+ \rightarrow 2_1^+$
3677.1(4)		1467.0(4)	2.3(1)	-0.09(13)/-0.12(14)	0.41(34)	$1_1^+ \rightarrow 2_1^+$
4687.6(2)	292.0(9)	1283.4(3)	2.6(1)	-0.10(9)/-0.11(11)	0.44(16)	$3_1^+ \rightarrow 2_2^+$
		2477.4(1)	14.8(2)	-0.47(3)/-0.04(4)	0.51(2)	$3_1^+ \rightarrow 2_1^+$
4808.7(3)	413.1(10)	1404.5(1)	3.1(1)	0.12(12)/-0.05(15)	1.13(13)	$2_3^+ \rightarrow 2_2^+$
		2598.6(4)	3.1(1)			$2_3^+ \rightarrow 2_1^+$
5132.1(1)	736.5(8)	2921.8(1)	26.7(2)	0.37(2)/-0.12(3)	1.28(3)	$4_1^+ \rightarrow 2_1^+$
5218.8(3)	823.2(10)	1814.4(3)	1.4(8)	-0.32(11)/0.02(12)	0.56(34)	$3_2^+ \rightarrow 2_2^+$
		3008.5(2)	5.5(1)	-0.28(9)/0.03(11)	0.59(10)	$3_2^+ \rightarrow 2_1^+$
5848.0(4)	1452.4(11)	3637.7(4)	4.5(1)	0.30(4)/-0.05(6)	1.30(8)	$4_2^+ \rightarrow 2_1^+$

Chapter 7

Conclusions and Future Work

Two separate experiments have been performed gaining insight into two T_z= -1 nuclei, ^{20}Na and ^{30}S, important for explosive binary star systems. A study of the β-delayed proton decay of ^{20}Mg to investigate the astrophysically important nucleus ^{20}Na above the proton emission threshold 2190.1(1) keV [70] was performed. $J^{\pi} = 0^{+}$ and 1^{+} resonances above the proton emission threshold were observed and resonance energies determined. A proton from a previously observed resonance was seen in a β-delayed proton decay study of ^{20}Mg for the first time, with an energy of 885(15) keV and the branch and corresponding logft value were able to be determined to be 0.5(1)% and 5.41(9) respectively. All states in ^{20}Na in the range 2.6 - 3.6 MeV were paired with analogous states in the mirror ^{20}F. Through careful examination of previous studies the precise energy of the key resonance, 457(3) keV, expected to dominate the $^{19}\mathrm{Ne}(p,\gamma)^{20}\mathrm{Na}$ reaction at astrophysical temperatures, was determined [77, 81]. From the non-observation of the β-proton branch in this study a lower limit on the logft of 6.9 for the key resonance was placed, strongly implying that the spin-parity of the 457 keV key resonance is $J^{\pi} = 3^{+}$. The effect of the spin-parity assignment and calculated resonance energy for the key 457 keV resonance on the $^{19}\mathrm{Ne}(p,\gamma)^{20}\mathrm{Na}$ reaction rate was investigated. It was found that a 3^{+} spin-parity assignment increases the resonance strength, implying an increase in the $^{19}\mathrm{Ne}(p,\gamma)^{20}\mathrm{Na}$ reaction rate at astrophysical temperatures. The new rate of the $^{19}\mathrm{Ne}(p,\gamma)^{20}\mathrm{Na}$ reaction was compared to the most recent compilation theoretical study reaction rate and it was found to be nearly an order of magnitude lower at astrophysical temperatures [104].

The decrease in the overall reaction rate combined with the new, accurate energy

for the 457 keV key resonances strongly favours a new direct measurement of the resonance strength of the key resonance. A proposal to study this is currently submitted to TRIUMF. The current limit on the resonance strength of 15 meV [86] is just slightly incompatible with the theoretical lower limit of 16 meV [85] for a 3^+ spin-parity assignment and as such it would be desirable for a direct measurement of the resonance strength to be undertaken in the near future.

The impact of the current results for the ^{19}Ne$(p,\gamma)^{20}$Na reaction within explosive binary star systems is uncertain. The increase in the reaction rate for the 457 keV resonance could imply that break out to the rp process starts at a lower temperature, although this is not certain as the overall reaction rate saw a decrease. The preceding reaction, ^{15}O$(\alpha,\gamma)^{19}$Ne, is also believed to be slower and therefore this reaction could be the deciding factor for the temperature at which breakout occurs. In order to fully understand the impact of the current result on explosive binary star systems more information is required on the ^{15}O$(\alpha,\gamma)^{19}$Ne reaction and the entire reaction sequence.

A γ-ray spectroscopy study of the astrophysically important nucleus ^{30}S was performed. This study confirmed spin-parity assignments of $J^\pi = 3^+$ and 2^+ for the first two resonances above the proton emission threshold in ^{30}S, with excitation energies of 4687.6(2) and 4808.7(3) keV respectively. These two resonances are believed to dominate the ^{29}P$(p,\gamma)^{30}$S reaction rate at astrophysical temperatures. In total nine levels were populated and identified, including spin-parity assignments. Levels in ^{30}S over the range 4.6 - 5.9 MeV were paired with their analogue states in the mirror ^{30}Si.

The new resonance energies and spin-parity assignments, combined with previous energies for the resonances not observed in this study, were used to investigate the ^{29}P$(p,\gamma)^{30}$S reaction rate at astrophysical temperatures. A decrease of $\sim$2 in the uncertainty of the ^{29}P$(p,\gamma)^{30}$S reaction rate was achieved. It is now expected that the reaction rate is determined well enough for precise calculations of abundances in novae ejecta. It is also now possible for an improved model of the flow of reactions as a X-ray burst approaches its peak to be calculated. Direct measurements of the ^{29}P$(p,\gamma)^{30}$S reaction are unlikely to yield a great reduction in the reaction rate and as such would be not be suggested.

Bibliography

[1] H.A. Bethe and C.L. Critchfield. *Physical Review*, 54:248, 1938.

[2] H.A. Bethe. *Physical Review*, 55:434, 1939.

[3] C.F. von Weizsäscker. *Zeitschrift fur Physik*, 39:633, 1938.

[4] M. Wiescher, J. Gorres, E. Uberseder, G. Imbriani, and M. Pignatari. *Annual Review of Nuclear and Particle Science*, 60:381, 2010.

[5] R.K. Wallace and S.E. Woosley. *The Astrophysical Journal Supplement Series*, 45:389, 1981.

[6] C.A. Bertulani and A. Gade. *Physics Reports*, 485:195, 2010.

[7] K. Langanke. Explosive hydrogen burning: novae and x-ray bursts. In *GSI and TUD, Darmstadt*, 2006.

[8] http://www.cfa.harvard.edu/hea/osp/wdan.html, .

[9] P. Hauschildt, S. Starrfield, S. N. Shore, F. Allard, and E. Baron. *The Astrophysical Journal*, 447:829, 1995.

[10] D. Prialnik and A. Kovetz. *The Astrophysical Journal*, 455:789, 1995.

[11] K. Nomoto. *The Astrophysical Journal*, 277:791, 1984.

[12] A.E. Champagne and M. Wiescher. *Annual Review of Nuclear and Particle Science*, 42:39, 1992.

[13] http://astronomy.swin.edu.au/cms/astro/cosmos/r/Roche-lobe+Overflow, .

[14] J.S. Gallagher and S. Starrfield. *Annual Review Astronomy and Astrophysics*, 16:171, 1978.

[15] J.W. Truran. *Essays in Nuclear Astrophysics*, page 467, 1982.

[16] S. Starrfield, S. Sparks, and J.W. Truran. *The Astrophysical Journal*, 220: 1063, 1978.

[17] A. Kovetz and D. Prialnik. *The Astrophysical Journal*, 291:812, 1985.

[18] S. Starrfield. *Classical Novae*, page 39, 1989.

[19] J.W. Truran. *Physics of Classical Novae*, page 373, 1990.

[20] B. Lazareff, J. Audouze, S. Starrman, and J. Truran. *The Astrophysical Journal*, 228:875, 1979.

[21] S. Wanajo, K. Nomoto, M. Hashimoto, T. Kajino, and S. Kubono. *Nuclear Physics A*, 616:91, 1997.

[22] J. José, M. Hernanz, S. Amari, K. Lodders, and E. Zinner. *The Astrophysical Journal*, 612:414, 2004.

[23] S. Starrfield, J.W. Truran, M. Wiescher, and W.M. Sparks. *Monthly Notice of the Royal Astromonical Society*, 296:502, 1998.

[24] M. Wiescher, J. Görres, and H. Schatz. *Journal Physics G:Nuclear and Particle Physics*, 25(6):133, 1999.

[25] M.M. Shara, M. Livio, A.F.J. Moffat, and M. Orio. *The Astrophysical Journal*, 311:163, 1986.

[26] E. Zinner. *Annual Review Earth and Planetary Sciences*, 26:147, 1998.

[27] S. Amari, X. Gao, L.R. Nittler, E. Zinner, J. José, M. Hernanz, and R.S. Lewis. *The Astrophysical Journal*, 551:1065, 2001.

[28] C. Iliadis, A.E. Champagne, J. José, S. Starrfield, and P. Tupper. *The Astrophysical Journal Supplement Series*, 142:105, 2002.

[29] J. Grindlay, H. Gursky, H. Schnopper, D.R. Parsignault, J. Heise, A.C. Brinkman, and J. Shcrijver. *The Astrophysical Journal Letters*, 205:127, 1976.

[30] C. Pinto, J.S. Kaastra, E. Costantini, and F. Verbunt. *Astronomy and Astrophysics*, 521:A79, 2010.

[31] R.E. Taam. *AIP Conference Proceedings*, 115:1, 1984.

[32] W.H.G. Lewin, J. van Paradijis, and R. Taam. *Space Science Review*, 62: 233, 1993.

[33] C.J. Hansen, S.D. Kawaler, and V. Trimble. *Stellar Interiors*. Springer, 1994.

[34] R. Taam, S.E. Woosley, and D. Lamb. *The Astrophysical Journal*, 459:271, 1996.

[35] P.C. Joss and F.K. Li. *The Astrophysical Journal*, 238:287, 1980.

[36] M.Y. Fujimoto, T. Hanawa, and S. Miyaji. *The Astrophysical Journal*, 246: 267, 1981.

[37] A. Ayasli and P.C. Joss. *The Astrophysical Journal*, 256:637, 1982.

[38] E.F. Brown and L. Bildsten. *The Astrophysical Journal*, 496:915, 1998.

[39] L. Bildsten. *The Many Faces of Neutron Stars*. 1998.

[40] H. Schatz, L. Bildsten, A. Cumming, and M. Wiescher. *The Astrophysical Journal*, 524:1014, 1999.

[41] L. Bildsten and C. Cutler. *The Astrophysical Journal*, 449:800, 1995.

[42] E.E. Salpeter. *The Astrophysical Journal*, 115:326, 1952.

[43] H. Schatz, A. Aprahamian, J. Görres, H. Wiescher, T. Rauscher, J.F. Rembges, F.-K. Thielemann, B. Pfeiffer, P. Möller, K.-L. Kratz, H. Herndi, B.A. Brown, and H. Rebel. *Physical Reports*, 294:167, 1998.

[44] J. Görres, M. Wiescher, and F.K. Thielemann. *Physical Review*, 51:392, 1995.

[45] L.V. Grigorenko and M.V. Zhukov. *Physical Review C*, 72:015803, 2005.

[46] K. Langanke, M. Wiescher, W.A. Fowler, and J. Görres. *The Astrophysical Journal*, 301:629, 1986.

[47] J.L. Fisker, H. Schatz, and F.-K Thielemann. *The Astrophysical Journal Supplement Series*, 174:261, 2008.

[48] H. Schatz, A. Aprahamian, J. Görres, M. Wiescher, T. Rauscher, J.F. Rembges, F.-K Thielemann, B. Pfeiffer, P. Möller, K.-L. Kratz, H. Herndl, B.A. Brown, and H. Rebel. *Physics Reports*, 294:167, 1998.

[49] A. Parikh, J. José, F. Moreno, and C. Iliadis. *The Astrophysical Journal Supplement Series*, 178:110, 2008.

[50] J.L. Fisker, F.-K. Thielemann, and M. Wiescher. *The Astrophysical Journal Letters*, 608(61), 2004.

[51] C. E. Rolfs and W. S. Rodney. *Cauldrons in the Cosmos*. University of Chicago Press, 2005.

[52] C. Iliadis. *Nuclear Physics of Stars*. Wiley VCH, 2007.

[53] G. Gamow. *Zeitschrift fur Physik*, 51:204, 1928.

[54] D. Page and J. G. Hirsch. *From the Sun to the Great Attractor: 1999 Guanajuato Lectures on Astrophysics*. Spinger, 2000.

[55] L. Trache. *Romanian Journal of Physics*, 52:823, 2007.

[56] G. Lotay. *Gamma-ray Spectroscopy Measurements for Nuclear Reactions in Novae*. PhD thesis, The University of Edinburgh, 2009.

[57] B.J. Cole, A. Watt, and R.R. Whitehead. *Journal of Phyiscs G: Nuclear and Particle Physics*, 2:501, 1976.

[58] J.S. Lilley. *Nuclear Physics: Princles and Applications*. Wiley and Sons, 2001.

[59] C.B. Hinke et al. *Nature*, 486:341, 2012.

[60] http://upload.wikimedia.org/wikipedia/commons/1/1f/Zerfallsschema.png, .

[61] W. Heisenburg. *Zeischrift fur Physik*, 77:1, 1932.

[62] E. Wigner. *Physical Review*, 51:106, 1937.

[63] B. Povh, K. Rith, and C. Scholz. *Particles and Nuclei*. Springer, 2008.

[64] E.P. Wigner. *Proceedings of the Robert A Welch Conference on Chemical Research, vol.1, Robert A Welch Foundation, Houston, Texas*, page 67, 1957.

[65] S.M. Lenzi and M.A. Bentley. Isospin symmetry breaking in mirror nuclei. 2010.

[66] K.S. Krane. *Introductory Nuclear Physics*. Wiley, 1988.

[67] D. Schwalm and D. Pelte. North Holland Publishing Company, 1982.

[68] D.C. Radford. *Nuclear Instruments and Methods in Physics Research Section A: Accelerators, Spectrometers, Detectors and Associated Equipment*, 361:296, 1995.

[69] D. Seweryniak, P.J. Woods, B. Blank, M.P. Carpenter, T. Davinson, S.J. Freeman, J. Görres, A. Heinz, R.V.F. Janssens, H. Mahmud, T.L. Khoo, Z. Lui, G. Mukherjee, E. Rehm, F. Sarazin, J. Shergur, M. Shawcross, S. Sinha, and A. Woehr. *Physics Letters B*, 590:170, 2004.

[70] C. Wrede et al. *Physical Review C*, 81:055503, 2010.

[71] L.O. Lamm, C.P. Browne, J. Görres, M. Wiescher, and A.A. Rollefson. *Zeitschrift fur Physik A*, 327:239, 1987.

[72] L.O. Lamm, C.P. Browne, J. Görres, S.M. Graff, M. Wiescher, A.A. Rollefson, and B.A. Brown. *Nuclear Physics A*, 510:503, 1990.

[73] S. Kubono, H. Orihara, S. Kato, and T. Kajino. *The Astrophysical Journal*, 344:460, 1989.

[74] S. Kubono, N. Ikeda, M. Yasue, T. Nomura, Y. Fuchi, H. Kawashima, S. Kato, H. Orihara, T. Shinozuka, H. Ohnuma, H. Miyatake, and T. Shimoda. *Zeitschrift fur Physik A*, 331:359, 1988.

[75] N.M. Clarke, P.R. Hayes, M.N. Becha, C.N. Pinder, and S. Roman. *Journal of Physics G: Nuclear and Particle Physics*, 16:1547, 1990.

[76] N.M. Clarke, S. Roman, C.N. Pinder, and P.R. Hayes. *Journal of Physics G: Nuclear and Particle Physics*, 19:1411, 1993.

[77] M.S. Smith, P.V. Magnus, K.I. Hahn, A.J. Howard, P.D. Parker, A.E. Champagne, and Z.Q. Mao. *Nuclear Physics A*, 536:333, 1992.

[78] B.D. Anderson, B. Wetmore, A.R. Baldwin, L.A.C. Garcia, D.M. Madey, J.W. Watson, W.M. Zhang, B.A. Brown, C.C. Foster, and Y. Wang. *Physical Review C*, 52(4):2210, 1995.

[79] M. Huyse and R. Raabe. *Journal Physics G*, 38:024001, 2011.

[80] B.A. Brown, A.E. Champagne, H.T. Fortune, and R. Sherr. *Physical Review C*, 48(3):1456, 1993.

[81] R. Coszach et al. *Physical Review C*, 50(3):1695, 1994.

[82] R.D. Page et al. *Physical Review Letters*, 73(23):3066, 1994.

[83] C. Michotte et al. *Physical Letters B*, 381(4):402, 1996.

[84] G. Vancraeynest et al. *Physical Review C*, 57(5):2711, 1998.

[85] H.T. Fortune, R. Sherr, and B.A. Brown. *Physical Review C*, 61(5):057303, 2000.

[86] M. Couder, C. Angula, E. Casarejos, P. Demaret, P. Leleux, and F. Vanderbist. *Physical Review C*, 69(2):022801(R), 2004.

[87] A. Piechaczek et al. *Nuclear Physics A*, 584(3):509, 1995.

[88] S. Kubono et al. *Physical Review C*, 46(1):361, 1992.

[89] J. Görres, M. Wiescher, K. Scheller, D.J. Morrissey, B.M. Sherrill, D. Bazin, and J.A. Winger. *Physical Review C*, 46(3):R833, 1992.

[90] R. Coszach et al. *Proc. 2nd INt. Symp. on Nuclear Astrophysics nuclei in the cosmos. Karlsruhe*, page 295, 1993.

[91] John M. Nieminen. A tool to study fusion-evaporation reactions, 1998.

[92] Ingo Wiedenhöver. *Physics*, 5:73, 2012.

[93] http://cyclotron.tamu.edu/, .

[94] Matt McCleskey. Private communication.

[95] R.E. Tribble, R.H. Burch, and C.A. Gagliardi. *Nuclear Instruments and Methods in Physics Research*, 285:441, 1989.

[96] R.G. Sextro, R.A. Gough, and J. Cerny. *Physical Review C*, 8:258, 1981.

[97] S. Raman, E.K. Warburton, J.W. Starner, E.T. Jurnery, J.E. Lynn, P. TIkkanen, and J. Keinonen. *Physical Review C*, 53:616, 1995.

[98] D.E. Alburger, G. Wang, and E.K Warburton. *Physical Review C*, 35:1479, 1986.

[99] H.T. Fortune and R.R. Betts. *Physical Review C*, 10:1292, 1974.

[100] J. Görres and M. Wiescher. *Physical Review C*, 52:412, 1995.

[101] D.R. Tilley, C.M. Cheves, J.H. Kelley, S. Raman, and H.R. Weller. *Nuclear Physics A*, 636:249, 1998.

[102] M.S. Chowdhury, M.A. Zaman, and H.M. Sen Gupta. *Physical Review C*, 46:2273, 1992.

[103] T. Fortune. Private correspondence.

[104] C. Iliadis, R. Longland, A.E. Champagne, A. Coc, and R. Fitzgerald. *Nuclear Physics A*, 841:31, 2010.

[105] M. Wang, G. Audi, A.H. Wapstra, F.G. Kondev, M. MacCormick, X. Xui, and B. Pfeiffer. *Chinese Physics C*, 36(12):1603, 2012.

[106] M. Wiescher and J. Görres. *Zeitschrift fur Physik A*, 329(1):121, 1988.

[107] C. Iliadis, J.M. D'Auria, S. Starrfield, W. Thompson, and M. Wiescher. *Astrophysical Journal Supplement Series*, 134:151, 2001.

[108] D.W. Bardayan, J.C. Blackmon, R.P. Fitzgerald, W.R. Hiz, K.L. Jones, R.L. Kozub, J.F. Liang, R.J. Livesay, Z. Ma, L.F. Roberts, M.S. Smith, J.S. Thomas, and D.W. Visser. *Physical Review C*, 76:045803–1, 2007.

[109] K. Setoodehnia, A.A. Chen, J. Chen, J.A. Clark, C.M. Deibel, S.D. Geraedts, D. Kahl, P.D. Parker, D. Seiler, and C. Wrede. *Physical Review C*, 82:022801(R), 2010.

[110] K. Setoodehnia et al. *Physical Review C*, 83:018803, 2011.

[111] S. Almaraz-Calderon et al. *Physics Review C*, 86:065805–1, 2012.

[112] http://www.phy.anl.gov/atlas/, .

[113] J. Eberth and J. Simpson. *Progress in Particle Nuclear Physics*, 60:283, 2008.

[114] http://nucalf.physics.fsu.edu/ riley/, .

[115] http://radware.phy.ornl.gov/gf3/gf3.html, .

[116] R.A. Paddock. *Physical Review C*, 5:485, 1972.

[117] P.M. Endt. *Nuclear Physics A*, 521:1, 1990.

[118] D. Steppenbeck et al. *Nuclear Physics A*, 847:149, 2010.

[119] E. Kuhlmann, W. ALbrecht, and A. Hoffmann. *Nuclear Physics A*, 213(1): 82, 1973.

[120] H. Yokota, K. Fujioka, K. Ichimaru, Y. Mihara, and R. Chiba. *Nuclear Physics A*, 383(2):298, 1982.

[121] H.O.U. Fynbo et al. *Nuclear Physics A*, 677:38, 2000.

[122] J.M.G. Caraça, R.D. Gill, A.J. Cox, and H.J. Rose. *Nuclear Physics A*, 193 (1):1, 1972.

[123] H. Mackh et al. *Nuclear Physics A*, 202(3):497, 1973.